



Norwegian University of  
Science and Technology

# Intergranular Corrosion of Extruded AlMgSi(Cu,Zn) Alloys

**Phuong Vy Thi Lam**

Chemical Engineering and Biotechnology

Submission date: June 2016

Supervisor: Trond Furu, IMTE

Co-supervisor: Otto Lunder, IMT

Norwegian University of Science and Technology  
Department of Materials Science and Engineering





# Preface

The work presented in the master thesis «Intergranular Corrosion of Extruded AlMgSi (Cu,Zn) Alloys» was conducted at the Department of Materials Engineering, NTNU, the spring 2016.

This thesis has been a part of the larger collaboration project FICAL - *Fundamentals of Intergranular Corrosion in Aluminium Alloys* with participation from NTNU, SINTEF and the following aluminium manufacturers and partners; Hydro, Benteler, Sapa, Steertec and Gränges.

Furthermore, this work is a continuation of the project thesis «Corrosion of 6082 alloys in maritime environment», carried out the autumn 2015.

All work presented has been carried out by the author, with the exception of the STEM and EDS analysis which was obtained with the assistance from Senior Research Scientist John C. Walmsley from SINTEF.

Phuong Vy Thi Lam  
June 2016, Trondheim



# Acknowledgement

First and foremost, acknowledgements are directed to my supervisor Trond Furu<sup>1</sup> and co-supervisor Otto Lunder<sup>2</sup>. It has been truly exciting to be a part of this project. Your expertise guidance and our academic discussions have been sincerely appreciated and of great significance for the progression of this work.

I would also like to show my deepest gratitude towards John C. Walmsley<sup>2</sup> for his efforts and assistance with the with the TEM studies. This thesis would not have been the same without your contribution. Furthermore, I would like to thank Yingda Yu<sup>3</sup> and Trygve Lindahl Schanche<sup>3</sup> for the guidance related to SEM and sample preparations carried out last year. Your excellent guiding has been of great value this spring. I also want to thank my fellow classmates Sondre Røstbø and Christian Lauritsen for helping me with the electrochemical measurements.

Finally and certainly not least, I want to thank all the lovely people who have made these last memorable five years truly wonderful.

---

<sup>1</sup>Hydro Aluminium, Sunndalsøra

<sup>2</sup>SINTEF Materials and Chemistry, Trondheim

<sup>3</sup>Department of Materials Science and Engineering, NTNU, Trondheim



# Abstract

In general, the 6xxx series alloys (AlMgSi) are considered to be resistant to intergranular corrosion (IGC) in marine environments. However, the addition of copper to increase peak hardness has proven to increase the IGC susceptibility. The detrimental effect on IGC resistance is believed to be caused by the formation of a nanoscale continuous Cu rich film confined along the grain boundaries of the material. Evaluation of IGC susceptibility in heat treatable aluminium alloys is generally carried out by metallographic examination of specimens after exposure in an acidified chloride test solution. Experience has revealed that accelerated corrosion testing is highly dependent on several factors. Especially extruded specimens with a region comprised of highly directional grains in the centre and a recrystallised surface have shown to experience severe corrosion inwards the fibrous area. This observation is believed to influence the extent of corrosion on the recrystallised specimen surface. Extruded copper containing AA6082 alloys modified with various Zn levels were corrosion tested according to BS-ISO 11846 (method B) in the T5 and T6 temper. Several IGC test parallels were conducted to examine how the edge microstructure affects the IGC resistance of these alloys. The influence of Zn on IGC susceptibility was investigated as well. Optical microscopy (LM) was used to characterise the microstructure of the T5 and T6 profiles, and scanning transmission electron microscopy (STEM) and energy dispersive spectroscopy (EDS) analysis were conducted to identify and characterise the grain boundary chemistry in the fibrous microstructure. Assessment of corrosion susceptibility was done by metallographic examination in LM and scanning electron microscopy (SEM) after accelerated corrosion testing. Results reveal that the edge microstructure had a significant effect on the corrosion behaviour of the recrystallised surface. Corrosion susceptible T5 tempered alloys with a fibrous microstructure and recrystallised surface experienced extensive edge corrosion, whereas the surface was nearly resistant to IGC. This was especially evident for the Cu containing alloys without Zn and with 0.21 wt% Zn. By covering the edges, extensive IGC was observed at the surface on the alloys that previously appeared to be resistant to IGC. The completely recrystallised T6 profiles experienced limited edge corrosion, while severe IGC occurred on the surface in susceptible alloys. The corrosion behaviour did not change when the edges were covered. The difference in IGC extent dependent on edge microstructure in the susceptible T5 alloys points towards that the BS-ISO 11846 standard is inadequate to account for edge effects. Furthermore, results indicated that IGC susceptibility increased with increasing Zn content and EDS analysis of the T5 profile with 0.60 wt% Zn revealed a Cu rich film along the grain boundaries, whereas the Zn primarily remained in solid solution. Zn in solid solution might have activated the particle free zone (PFZ) further thus accelerating the IGC mechanism.



# Sammendrag

Vanligvis regnes 6xxx serien (AlMgSi) som motstandsdyktig mot intergranulær korrosjon (IGC) i marint miljø. Kobbertilsetning for å øke maksimal hardhet har derimot vist seg å øke følsomheten for IGC. Den skadelige virkningen på IGC motstanden antas å skyldes dannelsen av et kontinuerlig kobberholdig lag i nanostørrelse begrenset til korngrensene i materialet. Evaluering av IGC følsomhet i utholdbare aluminiumslegeringer blir som regel gjennomført ved metallografiske undersøkelser av prøver etter eksponering i forsured klorholdige saltløsninger. Erfaring har vist at akselerert korrosjonstesting avhenger av en rekke faktorer. Spesielt ekstruderte legeringer med en fibrig mikrostruktur og rekrySTALLISERT overflate har vist seg å være utsatt for kraftig korrosjon fra kantene innover langs fiberstrukturen. Denne observasjonen synes å påvirke omfanget av IGC på den rekrySTALLISerte prøveoverflaten. Ekstruderte kobberholdige AA6082-legeringer modifisert med varierende sinkinnhold ble korrosjonstestet ved BS-ISO 11846 (method B) i temperaturlstandene T5 og T6. Flere paralleller ble utført for å undersøke hvordan kantmikrostrukturen påvirker IGC motstanden i disse legeringene. Virkningen av Zn på IGC følsomheten ble også undersøkt. Lysmikroskopi (LM) ble brukt til å karakterisere mikrostrukturen til T5 og T6 profilene, og sveipetransmisjonselektronmikroskopi (STEM) og energidispersivt spektrometri (EDS) ble brukt til å identifisere og karakterisere den kjemiske sammensetningen på korngrensene i den fibrige mikrostrukturen. Vurdering av korrosjonsfølsomheten ble utført ved metallografiske undersøkelser i LM og sveipeelektronmikroskop (SEM) etter korrosjonstesting. Resultater viste at kantmikrostrukturen hadde en betydelig innvirkning på korrosjonsomfanget på den rekrySTALLISerte overflaten. Korrosjonsutsatte legeringer i T5 tilstand med en fibrig mikrostruktur og rekrySTALLISert overflate opplevde omfattende kantkorrosjon, mens overflaten var tilsynelatende immun mot korrosjon. Dette var spesielt fremtredende for de kobberholdige legeringene uten Zn og med 0.21 vekt% Zn. Ved å tildekke kantene ble omfattende IGC observert på overflaten på legeringer som tidligere virket immune mot IGC. De fullstendig rekrySTALLISerte T6 profilene opplevde begrenset kantkorrosjon, mens omfattende IGC ble observert på overflaten i utsatte legeringer. Korrosjonssadferden i disse legeringene endret seg ikke ved tidekking av kantene. Variasjonen i observert IGC med kantmikrostruktur hos utsatte T5 legeringer, antyder at BS-ISO 11846 standarden er utilstrekkelig når det gjelder hvordan kanteffekter påvirker IGC på overflaten. Generelt økte IGC følsomheten med økende sinkinnhold, og EDS-analyse av en T5 legering med 0.60 vekt% Zn viste en kobberrik film langs korngrensene. Zn derimot forble i fast løsning. Zn i fast løsning kan ha aktivert den partikkelfrie sonen (PFZ) i større grad og dermed akselerert IGC mekanismen.





# Contents

|  |             |
|--|-------------|
| <b>Preface</b>   | <b>i</b>    |
| <b>Acknowledgement</b>   | <b>iii</b>  |
| <b>Abstract</b>  | <b>v</b>    |
| <b>Sammendrag</b>  | <b>vii</b>  |
| <b>List of Abbreviations</b>   | <b>xiii</b> |
| <b>1 Introduction</b>  | <b>1</b>    |
| 1.1 Background . . . . .   | 1           |
| 1.2 Objective . . . . .  | 3           |
| <b>2 Literature review</b>   | <b>5</b>    |
| 2.1 AlMgSi alloys . . . . .  | 5           |
| 2.1.1 Processing route for extruded products . . . . .               | 6           |
| 2.1.2 Microstructure of extruded products . . . . .                  | 8           |
| 2.1.3 AA6082 . . . . .   | 9           |
| 2.2 Age hardening of AlMgSi alloys . . . . .                         | 10          |
| 2.2.1 Precipitation sequence . . . . .                               | 12          |
| 2.2.2 Strengthening mechanisms during artificial ageing . . . . .    | 14          |
| 2.3 Intergranular corrosion of AlMgSi alloys in seawater . . . . .   | 17          |
| 2.3.1 Effect of Cu content and Mg/Si ratio . . . . .                 | 19          |
| 2.3.2 Effect of Zn addition . . . . .                                | 20          |
| 2.3.3 Effect of thermomechanical history . . . . .                   | 21          |
| 2.4 Evaluation of standardised accelerated corrosion tests . . . . . | 23          |
| 2.5 Open circuit potential . . . . .                                 | 25          |
| <b>3 Experimental</b>  | <b>27</b>   |
| 3.1 Materials . . . . .  | 27          |

|          |   |           |
|----------|---|-----------|
| 3.1.1    | Thermomechanical history . . . . .  | 28        |
| 3.2      | Material characterisation . . . . .   | 28        |
| 3.2.1    | Sample preparation and examination in LM . . . . .                              | 29        |
| 3.2.2    | Sample preparation and TEM imaging and analysis . . . . .                       | 29        |
| 3.3      | Hardness measurements . . . . .   | 30        |
| 3.4      | Accelerated IGC test . . . . .  | 30        |
| 3.4.1    | Sample preparation and IGC test execution . . . . .                             | 30        |
| 3.5      | Examination in LM and SEM after IGC test . . . . .                              | 32        |
| 3.6      | Open circuit potential measurements . . . . .                                   | 32        |
| <b>4</b> | <b>Results</b>  | <b>35</b> |
| 4.1      | Microstructure . . . . .  | 35        |
| 4.2      | Effect of microstructure and Zn on hardness . . . . .                           | 38        |
| 4.3      | Accelerated IGC tests . . . . .   | 39        |
| 4.3.1    | Effect of microstructure and alloy content on IGC . . . . .                     | 40        |
| 4.3.2    | IGC on edge covered specimens . . . . .   | 44        |
| 4.3.3    | Effect of surface to edge ratio . . . . .                                       | 48        |
| 4.3.4    | IGC susceptibility on fibre structure . . . . .                                 | 52        |
| 4.4      | SEM imaging of surface after IGC test . . . . .                                 | 54        |
| 4.5      | OCP measurements . . . . .  | 57        |
| 4.6      | Grain boundary analysis and STEM imaging . . . . .                              | 60        |
| <b>5</b> | <b>Discussion</b>   | <b>67</b> |
| 5.1      | Effect of heat treatment and alloy composition on hardness properties . . . . . | 67        |
| 5.2      | IGC susceptibility in AlMgSi(Cu,Zn) . . . . .                                   | 68        |
| 5.2.1    | Effect of Zn on IGC susceptibility in T5 and T6 profiles . . . . .              | 69        |
| 5.2.2    | Effect of Zn on grain boundary chemistry . . . . .                              | 71        |
| 5.3      | Effect of edge corrosion on results retrieved from BS-ISO 11846 . . . . .       | 72        |
| 5.3.1    | Effect of edge microstructure . . . . .   | 72        |
| 5.3.2    | Effect of covering edges . . . . .  | 74        |
| 5.3.3    | Effect of edge to surface ratio . . . . .                                       | 76        |
| 5.3.4    | IGC susceptibility on fibrous region in T5 profiles . . . . .                   | 77        |
| 5.3.5    | Open circuit potential of edge and surface . . . . .                            | 79        |
| 5.3.6    | Practical significance . . . . .  | 80        |
| 5.4      | Further work . . . . .  | 81        |

|   |            |
|---|------------|
| <b>6 Conclusion</b>                                 | <b>83</b>  |
| <b>Bibliography</b>                                 | <b>87</b>  |
| <b>A Depth of recrystallised layer</b>              | <b>95</b>  |
| <b>B Vickers hardness measurements</b>              | <b>97</b>  |
| <b>C SEM imaging of surface corrosion damages</b>   | <b>99</b>  |
| <b>D Diffraction patterns from grain boundaries</b> | <b>103</b> |
| <b>E OCP measurements</b>                           | <b>105</b> |



# List of Abbreviations

|                   |                                     |
|-------------------|-------------------------------------|
| <b>ACT</b>        | Accelerated corrosion test          |
| $\beta$           | Equilibrium phase in AlMgSi         |
| $\beta'$          | Metastable precursor to $\beta$     |
| $\beta''$         | Metastable precursor to $\beta$     |
| $E_c$             | Pitting potential [V]               |
| $E_{\text{corr}}$ | Corrosion potential [V]             |
| <b>EBS</b>        | Electron backscatter diffraction    |
| <b>EDS</b>        | Energy dispersive spectroscopy      |
| <b>GP zones</b>   | Guinier Preston zones               |
| $I_{\text{corr}}$ | Corrosion current [I]               |
| $I_{\text{net}}$  | Net current [I]                     |
| $I_{\text{ox}}$   | Anodic current [I]                  |
| $I_{\text{red}}$  | Cathodic current [I]                |
| <b>IGC</b>        | Intergranular corrosion             |
| <b>L</b>          | Metastable precursor to Q'          |
| <b>LM</b>         | Light microscopy                    |
| <b>OCP</b>        | Open circuit potential [V]          |
| <b>PFZ</b>        | Particle free zone                  |
| <b>Q</b>          | Equilibrium phase in AlMgSi(Cu)     |
| <b>Q'</b>         | Metastable precursor to Q           |
| $R_a$             | Surface roughness [ $\mu\text{m}$ ] |

|                         |   |
|-------------------------|---|
| <b>R<sub>m</sub></b>    | Tensile strength [MPa]  |
| <b>R<sub>p0.2</sub></b> | Yield strength [MPa]  |
| <b>SCE</b>              | Standard calomel electrode  |
| <b>SE</b>               | Secondary electron  |
| <b>SEM</b>              | Scanning electron microscopy  |
| <b>SHE</b>              | Standard hydrogen electrode   |
| <b>SHT</b>              | Solution heat treatment   |
| <b>STEM</b>             | Scanning transmission electron microscopy                                     |
| <b>SSSS</b>             | Supersaturated solid solution   |
| <b>T5</b>               | Artificially aged at 185 °C for 5 h after extrusion                           |
| <b>T6</b>               | Solution heat treated after extrusion and artificially aged at 185 °C for 5 h |

# Chapter 1

## Introduction

### 1.1 Background

Aluminium alloys offer wide application areas ranging from household to industrial implementations, including the building and transportation industry [1]. In order to strengthen its present position as an engineering material, efforts are directed towards how aluminium can replace implementations currently occupied by traditional steel grades. Aluminium alloys provide distinctive properties such as high strength to weight ratio, corrosion resistance, good formability, low level of maintenance and recyclability [1, 2]. In fact, fabricating recycled aluminium constitutes only 5% of the energy required to produce primary aluminium. The automotive industry is currently experiencing conflicting costumer demands such as fuel efficiency without compromising comfort, performance and vehicle size [3–6], whereas governmental policies towards fuel emissions are becoming stricter. Replacing the present global car fleet with new and lighter vehicles has been reported to potentially save 220 metric tonnes of CO<sub>2</sub> emission annually [7]. This number could be increased even further, as newer advances have found that replacing conventional steel with aluminium alloys could result in a weight loss up to 40% without compromising strength [8].

Nevertheless, the main future trend for aluminium is considered to be in structural applications offshore [2]. In the offshore industry, aluminium alloys provide advantages such as ease of manufacturing complex geometries, low maintenance and installation costs, in addition to proven performance in corrosive environments. Higher requirements in terms of strength properties are however a challenge regarding structural aluminium alloys. The 6xxx series (AlMgSi) alloys have excellent corrosion properties in marine environment and satisfactory strength properties. AlMgSi alloys are regarded as medium strength alloys, even after optimisation of alloy composition and thermal processing. However, alloying with copper has proven to increase the ageing response considerably, although the presence of copper has adverse effects on corrosion resistance. Especially the susceptibility to intergranular corrosion (IGC) is enhanced when the alloy is subjected to a corrosive environment [9].

IGC has detrimental effect on mechanical properties and fatigue life. The corrosion damages facilitated by IGC are not readily observed, as the corrosion is initiated at the surface and propagates

deeply into the material through narrow paths along the grain boundaries. The presence of Cu alters the grain boundary chemistry, resulting in the formation of continuous microgalvanic cells along the grain boundaries which causes preferential dissolution of the most active area near the boundaries. In quaternary AlMgSi(Cu) alloys, the mechanism has been explained by the precipitation of a continuous narrow film enriched in Cu confined to the grain boundaries [10–13]. The highly cathodic Cu rich film is believed to accelerate the dissolution of the adjacent solute depleted zone. Excellent corrosion properties are among the advantages that make the 6xxx alloys favourable for offshore applications, although measures to ensure good mechanical properties are important in order to further expand the usage in marine environments. AlMgSi(Cu) alloys with Mg in excess have been reported to experience increased IGC resistance [13]. The improved corrosion resistance is attributed to the presence of a Mg rich film, in addition to the reported Cu film, along the grain boundaries. The Mg film reduces the cathodic nature of the grain boundaries, and the electrochemical potential difference between the boundaries and the anodic solute depleted zone is reduced. Strength properties are however somewhat reduced. Since modification of the driving force for IGC appears to be possible, it has been suggested that alloying with Zn can achieve an analogous effect as excess Mg, though without compromising strength.

Another important aspect of fabricating aluminium alloys for applications in marine environment, is the initial testing procedures that evaluate whether the alloys are suitable for practical use. Standardised accelerated corrosion testing is an effective and inexpensive method to assess corrosion susceptibility, and is widely used among alloy manufacturers and researchers. The standards have specific guidelines which facilitate direct comparison of results, and provide a basis for comparing the susceptibility of alloys relative to one another. Particular factors that affect susceptibility can also be easily identified. Although standardised, the validity of corrosion testing methods should occasionally be assessed as they have previously been found to yield varying results. Results from previous work by the author [14] has implied that IGC testing according to BS-ISO 11846 carried out on extruded copper containing AlMgSi alloys gave unexpected results. Alloys known in literature to be highly susceptible to IGC seemed nearly resistant, and was particularly evident for T5 tempered alloy containing 0.30 wt% Cu. Similar results were also observed in an earlier thesis [15]. The alloys did however experience extensive corrosion on the edges. The IGC susceptibility was finally revealed when the specimens were tested with covered edges.



## 1.2 Objective

The objective of this thesis is to contribute to a better understanding of how edge microstructure affects evaluation of IGC resistance on susceptible alloys by accelerated IGC testing according to BS-ISO 11846. AA6082 alloys received from Hydro Sunndalsøra were used, and the experiments were conducted on profiles water cooled after extrusion. Three alloy compositions with 0.3 wt% Cu and increasing Zn content, in addition to a Cu and Zn free reference sample, were heat treated corresponding to T5 and T6 temper and the microstructure characterised. Four different IGC test parallels were performed to examine how IGC susceptibility varied with microstructure, edge exposure and specimen size. Alteration in hardness properties with heat treatment and alloy composition was recorded, as well as open circuit potential of the fibrous edge and recrystallised surface. Furthermore, the effect of Zn on IGC susceptibility in copper containing AlMgSi alloys was also addressed.



## Chapter 2

# Literature review

### 2.1 AlMgSi alloys

The AlMgSi alloys are primarily alloyed with magnesium and silicon, although trace amounts of other elements are commonly added to improve mechanical properties and optimise microstructure during thermal processing [16, 17]. These alloys are also referred to as the 6xxx series and are categorised as heat treatable wrought alloys, hence they are strengthened by the age hardening process along with being mostly used as wrought products, e.g. rolled plates, extrusions, rods, wires etc. The alloy is cast in ingots and subsequently hot or cold worked mechanically into the desired shape [18]. For a balanced AlMgSi alloy, a Mg/Si ratio of 1.73 is required, calculated from the stoichiometry of its primary hardening constituent  $\text{Mg}_2\text{Si}$ . Further designations for wrought aluminium alloys are listed in Table 2.1.

**Table 2.1:** Wrought alloy designations [16, 17, 19–21]

| Alloy | Primary alloying element(s)           |
|-------|---------------------------------------|
| 1xxx  | Mostly pure aluminium, $\geq 99,00\%$ |
| 2xxx  | Copper                                |
| 3xxx  | Manganese                             |
| 4xxx  | Silicon                               |
| 5xxx  | Magnesium                             |
| 6xxx  | Magnesium and silicon                 |
| 7xxx  | Zinc                                  |
| 8xxx  | Other elements (e.g. iron or tin)     |
| 9xxx  | Unassigned                            |

General characteristic features of the AlMgSi alloys are good formability, weldability, machinability and corrosion resistance. The AlMgSi alloys are regarded as medium-strength structural alloys and do not possess the same high strength properties as the 2xxx and 7xxx alloys [17]. To further optimise the mechanical properties of these alloys, copper is often added in small amounts to increase the strengthening response of the 6xxx alloys beyond what is provided by Mg and Si precipitates. AlMgSi alloys are often found as extruded products due to its high formability, and are accordingly

easily formed to complex geometries. The aforementioned characteristics combined with excellent corrosion properties and high quality surface finish make these alloys suitable for architectural purposes, as well as in structural, building, marine and process-equipment applications [21, 22].

Heat treatable aluminium alloys provide a large range of products due to the various treatments and forming operations that can be applied. The Aluminium Association provides temper designations to categorise the combinations of applicable treatments, as for instance heat treatments and forming operations, in a final product. The first letter indicates a basic treatment or condition, as annealing, solution heat treatment or cold working, while the following suffix letters refers to a secondary treatment used to influence properties further. The T temper is always followed by digits which specify particular treatment sequences. A selection of common T tempers are provided in Table 2.2.

**Table 2.2:** A selection of temper designations for heat treatable aluminium alloys [23].

| Temper | Description   |
|--------|---|
| T4     | solution heat treated and naturally aged                                  |
| T5     | cooled from an elevated temperature shaping process and artificially aged |
| T6     | solution heat treated and artificially aged                               |

### 2.1.1 Processing route for extruded products

Extrusion is a relatively inexpensive and flexible method for producing alloys with complex cross-sections. AlMgSi alloys are highly suitable for extrusion as they are heat treatable; the primary alloying elements Mg and Si are soluble in aluminium at higher temperatures and can remain in solid solution throughout the entire process by immediate quenching after extrusion [24]. If the alloy is immediately quenched after extrusion, the necessity of solution heat treatment as a separate operation is eliminated prior to age hardening [25]. Nevertheless, to reduce the possibility of Mg and Si to precipitate prematurely due to temperature fluctuations during the entire process, the following processing steps have to be carefully executed to acquire the optimum result:

- Melt treatment and casting into billets
- Homogenisation
- Preheating before extrusion
- Extrusion and cooling

An ideal extrusion process is effective and concurrently results in a finished extruded piece with both excellent mechanical properties and a surface finish absent of defects. However, the the risk of introducing surface defects imposes limitations on the overall productivity of the press, especially if the efficiency is measured in terms of extrusion speed. Common surface defects during extrusion include die lines, tearing, surface cracks, pick-ups and local thinning of the cross-section (spalling). An overview of the entire extrusion process with typical time and temperature values is given in Figure 2.1 [26].

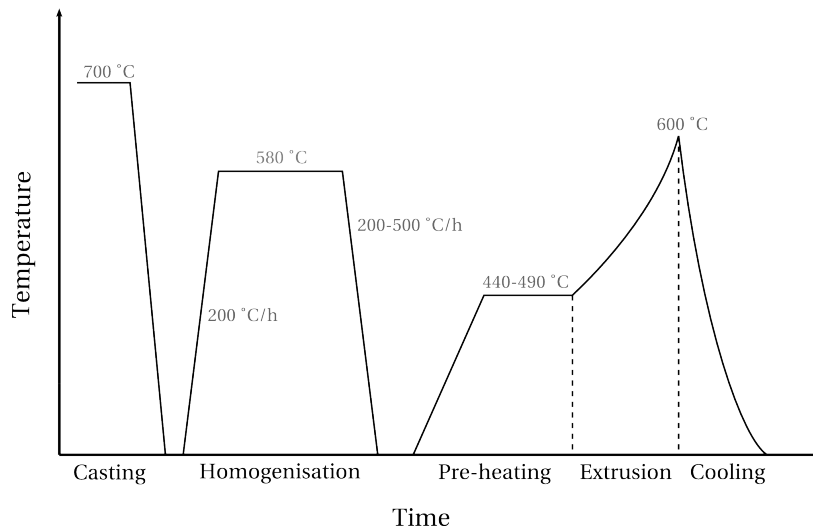


**Figure 2.1:** A schematic illustration of the time-temperature relationship during the different stages of the extrusion process. The indicated values are typical approximated temperatures. Adapted from [26].

### Melt treatment and casting

Before the aluminium melt with the desired chemical composition is cast into billets, a melt treatment is carried out to remove or prevent impurities from forming [27]. Casting can be carried out by several methods, although direct-chill (DC) casting is commonly used as it will provide a desirable uniform ingot structure. The molten alloy is vertically poured into water-cooled moulds, and the solidification process is initiated at the chilled mould wall while the remaining cross-section is solidified by removal of heat by spray cooling from a sub-mould [18].

### Homogenisation

The quality of the as-cast billets are inadequate for extrusion, and will lower workability due to the segregation of grain boundaries, low-melting point eutectics and brittle intermetallic phases after solidification [28]. Furthermore, the precipitation of hardening  $\text{Mg}_2\text{Si}$  precipitates prior to the ageing process will impair the hardenability of the alloy. During homogenisation, the billet is heated an to elevated temperature in the range of 450-600 °C for a sufficient time to even out any

concentration gradients. There are three important parameters during homogenisation; heating rate, homogenisation temperature combined with holding time and cooling rate. A rapid heating rate will risk inadequate dissolution of detrimental phases, which might rather melt when the final homogenisation temperature is reached. Spalling, surface cracks and tearing are caused by local melting reactions in the alloy during extrusion [26]. Slow cooling after homogenisation on the hand, can lead to unfavourable precipitation of  $\text{Mg}_2\text{Si}$ . When the temperature is above 400 °C, coarse  $\beta\text{-Mg}_2\text{Si}$  phases can form at the grain boundaries.  $\beta\text{-Mg}_2\text{Si}$  particles of considerable size do not dissolve readily during extrusion. Thus, a rapid cooling rate is favourable. The holding time during homogenisation depends on the cell size and the rate of diffusion for the alloying elements. A temperature of 565 °C for 6 h has been reported to be suitable for AlMgSi alloys [29]. An important consequence of homogenisation is the transformation of brittle platelike  $\beta\text{-AlFeSi}$  phases to the rounded  $\alpha\text{-AlFeSi}$  phase, phases which serve as nucleation sites for  $\text{Mg}_2\text{Si}$  particles [24, 29, 30].

### Preheating and extrusion

A high preheating temperature will ensure dissolving coarse  $\text{Mg}_2\text{Si}$  particles which do not contribute to strengthening during the ageing process. Lower extrusion speed is then required in order to maintain an acceptable surface finish. During extrusion, the resulting deformed microstructure and texture is dependent on the preheating, die design and extrusion force among other parameters [27]. For the process of hot extrusion, heated billets are being pressed through a die orifice by applied pressure to a ram. The forces exerted on the billet are compressive forces only, effectively reducing the cross-sectional area of the initial billet without causing cracking if the pretreatments are carried out successfully. The finished extruded piece has the desired shape and reduced dimensions [28, 31].

### 2.1.2 Microstructure of extruded products

Aluminium alloys possess a high stacking fault energy, and the deformation during extrusion will create cellular substructures rather than twins or stacking faults due to dynamic recovery [18, 25, 29]. Dynamic recovery occurs when recovery takes place during deformation at elevated temperatures as a result of high dislocation mobility. The subcells differ about 1° in orientation, and the walls are comprised of tangling dislocations. During recovery these subcells will evolve to subgrains in favour of recrystallisation, which provides considerable strengthening. As the extruded piece leaves the die, a strong texture is seen in the longitudinal direction parallel to the working direction, also called the *extrusion effect*. Some static recrystallisation will occur on the surface as the shear zone is more heavily deformed than the core and therefore richer in dislocations. Consequently, the end result is a heterogeneous microstructure [25]. Immediate quenching after extrusion will preserve this microstructure. The specific direction in the grain structure leads

to anisotropic mechanical properties. The strength is approximately 20% higher in the working direction as opposed to the recrystallised layer [18]. An illustration of the recovery and recrystallisation effect during extrusion of aluminium alloys is presented in Figure 2.2.

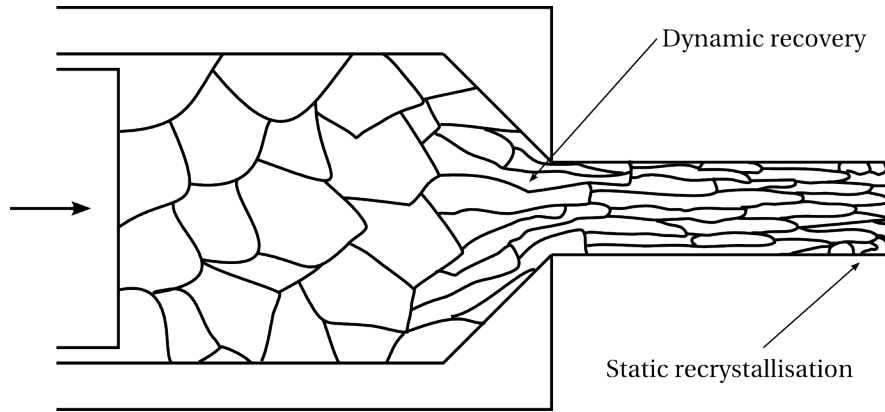


**Figure 2.2:** Dynamic recovery and static recrystallisation during extrusion of aluminium alloys. Reproduced from [25].

### 2.1.3 AA6082

The AA6082 alloy, hereafter referred to as 6082 alloy, is considered to be one of the highest strength alloys among the 6xxx series in addition to having exceptional corrosion resistance due to the low Cu content. In terms of primary alloying elements, the combined level of Mg and Si in the 6082 alloy are usually around < 1.5 wt% , where Si is in high excess. Si in excess lowers the quench sensitivity [23, 29]. Furthermore, the 6082 alloys are known to contain a high level of Mn compared to other alloys in the 6xxx series [29]. Common chemical compositions found in 6082 are listed in Table 2.3.

**Table 2.3:** Typical chemical composition of 6082 alloys in wt% [27].

| Si      | Fe    | Cu     | Mn      | Mg      | Cr     | Zn    | Ti    |
|---------|-------|--------|---------|---------|--------|-------|-------|
| 0.7-1.3 | 0-0.5 | 0-0.10 | 0.4-1.0 | 0.6-1.2 | 0-0.25 | 0-0.2 | 0-0.1 |

The purpose of alloying with Mn is to inhibit recrystallisation by raising the recrystallisation temperature in addition to acting as a grain refiner. This will contribute to improved toughness by maintaining the fibrous grain morphology after extrusion [32]. Alloying with Cr will provide similar effects as preventing nucleation and grain growth [18]. Mn has also a positive effect on corrosion properties since the alloying element is readily incorporated into  $\text{Al}_3\text{Fe}$  and  $\text{Al}_6\text{Fe}$  particles,

transforming them into AlMnFe which have a less detrimental effect on corrosion resistance. Furthermore, Mn dispersoids act as nucleation sites for the hardening  $\beta$ -Mg<sub>2</sub>Si phases. However, the addition of Mn and Cr will lower the extrudability due to increase in quench sensitivity and material flow stress [17, 27, 29]. Fe is generally present as an impurity and is primarily found in particles well distributed in the matrix. Nevertheless, improvement of ductility and toughness is experienced if Fe is present in low concentrations. Some values for selected mechanical properties of the 6082 alloy are as listed [27]

|                    |             |
|--------------------|-------------|
| $R_{p0.2}$         | 275-325 MPa |
| $R_m$              | 300-350 MPa |
| Uniform elongation | 4-6%        |
| Total elongation   | 8-11%       |

Because of the relatively high strength and good corrosion properties of the 6082 alloy, it is a structural alloy used for load-bearing purposes as for instance as constructional material for highly loaded automotive parts or other heavy-duty structures where corrosion resistance is required [33, 34]. Due to high electrical conductivity properties, the alloy is also used for affiliated purposes [16, 27].

## 2.2 Age hardening of AlMgSi alloys

Heat treatable aluminium alloys differ from the non-heat treatable alloys in their ability to increase strength and hardness by the process of age hardening. Age hardening, also known as precipitation hardening, is the process of strengthening metal alloys by the formation of fine and uniformly dispersed secondary phases in the primary matrix after a sequence of heat treatments. The process of age hardening consists of three major operations; solution heat treatment (SHT), quenching and precipitation heat treatment (ageing) as illustrated in Figure 2.3.

Two primary requirements have to be met in order for precipitation hardening to be effective; the solubility of the alloying constituents must be considerable, often at several percent. Secondly, the solubility limit of the alloying elements in the primary phase must decrease rapidly with decreasing temperature [31]. The pseudo-binary phase diagram of AlMgSi alloys meet these requirements, as shown in Figure 2.4. During SHT all primary alloying elements are dissolved upon heating to form a single phase solid solution [31]. In Figure 2.4, this corresponds to the phase field  $\alpha$ -Al which now consists of magnesium and silicon atoms in solid solution with aluminium. The solid solution is then rapidly cooled (quenched) below the solvus temperature to prevent diffusion and the formation of any secondary phases. At this point, the solid solution has become supersaturated with the primary alloying elements and excess vacancies, represented with the phase field  $\alpha$ -Al + Mg<sub>2</sub>Si in



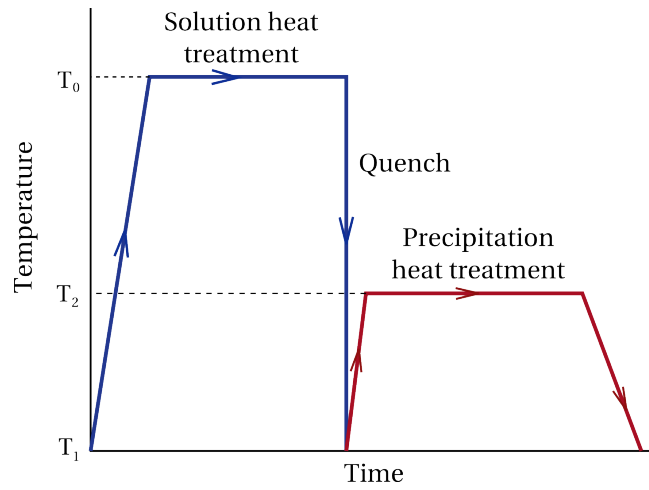


**Figure 2.3:** Schematic illustration of the time and temperature relationship for the age hardening process for solution heat treatment and artificial ageing. Adapted from [31].

Figure 2.4. This solid solution state is also referred to as SSSS (supersaturated solid solution).

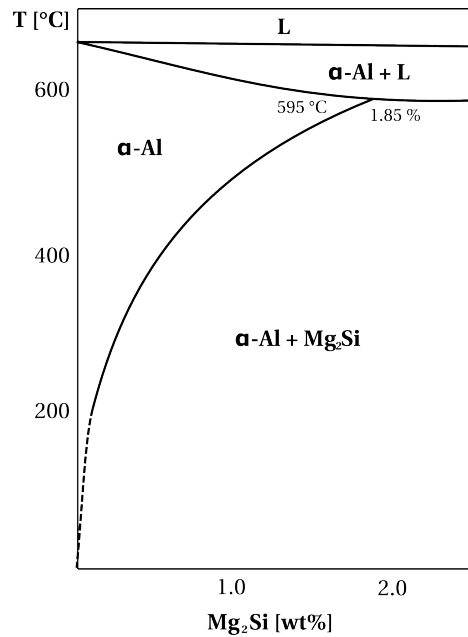


**Figure 2.4:** Pseudo-binary phase diagram for the Al-Mg<sub>2</sub>Si system in a balanced alloy. Adapted from [29, 35–37].

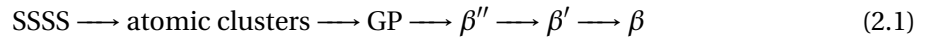
The driving force for precipitation of a secondary phase will depend on the degree of supersaturation and the mobility of the solute atoms with decreasing temperature. For the 6xxx alloys, this precipitation process is relatively slow, although some variations within the alloy series exists [38]. During hot extrusion of 6082 alloys, SHT occurs simultaneously with the extrusion due to the high

temperature facilitated by the process, and immediate quenching after extrusion is sufficient to retain the solute atoms in solid solution at room temperature.

After quenching, the SSSS is in a non-equilibrium state. To accelerate the precipitation process, the non-equilibrium SSSS is reheated to an appreciable temperature for diffusion, where the strengthening particles can precipitate. A suitable temperature is typically around 200 °C, although this process is also time dependent [29]. Higher temperature and longer holding time might risk ageing the alloy beyond peak strength, resulting in overageing and reduced strength properties. The process of accelerating the ageing process by heat treatment is called artificial ageing, although modest strengthening can be achieved by ageing at room temperature for some alloys. Ageing by storing at room temperature is called natural ageing, and the 6082 alloys do achieve some strengthening by natural ageing [38].

### 2.2.1 Precipitation sequence

Detailed information on precipitation in heat treatable aluminium alloys is important for optimising and controlling properties during alloy design. The type of precipitates that are formed is dependent on the heat treatments carried out and the alloy composition [39, 40]. For the AlMgSi alloys, the generally accepted precipitation sequence is given in equation 2.1,



where  $\beta$  is the stable equilibrium phase, while  $\beta''$  and  $\beta'$  correspond to the metastable phases of Mg<sub>2</sub>Si [1, 20, 35, 39, 41–43].

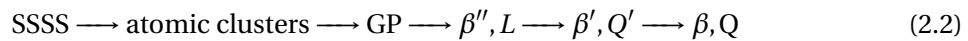
The initial stage of the age hardening mechanism is the formation of excess vacancies as the solute atoms go into solid solution with the primary phase. Subsequent to quenching, solute atoms in the SSSS will diffuse towards the excess vacancies and form clusters of vacancies together with Mg and Si atoms. These clusters act as nucleation sites for the formation of Guinier Preston zones (GP zones), as the solute atoms continue to segregate towards the clusters. A higher quenching rate after solution heat treatment will ensure a higher degree of supersaturation of vacancies, thus a denser and more finely dispersion of GP zones is attained. Consequently, the strengthening potential of the alloy is increased, and higher strength can be achieved upon the formation of the hardening phases. As the age hardening process continues, the GP zones grow into hardening particles [1]. Various suggestions on the morphology of the precipitates exists in literature. The spherical [20, 44] or needle shaped [39, 45, 46] GP zones are fully coherent. The successive precipitates in the sequence however start off as highly coherent and become ultimately incoherent. Highly coherent needle shaped  $\beta''$  phases are nucleated from the GP zones, and are regarded as

the main strength contributing precipitates. The semi-coherent rod shaped [1, 41, 42, 46]  $\beta'$  particles become coarser as the ageing commences, and a drop in strength is observed. Finally, the platelike incoherent  $\beta$ -Mg<sub>2</sub>Si phase is formed, and the equilibrium phase possesses the same FCC lattice as the Al matrix, ordered in an antiferroite structure.

Alloys with high excess Si is known to increase the hardness response compared to a balanced alloy. An apparent reason is that Si in excess will provide sufficient Si to form  $\beta$ -Mg<sub>2</sub>Si, even if a small amount ends up precipitating as elemental Si. In addition, Si has a favourable effect on the nucleation and stability of the atomic clusters [1]. Consequently, Si rich alloys contain a very fine precipitate microstructure and possesses high hardness even though the volume fraction of precipitates is low. The duration of the peak hardness domain during ageing is also prolonged, since both the GP zones and the metastable  $\beta''$  phase are strength contributors, although the latter is the most effective. High Mg alloys on the other hand have a narrower domain for peak hardness, and strength is mainly provided by the  $\beta''$  phase. Consequently, these alloys tend to overage faster than Si rich alloys [47].

### The effect of Cu and Zn addition on precipitation sequence and strength

When Cu is added to AlMgSi alloys, the original precipitation sequence will be altered as Cu is incorporated into the precipitates and form new phases. However, predicting the exact resulting precipitation sequence has been found difficult, since the precipitates change to some extent with varying alloy composition, primarily related to the Mg/Si ratio and the Cu content. Regardless, the stable quaternary Q phase and its metastable constituents will enter the original sequence [41]. The exact chemical composition of the Q phase and its precursors is not fully established yet, although they are known to consist of the main alloying elements in the alloy. Following compositions have been suggested: Al<sub>5</sub>Cu<sub>2</sub>Mg<sub>8</sub>Si<sub>6</sub>, Al<sub>4</sub>CuMg<sub>5</sub>Si<sub>4</sub>, Al<sub>4</sub>Cu<sub>2</sub>Mg<sub>8</sub>Si<sub>7</sub>, Al<sub>3</sub>Cu<sub>2</sub>Mg<sub>9</sub>Si<sub>7</sub> [41, 44]. A condensed precipitation sequence for AlMgSi(Cu) alloys is presented in equation 2.2,



where  $\beta$  and Q are the stable equilibrium phases, while L and Q' represent metastable precursors to the Q phase, and  $\beta''$  and  $\beta'$  are metastable precursors to the  $\beta$ -Mg<sub>2</sub>Si phase [39, 41].

The Q' and Q phase have been frequently reported in these alloys, although they have been mainly associated with overaged conditions and will only appear after prolonged ageing at elevated temperatures [44]. Instead, the main strength contributors are rather ascribed to the lath-shaped L phase, a precursor to the Q' phase, in combination with the  $\beta''$  phase in quaternary alloys [41, 45]. In fact, it has been reported that the  $\beta''$  phase only accounted for 20-30% of the precipitated phases in a peak hardened alloy, indicating that the strength contribution primarily originated from GP

zones and Q' precursors [39]. The presence of Cu in AlMgSi alloys raises hardness and tensile properties due to finer precipitate microstructure and dispersion, in addition to providing higher precipitate volume fraction by accelerating the formation of GP zones and  $\beta''$  [39, 44]. Furthermore, it has been reported that maximum thermal stability in AlMgSi(Cu) is achieved when the L phase is present [45], and the mechanism has been explained by the retarding effect Cu has on precipitate growth when it segregates to the particle interface [48].

Research on how the addition of Zn affects the precipitation sequence and strength properties in copper containing AlMgSi alloys is limited, although there have been studies on the effect of Zn in Cu free AlMgSi alloys. According to a study by Saito et al. an addition of 0.1 wt% Zn did not have a measurable influence on precipitate microstructure or mechanical properties [46]. Alloying with 1 wt% Zn on the other hand resulted in a slight increase in hardness. This was attributed to solid solution strengthening, since more Zn was found in solid solution, in addition to an increase in precipitate number density. Raising the Zn level to 1 wt% did however not alter the precipitation sequence, although it caused the precipitates to become more disordered. Small amounts were also incorporated in the existing precipitates. Nevertheless, the alloying element primarily remained in solid solution with the Al matrix. Zn is known to have a remarkable solubility in Al, up to as high as 82.8 wt% [18].

### 2.2.2 Strengthening mechanisms during artificial ageing

The overall strengthening during ageing is attributed to impediment of dislocation movement through various mechanisms. The exact strengthening mechanism during the ageing process will depend on particle size, distribution and coherency of the precipitates. Furthermore, these parameters depend on the temperature and time elapsed during artificial ageing [17, 19, 20]. The relationship between time and strength development is often divided into three domains for heat treatable alloys, indicating the conditions found during the ageing process; underaged, peak-aged and overaged. Maximum hardness and tensile properties are achieved in the peak-aged condition, whereas prolonged ageing prove detrimental to these properties. However, overageing will increase resistance to SCC, fatigue crack growth and improve dimensional stability [49]. Three strength mechanisms act during ageing: *coherency strain hardening*, *chemical hardening* and *dispersion strengthening*. The mechanisms can exist simultaneously in an alloy and are not mutually exclusive. All mechanisms and their time of appearance and combined strength contribution will yield an ageing curve where each stage represents a ageing condition, as seen in Figure 2.5. Solid solution strengthening is not a significant strength contributor during ageing since the amount of solute atoms will decrease as they are incorporated into the hardening phases and particles in the course of ageing.

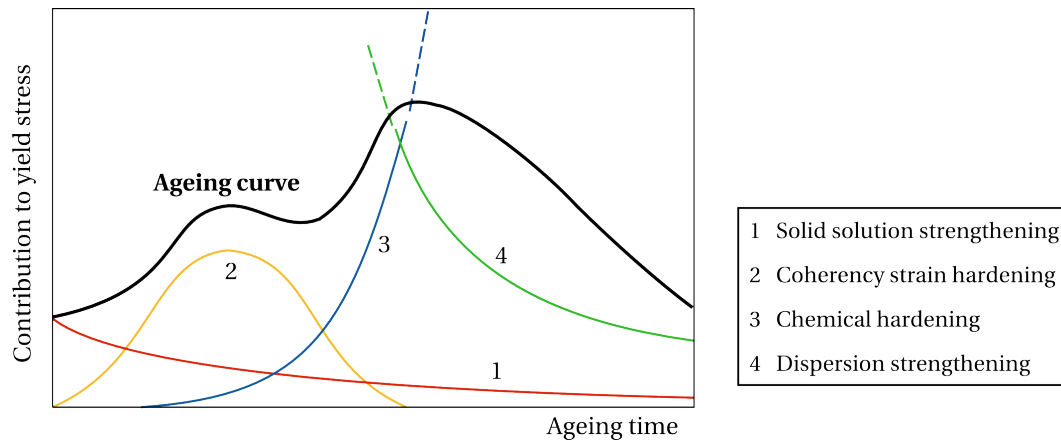


**Figure 2.5:** Illustration of a typical ageing curve for heat treatable aluminium alloys. Reproduced from [50].

### Coherency strain hardening

The initial coherent phases and clusters will create a surrounding strain field as a consequence of the deviation in size between the coherent phase and the solvent phase, as illustrated in Figure 2.6. Strain fields stabilise dislocation movement by obstructing and retarding the mobility of dislocations. Hence, an increase in hardness and yield strength is expected. The degree of strengthening depends on the number, size and spacing between the precipitates. Generally, as the ageing time progresses, the particles become larger and the particle spacing increases. The maximum strength provided by coherency strain hardening is reached when the average zone separation equals the limiting radius of the dislocation curvature. Early on, the particles are too small and finely spaced to properly inhibit dislocation movement, since the line defects cannot bend around all the strain fields. The reduction in strength during coherency strain hardening is caused by too widely spaced particles as the ageing continues [50].

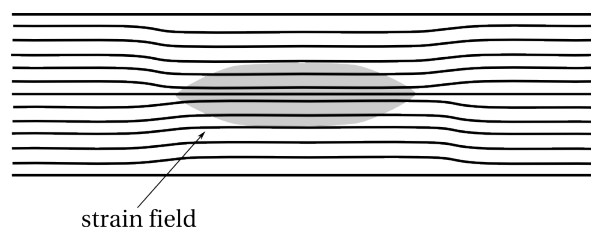


**Figure 2.6:** Strain field created from the matrix distortion caused by a coherent particle. Adapted from [18].

### Chemical hardening

Chemical hardening is also exhibited by coherent particles. This mechanism is caused by the increase in required force exerted by dislocations to cut or shear through a coherent phase or parti-

cle, due to the rise in surface area energy relative to the remaining matrix [1]. Further ageing will render the particles less coherent as they increase in size, and the ability to strengthen by chemical hardening diminishes [50]. Moreover, once the particle is cut, dislocations tend to continue to shear through a few selected active slip planes. The dislocations pile up and become highly localised, which may result in a micro-crack if the concentration is found near a grain boundary [18]. An illustration of the hardening mechanism is shown in Figure 2.7.

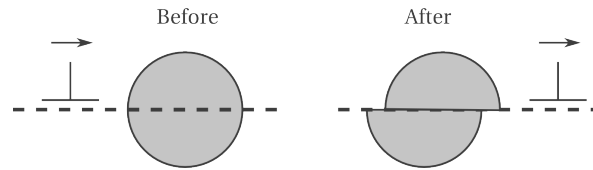


**Figure 2.7:** Representation of a dislocation shearing through a coherent particle. Reproduced from [51].

### Dispersion strengthening

While the coherency of the particles becomes semi-coherent and incoherent with the Al matrix, dispersion strengthening becomes the prominent mechanism for strengthening. Due to the incoherency, dislocations cannot continue to cut through the particles and are forced to divert by mechanisms as for instance Orowan bowing or looping, seen in Figure 2.8. The dislocation line is extruded through precipitates and creates dislocation rings around the precipitates after passing [52]. These rings become denser as more dislocations pass, and the rate of work hardening increases [1, 50]. Over time, the particles will coarsen and the dispersion hardening mechanism will become less effective.

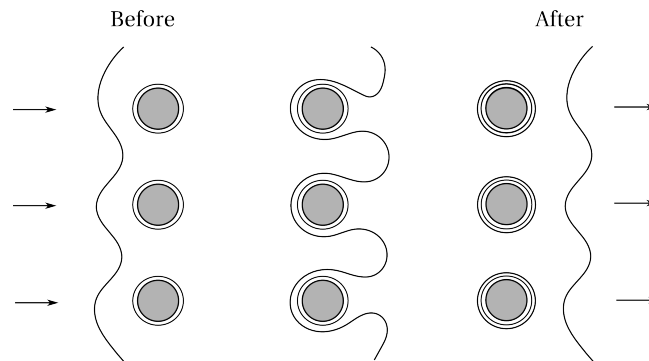


**Figure 2.8:** Illustration of Orowan looping. Dislocation lines create dislocation rings around the incoherent particles after passing. Adapted from [18, 51].

## 2.3 Intergranular corrosion of AlMgSi alloys in seawater

Table 2.4 lists the corrosion potential in an acidified salt solution for a selection of metals and alloys. According to the table, aluminium alloys are one of the most reactive ones among common engineering metals and alloys.

**Table 2.4:** Selected corrosion potentials at 25 °C with reference to a 0.1 N calomel electrode in a 53 g/L NaCl, 3 g/L H<sub>2</sub>O<sub>2</sub> solution [23].

| Metal                             | Corrosion potential<br>$E_{corr}$ [V] (SCE) |
|-----------------------------------|---|
| Nickel                            | +0.01                                       |
| Stainless steel                   | -0.01                                       |
| Copper                            | -0.12                                       |
| Brass (60-40)                     | -0.20                                       |
| Low-carbon steel                  | -0.50                                       |
| Aluminium alloys 1xxx, 3xxx, 6xxx | -0.72 to -0.75                              |
| Aluminium alloys 5xxx             | -0.77 to -0.79                              |
| Aluminium alloy 7072              | -0.88                                       |
| Zinc                              | -1.02                                       |
| Magnesium                         | -1.65                                       |

Conventional AlMgSi alloys are regarded to have excellent corrosion properties in atmospheric conditions, and are also considered corrosion resistant in seawater [53,54]. The high corrosion resistance is due to the spontaneous formation of a passivating Al<sub>2</sub>O<sub>3</sub> film when the alloy is in contact with oxygen. However, since aluminium is easily oxidised, it depends entirely on the passive film in order to prevent corrosion initiation. The reactivity of aluminium poses challenges as the matrix is generally more anodic to the intermetallic compounds originated by the alloying elements in the material. Galvanic coupling between the matrix and heterogeneities generates local microgalvanic cells, which serve as initiation sites for corrosion. The mode of corrosion is dependent on the precipitate microstructure and alloy content in absence of a passive film. Consequently, alloy composition and thermomechanical history are crucial to the corrosion behaviour of AlMgSi alloys. AlMgSi alloys are most susceptible to pitting corrosion and intergranular corrosion in seawater [55].

Alloying AlMgSi alloys with Cu reduces the corrosion resistance significantly, as Cu is appreciably soluble in aluminium as well as being more noble to the remaining matrix. If corrosion is initiated, the more active Al matrix will corrode at a faster rate, while the Cu containing heterogeneities at the surface will become more nobly enriched and ultimately act as local cathodes [56]. The described mechanism is particularly important in marine environments with regard to pitting cor-

rosion, where the presence of chloride ions can destabilise the aluminium oxide by reducing the critical pitting potential  $E_c$ . The  $E_c$  value does not directly depend on the pH of the bulk solution, but rather on the activity of the chloride ions, solution temperature and the alloy composition. Noble soluble constituents as Cu that favour high rates of reduction reactions combined with high chloride ion activity that lowers the  $E_c$  value are detrimental conditions for corrosion resistance. Weak areas where the passive film has ruptured and left exposed cathodic inclusions are initiation sites for localised corrosion attacks. After corrosion initiation, whether the attack propagates as pitting corrosion or intergranular corrosion (IGC) is highly dependent on the prior thermomechanical history of the alloy.

Heat treatable aluminium alloys are commonly susceptible to intergranular corrosion to some extent as a consequence of the heat treatments carried out to optimise the age hardening potential. In general, intergranular corrosion is the preferential dissolution of material along the grain boundaries due to coupling between zones with a difference in electrochemical potential, giving rise to microgalvanic cell action. Solute atoms tend to diffuse towards grain boundaries when the temperature is sufficiently elevated, since the grain boundaries are more favourable diffusion paths than the grain itself [57]. The disordered nature of the grain boundaries make them also suitable sites for heterogeneous precipitation. Solute atoms may form phases which are more noble or active to the remaining aluminium matrix. As precipitation along grain boundaries occurs, the adjacent area is rendered depleted of solute atoms and becomes more active or cathodic to the precipitated phase at the grain boundary. This area is often called the particle or precipitate free zone (PFZ).

Clearly, concentration and alloying species will determine the severity of IGC. In order to initiate IGC, intermetallic particles must precipitate continuously along the grain boundaries, providing paths where the corrosion can propagate. Also, a corrosive media must be present, as well as an electrochemical potential difference of 100 mV between the two galvanic coupled zones [53]. The microgalvanic coupling can be between [58]

- matrix and grain boundary precipitates
- matrix and PFZ
- grain boundary precipitates and PFZ

IGC is initiated at external cathodes on the surface and will start off as pitting. No correlation between pit depth or width has been found however, which indicates that IGC can originate from both shallow and deeper pits. The mass loss related to IGC is low, and the corrosion damage itself cannot be observed by the naked eye. Although IGC is initiated by cathodic inclusions at the surface, internal cathodes provide the most significant driving force for the propagation of IGC. The distance between external inclusions and anodic sites increases with the extent of IGC propagation, hence an increase in ohmic resistance in the galvanic system would be expected. Thereof,



external cathodes are not sufficient to maintain the rate of propagation observed in susceptible alloys [11, 59]. Extensive IGC propagated to the bulk material can have detrimental effects on mechanical properties, especially loss in elongation and thereafter loss in strength [53, 58]. Furthermore, the sharp tips of IGC attacks can act as substantial stress risers and have adverse effects on fatigue life [60]. IGC has also been claimed to be confined to the recrystallised layer of the extruded material [61–63]. Consequently, thin structures are more susceptible to failure than thicker ones. The thickness of the recrystallised layer is however dependent on the cooling rate after solution heat treatment or hot deformation.

### 2.3.1 Effect of Cu content and Mg/Si ratio

Published research from the recent years has unanimously established that the presence and increased level of Cu have the largest impact on raising IGC susceptibility in AlMgSi(Cu) alloys [9, 11, 64]. The exact mechanism on how the occurrence of Cu accelerates IGC has nonetheless been somewhat disputed. It has been previously proposed that the increase in IGC severity was governed by the extensive precipitation of Q'/Q phases, cathodic to the anodic solute depleted zone, along the grain boundaries [9]. Mg<sub>2</sub>Si precipitates anodic to the copper containing matrix has also been reported to be a probable cause of IGC [65]. Nevertheless, these particles are precipitated discreetly and discontinuously alongside the grain boundaries, which is insufficient to account for the observations of sharp and continuous IGC attacks on susceptible alloys [10]. Moreover, the Q phase has shown to be richer in Mg and Si relatively to Cu [10, 13], confirming the ambiguity of the Q precipitates as the source for increased susceptibility in AlMgSi(Cu). It has also been stated that the Q phases are ineffective as cathodes when it comes to initiating corrosion in these alloys [12].

More recent research has conversely revealed the existence of a seemingly continuous nanoscale Cu-enriched layer deposited along grain boundaries [10–13, 66–68]. The Cu-enriched film is considerably more cathodic than the solute depleted zone, and the coupling of these areas in corrosive media substantiates the formation of continuous microgalvanic cells along grain boundaries better than the previously reported Q/Q' precipitates. Kairy et al. detected a 2 nm wide Cu enriched film in a AlMgSi alloy containing 0.89 wt% Cu, and the observed PFZ was found to consist mainly of aluminium [68]. Although Cu is primarily detected in the film, thermodynamic calculations reveal that elementary Cu cannot be formed at the present heat treatment temperatures and alloy composition, i.e. the film has been suggested to be a precursor variant to the Q' phase [10] or non-equilibrium Cu in solid solution [67]. AlMgSi alloys containing as low as 0.12 wt% Cu has shown susceptibility to IGC [9], though the severity is highly dependent on thermomechanical history, an aspect which will be elaborated further in successive sections.

Moreover, how the primary alloying elements Mg and Si affect IGC resistance has also been elaborated. Especially  $\beta$  phases and elemental Si particles have been claimed to influence the resistance

in a negative direction, where it has been proposed that Mg is leached out of these phases, rendering Si particles that are highly cathodic to the Al matrix [69]. On the contrary, others have argued that Si particles will spontaneously form inert  $\text{SiO}_2$  when in contact with oxygen, which will yield a passivating effect as opposed to an active one [11]. Larsen and Nisancioglu [70] reported that a Cu free alloy with a Mg/Si ratio of 0.83, which is Si moderately in excess, did not experience any IGC. Nevertheless, excess Si alloys have been observed to experience increased corrosion rates when Cu is present in contrast to balanced alloys.

Liang et al. did a comprehensive study where the combined effects of Cu content and Mg/Si ratio on IGC behaviour in AlMgSi were evaluated [64]. This research concluded that increasing Cu content evidently had the largest impact on the severity of IGC, though an alloy ratio with Mg in excess showed improved IGC resistance to some extent. Conversely, a higher excess of Si had the opposite effect and has a slight detrimental effect. The improved IGC resistance by alloying with Mg in excess has later been confirmed by Holmestad et al. [66], where a Mg/Si ratio of 2 proved to reduce the severity of IGC attacks. STEM imaging and EDS elemental mapping indicated that the reduction of IGC was owed to the precipitation of a continuous film consisting of both Cu and Mg. Mg is believed to reduce the cathodic potential of the Cu layer, concurrently reducing the driving force for IGC. Even though alloying with Mg in increased amounts can slow the propagation of IGC, this will lower mechanical properties as formability, extrudability and strength [69].

### 2.3.2 Effect of Zn addition

How the addition of Zn to AlMgSi(Cu) alloys affects the IGC behaviour has not been extensively reviewed in current literature, however, some research exists. First and foremost, alloying with Zn in a high-purity alloy will direct the solution potential towards a more active direction [17]. A study by Yamaguchi and Tohma concluded that by alloying with Zn in appropriate amounts to an AlMgSi alloy containing 0.2 wt% Cu, the extent of IGC was reduced [65]. This was evident for alloys tested by galvanostatic polarisation after SHT and water quenching in addition to a brief baking treatment at 170°C. The conclusion from this work was based on the assumption that the observed IGC was owed to the anodic  $\beta\text{-Mg}_2\text{Si}$  phases precipitated at the grain boundaries coupled with cathodic grain bodies with Cu in solid solution. The dissolution potential of the alloy reached the potential of the  $\text{Mg}_2\text{Si}$  phases when 0.1 wt% Zn was added, i.e. preferential dissolution was avoided. However, Zn amounts exceeding 0.1 wt% introduced IGC. Other research has experimented with adding Zn to copper free AlMgSi alloys. Saito et al. did a study where a Zn content of 1 wt% led to segregation of Zn to the grain boundaries for the peak aged temper, though the IGC susceptibility was consequently increased due to coupling between the highly anodic Zn rich film and the nobler grain body [46].

In light of this result, alloying AlMgSi(Cu) with Zn might achieve the same effect as observed by

Holmestad et al. [66] where the IGC resistance was improved by the combined effect of a Mg and Cu layer at the grain boundary. This is a part of the objective of this present study. Since Zn is not readily incorporated in the particles, according to Saito et al. [46], the alloying element might rather segregate together with Cu and form a continuous layer at the grain boundary and reduce the cathodic nature of the Cu film. Hence a lower potential difference between the boundaries and the PFZ would be achieved, resulting in a lower driving force for corrosion. Furthermore, Zn was not observed to have detrimental influence on strength, as opposed to Mg, but had a modest effect on raising the hardness due to solid solution strengthening [46].

### 2.3.3 Effect of thermomechanical history

Another important feature that affects IGC susceptibility in heat treatable alloys is thermomechanical history. Thermomechanical history involves metallurgical procedures as deformation processes, quenching and heat treatments such as SHT and artificial ageing.

The cooling rate after SHT, either if it is done during hot deformation or as a separate process, affects the subsequent precipitation and diffusion of alloying elements. Slow cooling rates, e.g. air cooling, allow for more diffusion of elements since the temperature is appreciably high for longer times. This will result in more precipitation along grain boundaries of as-quenched materials and thus affect the succeeding ageing process. For materials used in the natural or peak-aged condition, slow cooling rates can have detrimental effect on IGC resistance as more precipitates and phases cathodic to the PFZ is located along grain boundaries. For more rapid quenching, often achieved with water quenching, phases detrimental to IGC resistance will have insufficient time to precipitate and the IGC susceptibility can be reduced. However, higher quenching rates are not always easily carried out, especially for thicker sections. High quenching rates may also induce undesirable residual stresses within the material [58], although water quenching will provide better hardness compared to air cooling [63]. Nevertheless, assessing the cooling rates as an isolated effect on IGC is often not expedient as the final corrosion properties result from the combination of cooling rates and artificial ageing.

The heating temperature during the ageing treatment facilitates the precipitation of the hardening phases in the alloy, and has therefore a prominent effect on the IGC behaviour. The initial stage of age hardening will introduce precipitation of particles, whereas continued ageing will alter their size, distribution and chemical composition. During this process, detrimental phases to IGC may form and precipitate along grain boundaries. The corrosion morphology is not only dependent on whether the alloy is underaged, peak-aged or overaged but also on the quenching rate prior to ageing. In a study by Svenningsen et al. [63], air cooled alloys containing 0.17 wt% Cu was found to suffer from extensive IGC in the natural and underaged condition. Further ageing led to more localised IGC and finally developed into pitting when the overaged domain was reached. The al-

loys were nearly resistant to IGC and corrosion in general around the peak-aged condition. Water cooled alloys on the other hand experienced pitting in the natural aged condition, whereas IGC was introduced when the alloy was underaged. Continued ageing reduced the extent of IGC, although the occurrence of IGC was not completely eliminated. The decrease in IGC with ageing time is believed to be caused by diffusion which render phases or particles coarser, in addition to discontinuation of the Cu rich grain boundary film. Cu from the boundary segregates towards the particles and consequently reduces the electrochemical potential difference between the boundary and the PFZ, and the disruption of the continuous film might explain the transition from IGC to pitting.

Additional solution heat treatment after extrusion has been reported to slightly increase IGC susceptibility [63]. It has been proposed that precipitation kinetics related to dislocation density might be the cause. Deformed and stretched materials have a higher dislocation density which will accelerate the precipitation process. Coarser precipitates are therefore expected. Solution heat treatment on the contrary, will anneal out dislocation to a larger extent. The coarse precipitates lead to pitting when the alloys are overaged, whereas solution heat treated alloys experiences IGC instead. Increasing solution heat treatment temperature has also been reported to increase IGC susceptibility to a small extent [71], though strength properties are slightly improved.

For materials with a characteristic fibrous structure, as depicted in Figure 2.9, slower cooling rates will increase the depth of the recrystallised layer, which is another feature that has been reported to affect IGC susceptibility. It has been suggested that IGC is predominately found in the recrystallised layer of materials which have a strong texture in the centre, and that the propagation of IGC seems to stop when the fibrous grain structure is reached [63].

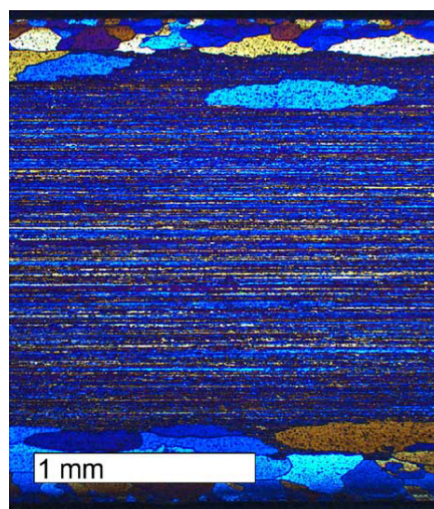


**Figure 2.9:** Characteristic microstructure for extruded air cooled 6xxx alloys [9].

The observation has been related to grain boundary angles; high angle boundaries are more favourable sites for extensive precipitation whereas low angle boundaries are found to have less precipitation [61, 62]. This might provide an indication of why IGC is often observed to be confined to the recrystallised layer, and why air cooled alloys often display deeper corrosion attacks. However, corrosion at highly directional textures in heat treatable aluminium alloys is not unfamiliar, as it is very common among the 2xxx and 7xxx series. This corrosion mechanism is called exfoliation corrosion since the accumulation of corrosion products may lift and delaminate the metal surface, and is governed by the same general mechanism as IGC. Exfoliation like attack was observed in copper containing 6xxx alloys by Eckermann et al. [72], although the exfoliation like attacks seemed to propagate independent of grain boundaries.

## 2.4 Evaluation of standardised accelerated corrosion tests

Standardised corrosion tests contribute to the basis of predicting the service life and practical corrosion control of components in specific service environments [73, 74]. Three types of corrosion testing exist; laboratory tests, field tests and service tests. Specimens used in field and service tests are subjected to long term exposure in actual conditions that are expected during service, although field tests often use test coupons whereas service tests may use manufactured components subjected to more specific service environments [74]. Standardised accelerated corrosion tests (ACT) are commonly laboratory tests which provide test procedures with specific guidelines to avoid dispersion in results [53]. The standards are developed by technical societies, standard institutions or even industrial manufacturers, and are frequently used in research and the industry since in-field tests are more expensive and demanding while time-consuming.

Accelerated laboratory tests are conducted under precisely defined and controlled conditions, and make it possible to identify separate effects among numerous of factors which influence corrosion behaviour, as for instance thermomechanical history, alloy composition, environmental composition, temperature etc. This also enables direct comparison of corrosion susceptibility on different alloys tested in identical conditions. The acceleration of the tests is often done by intensifying one or several factors to increase the corrosion rates, in other words by increasing the aggression of the corrosion media. This may involve increasing acidity, salt concentration, pressure and temperature [74, 75]. Accelerated immersion tests are the most simple ACTs, and they provide a quick and economical method to screen and eliminate alloys from further consideration. Results from such tests are highly qualitative where metallographic examination is the conventional method for assessing corrosion damages, in combination with simple quantitative measurements as mass loss and corrosion depth [53, 76]. Metallographic examination of corroded specimens involving cutting and polishing can however lead to grain fallout during sample preparation or the risk of introducing artefacts [72].

The validity of standardised ACTs is widely recognised in scientific research, though it is important to occasionally confirm the reliability of such tests. One major disadvantage of these accelerated immersion tests is the difficulty of extrapolating the results to predict the lifetime of the tested alloys in actual service [75]. The aggressiveness of these tests can also result in alloys failing the ACT, though later prove to be satisfactory during service in the actual environment. Moreover, standardised ACTs in general provide no model which can relate laboratory tests to how long-term corrosion in operating conditions affect mechanical properties, however this matter is beyond the scope of this work.

Standardised ACTs designed for evaluating IGC in aluminium alloys include ASTM G110 and BS-ISO 11846. Both of these immersion tests are widely used to examine susceptibility to IGC in heat treatable aluminium alloys [77, 78]. The amount of studies on evaluating consistency of ACTs with in field tests are limited, though some research has been done. Bauger and Furu [79] compared long-term exposure tests in the field with several ACTs, including ASTM G110, SWAAT (cyclic salt spray test) and VDA (cyclic test used in the automotive industry). Samples were field tested in atmospheric marine environment for 2.8 and 5.8 years, and the extent of corrosion from the field tested specimens correlated well with the IGC test. Mass loss measurements from the field specimens showed similar trends for both SWAAT and VDA, although the mass loss was significantly higher for the field tested samples compared to the VDA test [79]. Svenningsen et al. [9] evaluated the BS-ISO 11846 standard by comparing laboratory test specimens with samples exposed from six to 24 months. The results revealed that the corrosion damages were more severe on the ACT samples, indicating that the BS-ISO 11846 subjected the specimens to more extreme conditions than provided by 24 months of exposure in natural marine atmosphere.

As stated in the BS-ISO 11846 standard, its main purpose is to highlight how alloy composition and thermomechanical history affect the susceptibility to IGC. Correct usage of the test entails that sensitivity to IGC is assessed relatively among the selected test specimens [78]. Consistent material preparation and dimensions are important for comparisons to be valid. IGC testing should be carried out in a manner such that any reasonably susceptible alloys are discovered. For instance, occurrence of extensive corrosion from the edges on highly directional deformation structures is common for alloys sensitive to corrosion. Subsequent to testing, the results will strongly indicate that susceptibility to corrosion is evident, although the corrosion mode on the surfaces of interest might be concealed due to preferred corrosion of the edges. Conversely, alloys with identical composition with a microstructure absent of the characteristic directional texture might exhibit extensive corrosion on the surfaces. This correlates poorly with realistic application as cut edges are seldom designed to be exposed when in service. The BS-ISO 11846 does not require edges to be covered during testing.

## 2.5 Open circuit potential

A metal immersed in a corrosive media will often in practice experience both reduction and oxidation reactions at the metal surface. The theoretical net current  $I_{net}$  would represent the combined effect of the anodic and cathodic current as expressed in equation 2.3 [80]

$$I_{net} = \Sigma I_{ox} - \Sigma |I_{red}| \quad (2.3)$$

The corrosion rate is governed by the sum of all partial currents which cause metal dissolution, i.e. the anodic currents on the surface  $I_{ox}$ , as shown in equation 2.4

$$I_{corr} = \Sigma I_{ox} \quad (2.4)$$

Considering the case that no net current is present,  $I_{net} = 0$ , the anodic current and the cathodic current will be equal in magnitude according to equation 2.5, and the measured potential is called the open circuit potential (OCP). Furthermore, since the metal corrodes without any external current, the OCP value will equal the corrosion potential of the metal,  $E_{corr}$  as seen in equation 2.6.

$$I_{corr} = \Sigma I_{ox} = \Sigma |I_{red}| \quad (2.5)$$

$$E = E_{corr} \quad (2.6)$$

$E_{corr}$  is determined solely by kinetics, i.e. the rates of the reduction and oxidation reactions occurring on the surface, in contrast to the equilibrium potentials of each partial reaction which is based on thermodynamic calculations [81]. The corrosion potential is easily measured by breaking the circuit or adjusting the power source, and is measured against a reference cell [80]. The practical significance of  $E_{corr}$  is important, as the potential difference between two coupled metals can cause preferential dissolution of the metal possessing the lower potential. This mechanism is also applicable for heterogeneities with potential differences within the same alloy, as already elaborated on the mechanism of IGC in section 2.3. However, the measured OCP of the entire alloy specimen will be a combination of the individual potential contributions from the matrix and the heterogeneities.





## Chapter 3

# Experimental

### 3.1 Materials

The materials used for testing were provided by Hydro Sunndalsøra and were received as homogenised bolts and examined as extruded profiles. The chemical composition of the bolts are listed in Table 3.1.

**Table 3.1:** Chemical compositions of examined 6082-profiles given in wt%.

| Profile   | Serial no. | Mg   | Si   | Fe   | Mn   | Cu   | Zn   |
|-----------|------------|------|------|------|------|------|------|
| <b>1a</b> | <b>W-3</b> | 0.67 | 1.04 | 0.19 | 0.54 | 0.00 | 0.00 |
| <b>4a</b> | <b>W-3</b> | 0.66 | 1.04 | 0.20 | 0.53 | 0.30 | 0.00 |
| <b>4b</b> | <b>W-2</b> | 0.66 | 1.02 | 0.20 | 0.55 | 0.31 | 0.21 |
| <b>4c</b> | <b>W-2</b> | 0.65 | 1.02 | 0.19 | 0.54 | 0.31 | 0.60 |

Each profile had varying levels of Cu and Zn, while the Mg, Si, Fe and Mn content were kept fairly constant. Profile 1a did not contain any Cu and Zn and was used for referencing. Profile 4a contains 0.30 wt% Cu without Zn, whereas profile 4b and 4c contain 0.31 wt% Cu and medium and high Zn level, respectively 0.21 wt% and 0.60 wt% . The serial number of the profiles indicates where in the extruded profile the test materials were taken from. Serial numbers W-2 and W-3 indicate that the profiles originated roughly from the middle of the total extruded piece, where extrusion processing parameters have stabilised. In general, these modified copper containing 6082 alloys have a Mg/Si ratio of approximately 0.64, i.e. Si is in excess.

### 3.1.1 Thermomechanical history

The aluminium melts with the chemical compositions listed in Table 3.1 were produced at Hydro Sunndalsøra and cast at 700 °C into 95 mm bolts and ~1.2 m length. Afterwards, the bolts were homogenised by heating to a temperature of 575 °C with a heating rate of 100 °C/h, and held for 2 h and 15 min. After homogenisation, the bolts were cooled to room temperature with a cooling rate of 249 °C/h, and cut into lengths of 20 cm. The mentioned procedures in were carried out at Hydro Sunndalsøra.

Extrusion of the homogenised bolts from Hydro Sunndalsøra were extruded at NTNU, Trondheim with the SINTEF vertical laboratory press. The bolts were extruded into bars with a cross-sectional area of 3 x 65 mm, into a water filled pipe which served as water quenching. Extrusion temperature was kept at 533-520 °C. The bars were then cut into sections and given a serial number according to placement and subsequently stored in a freezer.

Each profile was thermally processed to the T5 and T6 temper. The T5 samples were artificially aged directly from the as-extruded condition, 20 min after the sections were taken out of the freezer. Afterwards, the sections were then artificially aged in an oil bath at 185 °C for 5 h. For the T6 samples, the sections were solutionised prior to artificial ageing. A convection oven was used for the solutionising, where the profiles were heated to 540 °C for 15 min and subsequently water quenched. After 20 min, the samples were artificially aged in an oil bath at 185 °C for 5 h.

## 3.2 Material characterisation

LM imaging was used to characterise the microstructure of all profiles in the T5 and T6 temper. The technique was also used to estimate the depth of the recrystallised layer for relevant samples. Samples were taken from profiles in the T5 and T6 temper and cut into dimension as indicated in Figure 3.1a with a Discotom 2.

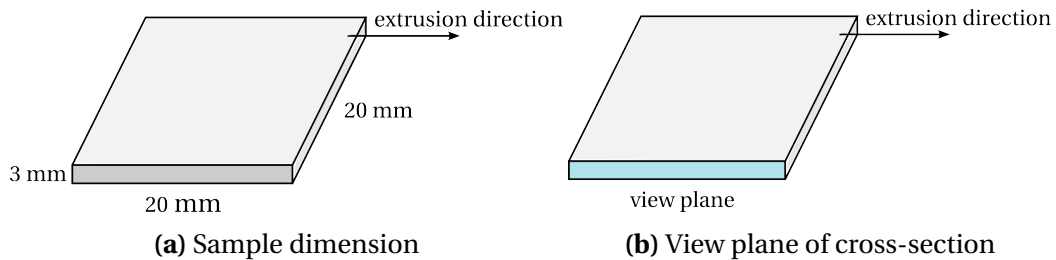


**Figure 3.1:** Sample dimensions and view plane for material characterisation.

### 3.2.1 Sample preparation and examination in LM

Samples were mounted in EpoFix resin, set by vacuum impregnation and ground with gradually finer SiC abrasive papers (500P, 800P, 1000P, 1200P, 2400P) with water as lubricant until a uniform surface was obtained. Prior to polishing, the samples were rinsed in soap water and ethanol and dried. Polishing was carried out with polishing discs and diamond paste; 3  $\mu\text{m}$  MD Mol, 1  $\mu\text{m}$  MD Nap and 1  $\mu\text{m}$  OP-S suspension, for 2-5 min each until surface defects were absent. Samples were rinsed in soap water, ethanol and dried between each polishing step. To image the grain structure with polarised light in LM, the surface to be examined was anodised. Samples were immersed in 5%  $\text{HBF}_4$  solution with an applied voltage of 20.00 V and current of 1 A for 90-180 s, and immediately submerged in water, cleaned with water and finally air-dried.

A Leica MeF4 optical microscope was used for microstructure examination, and the images obtained with Jentik Optic System camera and ProgRes Capture v2.8.8. The images of the anodised surface were taken perpendicular to the extrusion direction as indicated in Figure 3.1b, and the grain structure imaged with polarised light and a sub-parallel  $\lambda$ -plate.

### 3.2.2 Sample preparation and TEM imaging and analysis

TEM imaging and EDS analysis was performed on a T5 tempered profile with 0.31 wt% Cu and 0.60 wt% Zn, and the images were taken in STEM mode. Thin foils of the sample was mechanically polished and punched into 3 mm discs and polished to electron transparency afterwards. Electropolishing electrolyte was one volume part concentrated nitric acid ( $\text{HNO}_3$ ) and two parts methanol ( $\text{CH}_3\text{OH}$ ) while the temperature was maintained between -37 and -32  $^\circ\text{C}$  by cooling with liquid nitrogen. Furthermore, samples were ion beam thinned prior to examination. The samples were prepared in transverse geometry, i.e. the captured images visualise grain boundaries down the extrusion direction. The examination was carried out using a JEOL 2100F TEM and operated in STEM mode at 200 kV with a nominal electron probe diameter of 1 nm, and the grain boundary composition was analysed with EDS using an Oxford Instrument system. The sample preparation and TEM images were performed and acquired by John C. Walmsley from SINTEF Materials and Chemistry.

### 3.3 Hardness measurements

Vickers hardness measurements were performed on all profiles in the T5 and T6 tempers. The test surface was ground using SiC abrasive papers with increasing fineness to 1000P, and the sample was clamped to align the specimen surface with the indenter. Ten indentations were made parallel to the extrusion direction with 1-2 mm spacing between each indent, as indicated in Figure 3.2. The measurements were carried out with 1 kg load for 15 s per cycle using a Matsuzawa DKV-1S hardness tester.

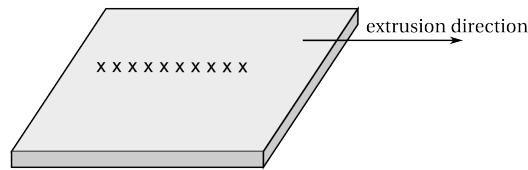


**Figure 3.2:** Vickers hardness measurements were carried out with ten indentations parallel to the extrusion direction.

### 3.4 Accelerated IGC test

Standardised accelerated corrosion testing according to BS-ISO 11846 (method B) was done on four parallels with variations in test execution to study whether any differences occurred in the obtained results. All alloy compositions in the T5 and T6 condition were tested in each parallel. Nonetheless, all parallels were prepared according to the procedure described in the following section. The BS-ISO 11846 is applicable to cast and wrought heat treatable aluminium alloys without protective coatings, and method B provides a testing method for comparing intergranular corrosion resistance relatively among alloys as a function of varying alloy composition and heat treatment.

#### 3.4.1 Sample preparation and IGC test execution

The surface of the test specimens were degreased with acetone and then alkaline etched. The alkaline etch was carried out by initially immersing the specimen in a 7.5 wt% sodium hydroxide (NaOH) solution at 50-60 °C for 3 min, and desmutted afterwards by immersion in 64% HNO<sub>3</sub> for 2 min. The specimen was rinsed in running water before desmutting and finally rinsed in running water and distilled water. All samples were weighed after the alkaline etch.

The test specimen were then mounted freely in the glass beaker with fishing line to avoid concentration gradients and immersed in an acidified test solution (pH ~ 1) consisting of 30 g/l sodium

chloride (NaCl) and 10 ml/l of 35% hydrochloric acid (HCl) for 24 h. The ratio of the electrolyte volume to the total exposed specimen area exceeded  $5 \text{ cm}^3$  per  $\text{cm}^2$ , and the test solution was at least 20 mm above the upper edge of the specimen. All test dimensions were between 4 and  $20 \text{ cm}^2$  as specified in the standard. Finally, the samples were immersed in 75%  $\text{HNO}_3$  for 2 min to remove corrosion products, rinsed thoroughly in water and air-dried. Samples were weighed before and after the accelerated corrosion test to document the total weight loss during testing. Only deionised water and analytical grade chemicals were used throughout testing.

### Variation in test execution

As stated, four parallels of IGC testing was conducted. Specific variations were made to the samples, well within the requirements of the procedures provided by the standard. A run-through of variations in test execution are listed in Table 3.2, and include size variation, exposure of edges and surface microstructure. All edges of the specimens were ground with SiC abrasive papers to 1000P in order to ensure the surface roughness to be  $R_a \leq 2.5 \mu\text{m}$ , except from the edge covered specimens. A set of T5 samples were ground to the fibre structure to remove the recrystallised layer on one side to examine if the fibrous texture was susceptible to IGC. Another set had a larger sample dimension in order to reduce the edge/surface ratio. The IGC testing of these parallels were conducted in the same manner as described in the previous paragraphs.

The edge covered specimens were coated with beeswax to observe how edge corrosion affected the development of IGC on the recrystallised surface. After alkaline etching the samples were weighed. Masking tape with dimensions  $2.2 \times 2.2 \text{ cm}$  was fastened onto each side of the specimen surfaces and submerged into heated beeswax. Several rounds of immersion in beeswax was done to cover the entire sample. After the beeswax had dried, the tape was removed with a scalpel to reveal a specific exposure area while the edges remained covered. After the 24 h IGC test was completed, the beeswax was removed by dipping the samples in boiling water. Finally, corrosion products were removed by immersion in nitric acid and the samples were rinsed, dried and weighed. An overview of all sample dimensions for the accelerated IGC test is shown in Figure 3.3.

**Table 3.2:** Variations in parameters of the different IGC test parallels.

| Parallel | Specimen area [ $\text{cm}^2$ ] | Edge surface area [%] | Variable                  |
|----------|---------------------------------|-----------------------|---------------------------|
| 1        | 10                              | 37-39                 | -                         |
| 2        | 10                              | -                     | covered edges             |
| 3        | 20                              | 28                    | larger specimen area      |
| 4        | 10                              | -                     | ground to fibre structure |

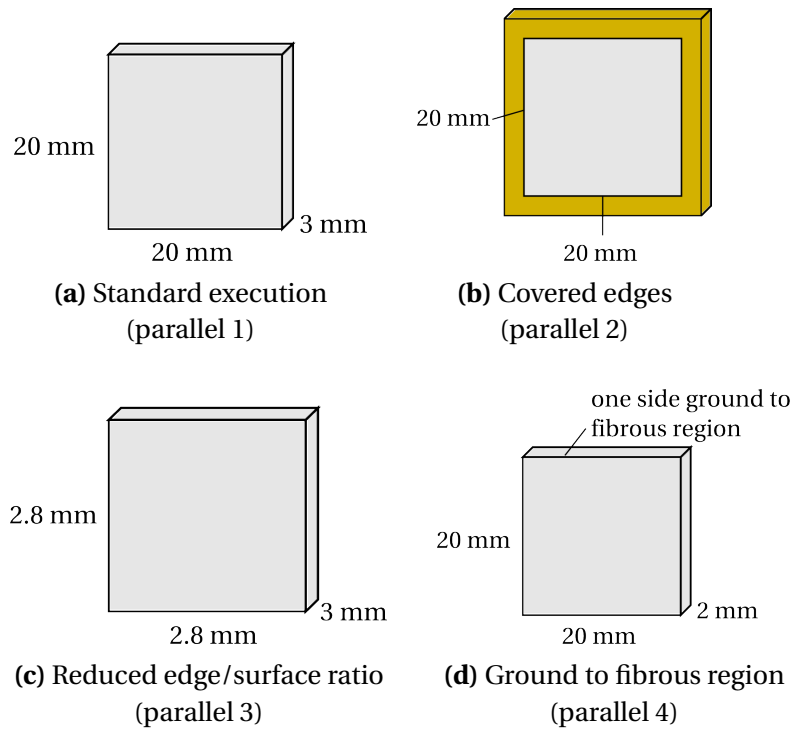


**Figure 3.3:** Sample dimensions for the four IGC parallels.

### 3.5 Examination in LM and SEM after IGC test

All specimens from the accelerated IGC test were examined in SEM and optical microscope after corrosion testing. The sample surfaces were initially examined in SEM and images acquired in second electron mode (SE) with a working distance of approximately 10-15 mm, accelerating voltage of 10.00 kV and aperture of 30.00  $\mu\text{m}$ . The electron micrographs were taken with a Zeiss Supra 55 VP LVFESEM. Subsequent to SEM imaging, examination of the corroded surface was done in LM to mark the most severe corrosion attacks for all tested samples. Cross-sections were then cut at these sites, parallel to the extrusion direction using an Accutom-5 and afterwards mounted in EpoFix resin. The surface of interest, as indicated in Figure 3.1b, was prepared in the same manner as detailed in section 3.2.1, with the exception of the anodising step. All optical micrographs were imaged in bright field with the same apparatus stated in section 3.2.1.

### 3.6 Open circuit potential measurements

OCP measurements were conducted separately on edge and surface to examine the corrosion potential differences between the areas, in addition to document the effect of alloying with Zn. T5

tempered profiles with 0.30 wt% Cu, 0.00 wt% Zn and 0.31 wt% Cu, 0.60 wt% Zn, respectively, were selected for this purpose. Two sample specimens were collected from each alloy composition and alkaline etched as described in section 3.4.1. Masking tape was attached to a single edge of one sample, and on one surface of the other. Both samples were then fastened with copper wire and immersed in hot beeswax until the entire specimen was fully covered. The copper wire was thoroughly isolated with beeswax to ensure that the wire would not come in contact with the test solution. After the beeswax had dried off, the area of the masking tape was removed with a scalpel in order to expose either the edge or the surface. The areas of exposure were cleaned with acetone and rinsed in distilled water before the OCP measurements were performed.

A saturated calomel electrode (SCE) immersed in a saturated potassium chloride (KCl) solution was used as a reference electrode during the measurements. All potentials stated throughout this report are given in reference to the SCE reference electrode, which is approximately +0.244 mV with respect to the standard hydrogen electrode (SHE) [53]. The test solution was identical to the one described in section 3.4.1. Electrical contact between the reference electrode and the test solution was established by a tube filled with the electrolyte. The OCP was measured simultaneously for the two samples with identical alloy composition, i.e. the edge sample and surface sample of same composition was mounted into the same beaker and connected to separate Gamry potentiostats. The reference electrode was then connected to both potentiostats, and the electrolyte filled until the surfaces of interest were covered, but beneath the exposed copper wire. The OCP was measured continuously for 24 h with a frequency of one measurement per minute.

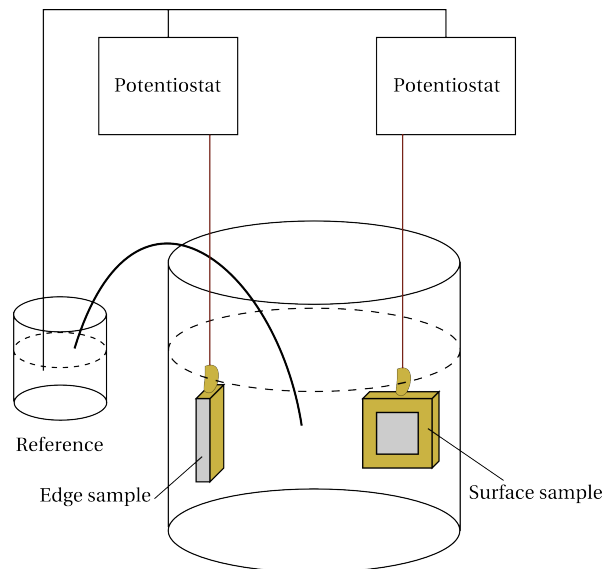


**Figure 3.4:** A schematic illustration of the test set-up for the OCP measurements of surface and edge. Samples measured simultaneously in the same beaker were of the same alloy composition.





## Chapter 4

# Results

### 4.1 Microstructure

The microstructure of all alloy compositions and tempers were characterised in LM to compare recrystallisation and texture variations dependent on alloy content and heat treatment. Optical micrographs of the T5 tempered alloys are presented in Figure 4.1, and the T6 tempered profiles are shown in Figure 4.2. Images were acquired with a magnification of 2.5x.

No significant change in microstructure due to alloy content can be observed within each temper, though a substantial difference in microstructure is seen for the two different heat treatments. In the T5 temper, the profiles have been artificially aged to peak hardness from the as-extruded condition and subsequently water quenched. Most of the fibrous structure caused by deformation during extrusion has been maintained, and recrystallisation has only occurred on the surface. The measured average depth of recrystallisation show no significant variations with alloy content, and ranges from 441-492  $\mu\text{m}$ , as presented in Table 4.1. The T6 temper includes solution heat treatment from the as-extruded condition before artificial ageing. This treatment causes complete recrystallisation of the fibrous region and larger elongated grains can be seen in the bulk, whereas the recrystallised region near the surface consists of smaller grains.

**Table 4.1:** Average depth of recrystallised layer for different alloy compositions in T5 profiles.

| Cu [wt%] | Zn [wt%] | Avg. depth of<br>recrystallised layer [ $\mu\text{m}$ ] |
|----------|----------|---|
| 0.00     | 0.00     | 465   |
| 0.30     | 0.00     | 466   |
| 0.31     | 0.21     | 441   |
| 0.31     | 0.60     | 492   |

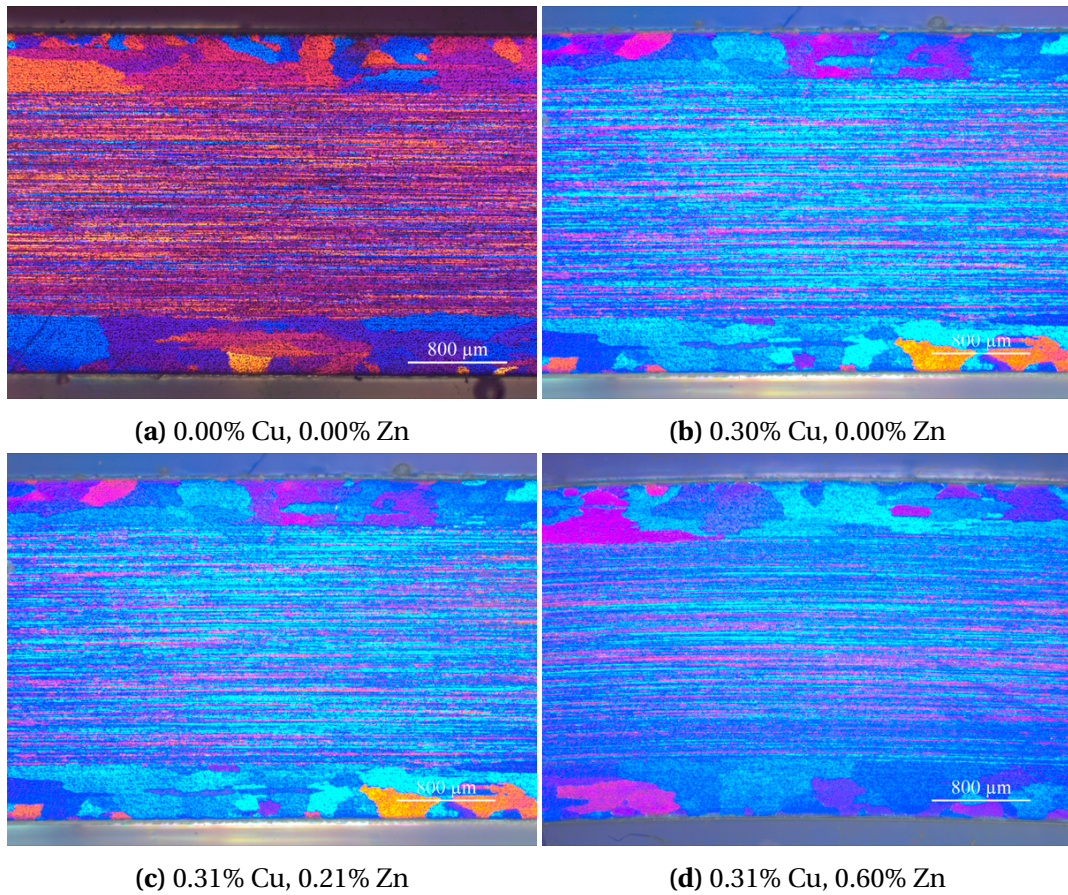


**Figure 4.1:** Optical micrographs (2.5x) of cross-sections showing the microstructure in T5 tempered alloys, viewed perpendicular to the extrusion direction. Alloy content is given in wt%.

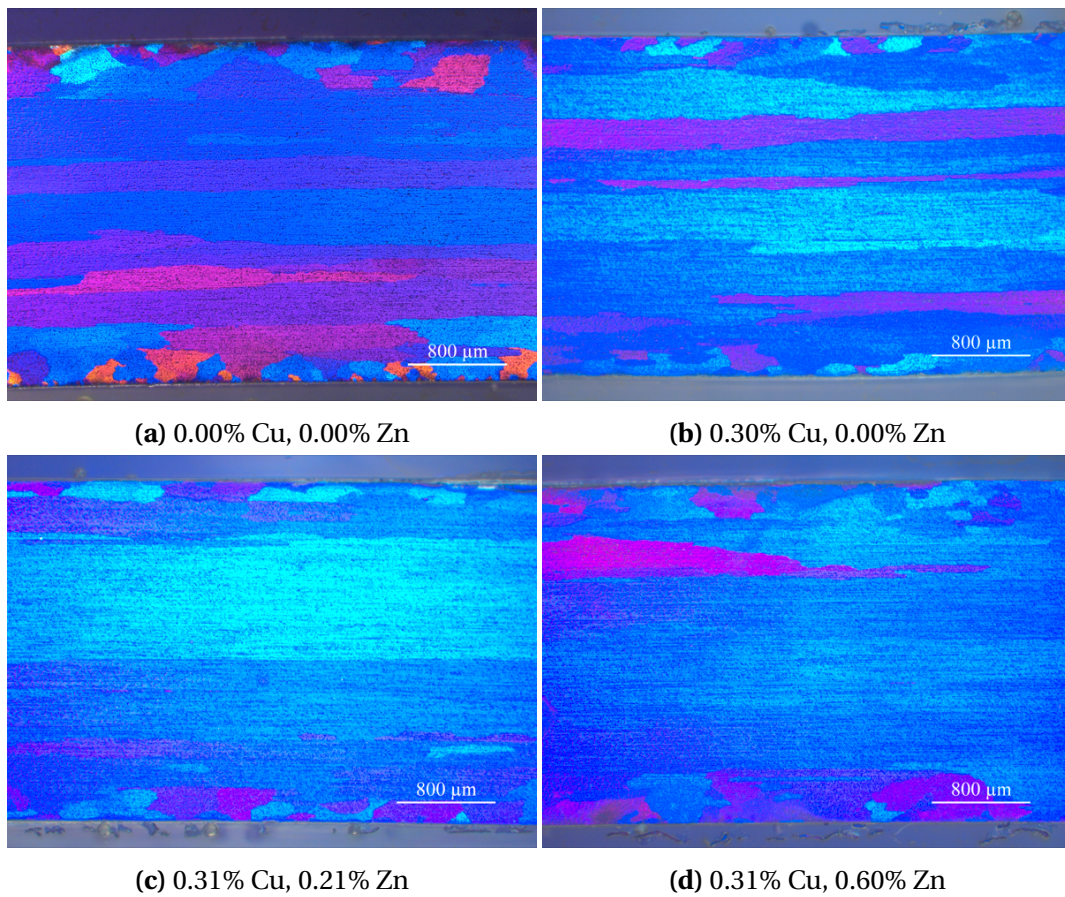


**Figure 4.2:** Optical micrographs (2.5x) of cross-sections showing the microstructure in T6 tempered alloys, viewed perpendicular to the extrusion direction. Alloy content is given in wt%.

## 4.2 Effect of microstructure and Zn on hardness

Results for the Vickers hardness measurements on all 6082 profiles in the T5 and T6 temper are graphically presented in Figure 4.3. Average hardness measurements for the T5 tempered profiles are found in Table B.1 and average values for the T6 temper is found in Table B.2 in Appendix B.

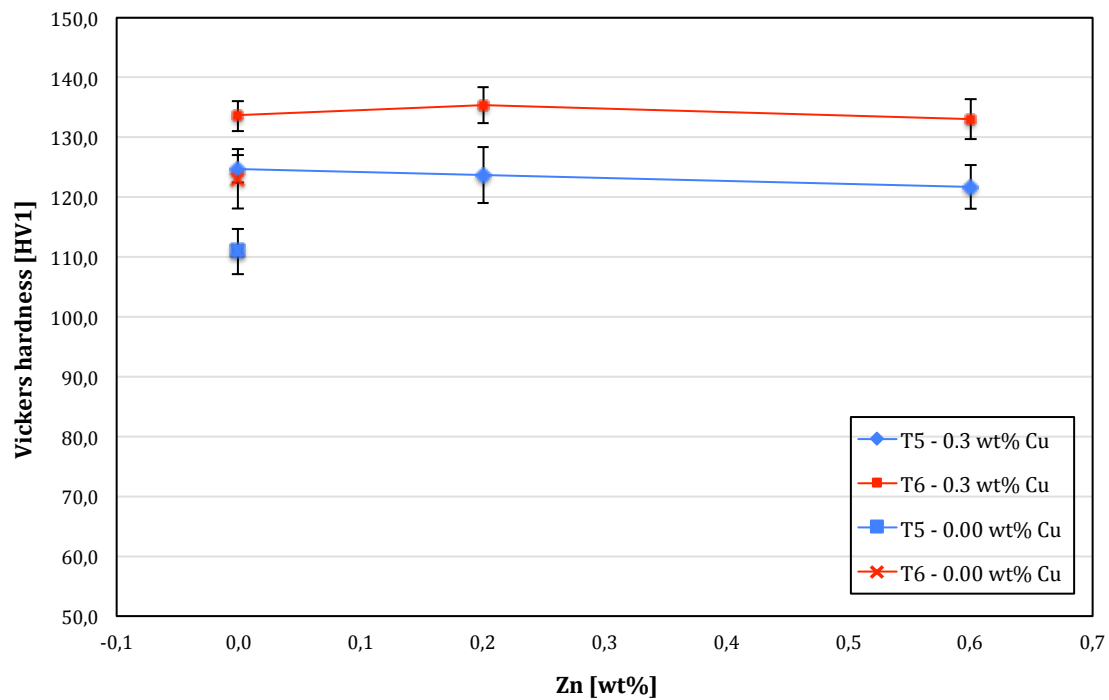


**Figure 4.3:** Vickers hardness measurements (HV1) for alloys containing 0.00 wt% Cu and 0.30 wt% Cu and increasing Zn content in the T5 and T6 temper.

Hardness values for the 0.00 wt% Cu, 0.00 wt% Zn profiles in both T5 and T6 temper compared with the Cu containing alloys show that the addition of Cu has the largest influence when it comes to increasing hardness. An additional ~15 HV is added when the profile is alloyed with 0.30 wt% Cu, this is apparent for profiles in both tempers. The addition of Zn however does not point the hardness to either direction. From the attained results, Zn does not seem to influence the hardness of these alloys, and the hardness remains fairly constant with varying Zn content. Solution heat treating before ageing to peak hardness, i.e. the T6 temper, provides a slight increase in hardness, although the standard deviation values indicated in the chart show that this modest increase is near the margin of error.

### 4.3 Accelerated IGC tests

A series of accelerated corrosion tests were performed according to BS-ISO 11846, a 24 h submer-sion test in an acidic corrosive electrolyte designed to determine intergranular corrosion resistance of aluminium alloys [78]. Subsequent to corrosion testing, weight loss was measured and the test specimens were prepared for quantitative assessment of corrosion damages in SEM and LM. The subject of examination was two-folded; to investigate how alloy composition and different heat treatments affect IGC resistance, and to evaluate the reliability of the test procedure described by BS-ISO 11846 to detect IGC susceptibility. Specific variations were made to the samples, well within the requirements of the procedures provided by the standard, to examine if any changes in the results occurred as already detailed in section 3.4.1. An overview of the parallels are listen in Table 3.2.

Interpretation of the results from the metallographic examination are summarised in a table for each tested alloy. An attempt to classify susceptibility to IGC of each alloy has been made by di-viding into roughly three categories; none, local IGC and uniform IGC. Where only a few shallow and highly localised IGC attacks have been observed, the alloy has been classified as resistant to IGC, i.e. labeled «none», since the test solution is very aggressive. It should be emphasised that the following optical micrographs represent a specific cross-section of the specimen selected from the most severe corrosion damage observed. Corrosion depth measurements were conducted in LM.

### 4.3.1 Effect of microstructure and alloy content on IGC

The IGC test of this parallel was conducted in an ordinary manner according to the standard (parallel 1) to examine how the IGC susceptibility varies with increasing Zn content and microstructure. Results strongly indicate that increased Zn content reduces IGC resistance for the 6082-profiles both in the T5 and T6 temper.

#### T5: artificially aged at 185 °C (5 h)

Figure 4.4 presents optical micrographs of the T5 tempered profiles with a magnification of 2.5x and 20x. All profiles seem to be practically resistant to IGC except when 0.60 wt% Zn is introduced. No IGC except for a few shallow attacks are observed on the 0.00 Cu wt% and 0.00 Zn wt% imaged in Figure 4.4a-4.4c, and the same can be seen in the 0.31 Cu wt% and 0.21 wt% Zn profile in Figure 4.4g-4.4i. The Zn free alloy with 0.30 wt% Cu in Figure 4.4d-4.4f however show no signs of IGC. Shallow, though uniform IGC is evident for the profile containing maximum Cu and Zn levels, seen in Figure 4.4j-4.4l.

Corrosion depth and weight loss are found in Table 4.2. Weight loss values for the two seemingly IGC resistant alloys containing 0.30 wt% Cu and 0.00 wt% Zn, and 0.31 wt% Cu and 0.21 wt% Zn, points towards that extensive corrosion has occurred, and the crucial observation here is that the weight loss originates from the corrosion of edges, as seen in Figure 4.4d and 4.8g. Weight loss increases significantly when the Zn level reaches 0.60 wt% .

**Table 4.2:** Measured corrosion depths and weight loss for the T5 tempered specimens in parallel 1 after IGC testing.

| Cu [wt%] | Zn [wt%] | Corrosion mode | Avg. corrosion depth [ $\mu\text{m}$ ] | Max. corrosion depth [ $\mu\text{m}$ ] | Weight loss [ $\text{mg}/\text{cm}^2$ ] |
|----------|----------|----------------|--|--|---|
| 0.00     | 0.00     | none           | -                                      | -                                      | 0.70                                    |
| 0.30     | 0.00     | none           | -                                      | -                                      | 4.52                                    |
| 0.31     | 0.21     | none           | -                                      | -                                      | 4.51                                    |
| 0.31     | 0.60     | uniform IGC    | 71                                     | 95.6                                   | 5.98                                    |



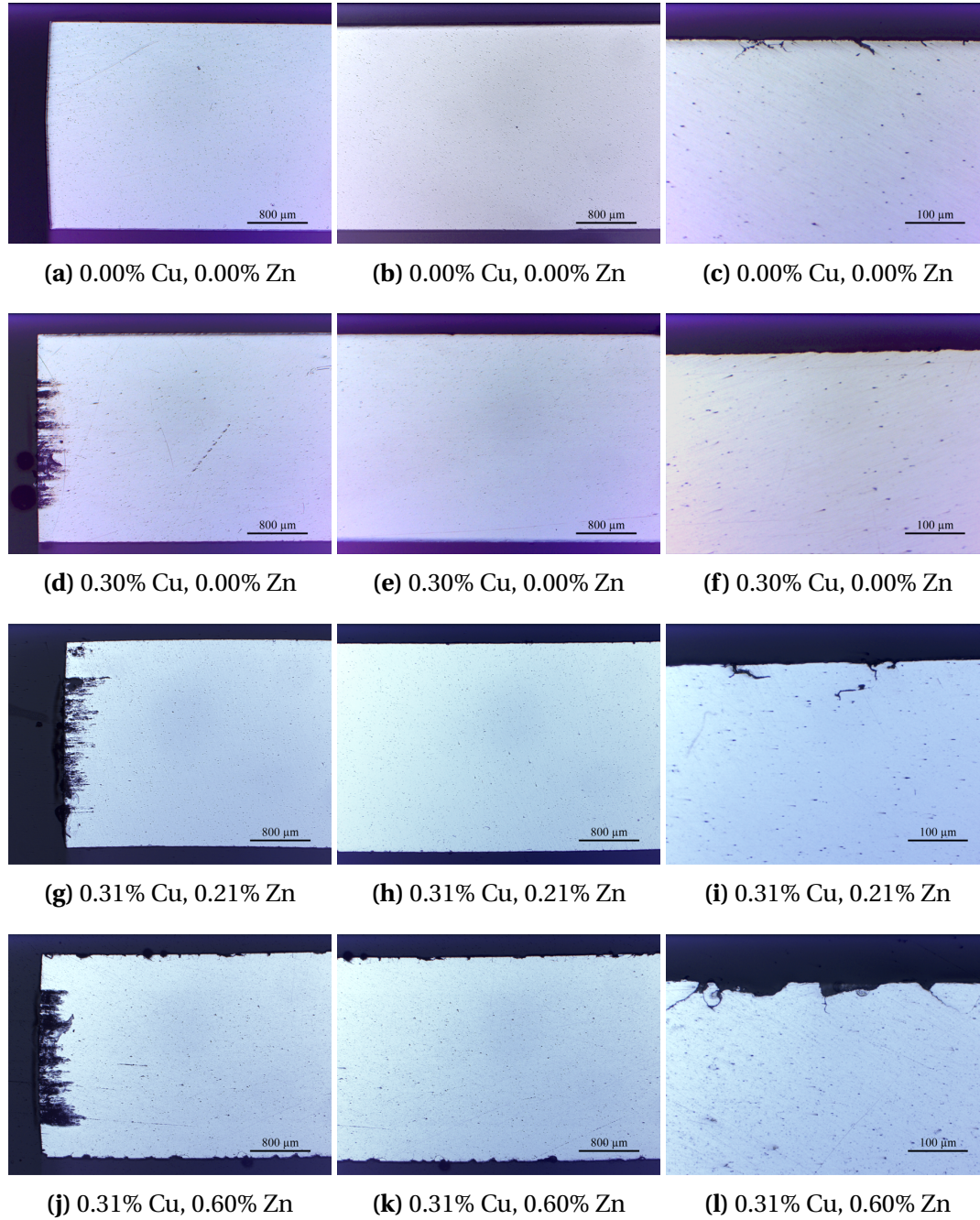


**Figure 4.4:** Optical micrographs (2.5x, 20x) of cross-sections showing extent of corrosion damages with varying Cu and Zn content for the T5 temper. Specimens are from test parallel 1. Alloy content is given in wt%.

**T6: solutionised at 540 °C (15 min) and artificially aged at 185 °C (5 h)**

Optical micrographs of the T6 tempered alloys are shown in Figure 4.5. The Cu and Zn free profile suffered from local and narrow IGC attacks seen in Figure 4.5a-4.5c. The Cu containing alloys suffered from deep uniform IGC, and grew more severe as the Zn level increased. A comparison of Figure 4.5e with Figure 4.5h and 4.5k illustrates this. Values for corrosion depth and weight loss are listed in Table 4.3. Weight loss values increase when Cu is added, and is further intensified as the Zn level reaches 0.60 wt%. Moderate corrosion can be observed on the edges for the Cu containing alloys, as seen in Figure 4.5d, 4.5g and 4.5j. Weight loss is nearly identical for the 0.30 wt% Cu, 0.00 wt% Zn and 0.31 wt% Cu, 0.21 wt% Zn, although the corrosion depth of the latter was deeper.

**Table 4.3:** Measured corrosion depths and weight loss for the T6 tempered specimens after IGC testing.

| <b>Cu [wt%]</b> | <b>Zn [wt%]</b> | <b>Corrosion mode</b> | <b>Avg. corrosion depth [<math>\mu\text{m}</math>]</b> | <b>Max. corrosion depth [<math>\mu\text{m}</math>]</b> | <b>Weight loss [<math>\text{mg}/\text{cm}^2</math>]</b> |
|-----------------|-----------------|-----------------------|--|--|---|
| 0.00            | 0.00            | local IGC             | 146  | 301  | 1.42  |
| 0.30            | 0.00            | uniform IGC           | 227  | 295  | 3.13  |
| 0.31            | 0.21            | uniform IGC           | 283  | 351  | 3.08  |
| 0.31            | 0.60            | uniform IGC           | 389  | 473  | 5.85  |



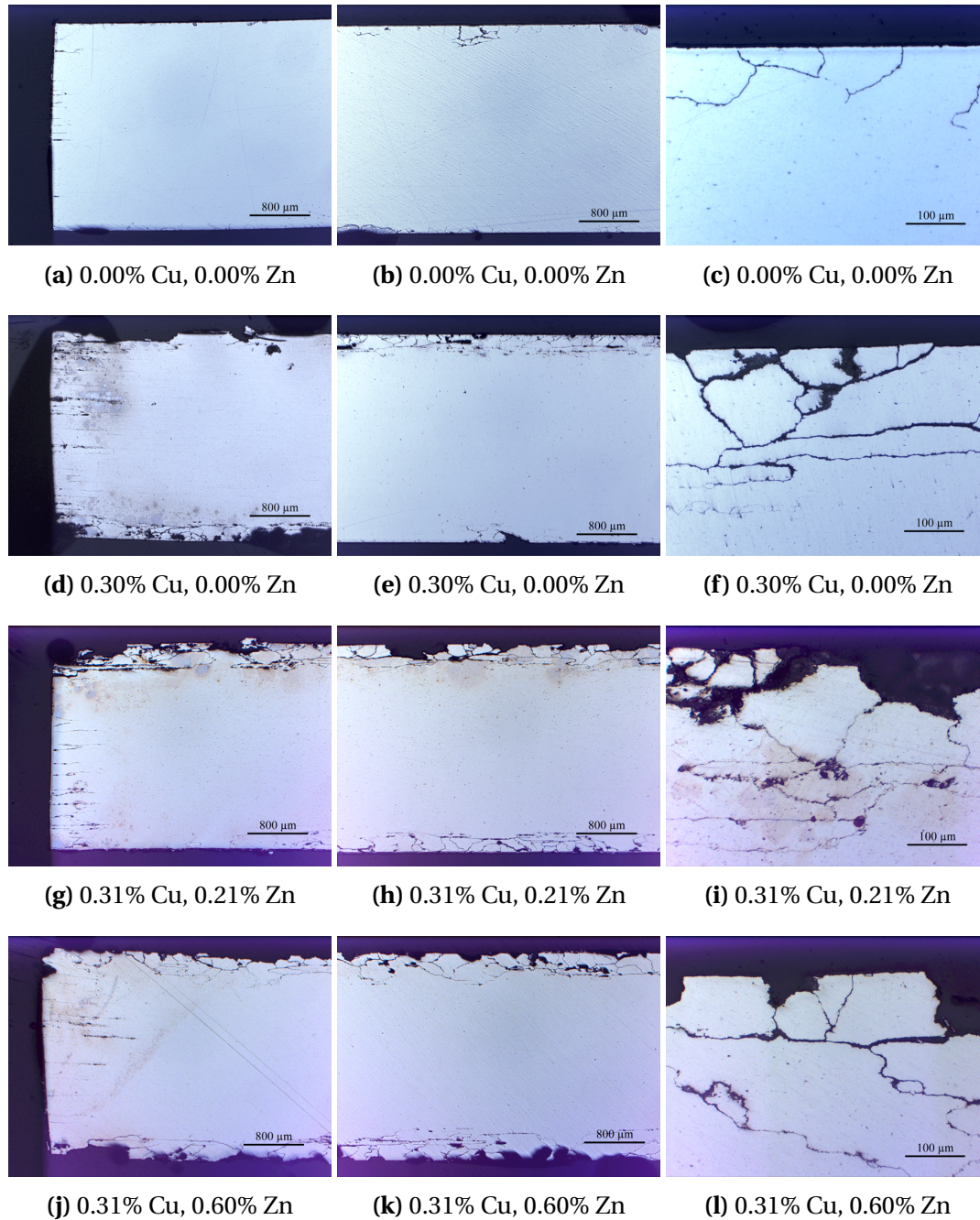


**Figure 4.5:** Optical micrographs (2.5x, 20X) of cross-sections showing extent of corrosion damages with varying Cu and Zn content for the T6 temper. Specimens are from parallel 1. Alloy content is given in wt%.

### 4.3.2 IGC on edge covered specimens

An accelerated IGC test was conducted on samples where the edges were covered with beeswax in order for the edges to avoid contact with the corrosive test solution (parallel 2). This test was performed to examine whether if the extent of edge corrosion was severe enough to conceal any evidence of IGC susceptibility on the profiles. Weight loss measurements were also done after corrosion testing, although these values are highly inaccurate as the removal of beeswax is very troublesome. The values can however be evaluated relatively to one another.

#### T5: artificially aged at 185 °C (5 h)

Figure 4.6 shows optical micrographs (2.5x and 20x) of profiles in the T5 temper. All alloys suffer from severe IGC attacks, except from the Cu and Zn free alloy which shows no signs of corrosion. Uniform and deep IGC attacks are present when 0.30 wt% Cu is introduced, seen in Figure 4.6c and 4.6d. The IGC attacks become narrower and penetrate deeper as the Zn level is raised to 0.60 wt% , as seen in Figure 4.6g and the corrosion depth values in Table 4.4. Weight loss values is exceedingly increased when the Zn level reaches 0.60 wt%.

**Table 4.4:** Measured corrosion depths and weight loss for the T5 tempered specimens after IGC testing.

| Cu [wt%] | Zn [wt%] | Corrosion mode | Avg. corrosion depth [ $\mu\text{m}$ ] | Max. corrosion depth [ $\mu\text{m}$ ] | Weight loss [ $\text{mg}/\text{cm}^2$ ] |
|----------|----------|----------------|--|--|---|
| 0.00     | 0.00     | none           | -                                      | -                                      | -                                       |
| 0.30     | 0.00     | uniform IGC    | 277                                    | 345                                    | 3.68                                    |
| 0.31     | 0.21     | uniform IGC    | 215                                    | 347                                    | 5.32                                    |
| 0.31     | 0.60     | uniform IGC    | 441                                    | 511                                    | 10.9                                    |

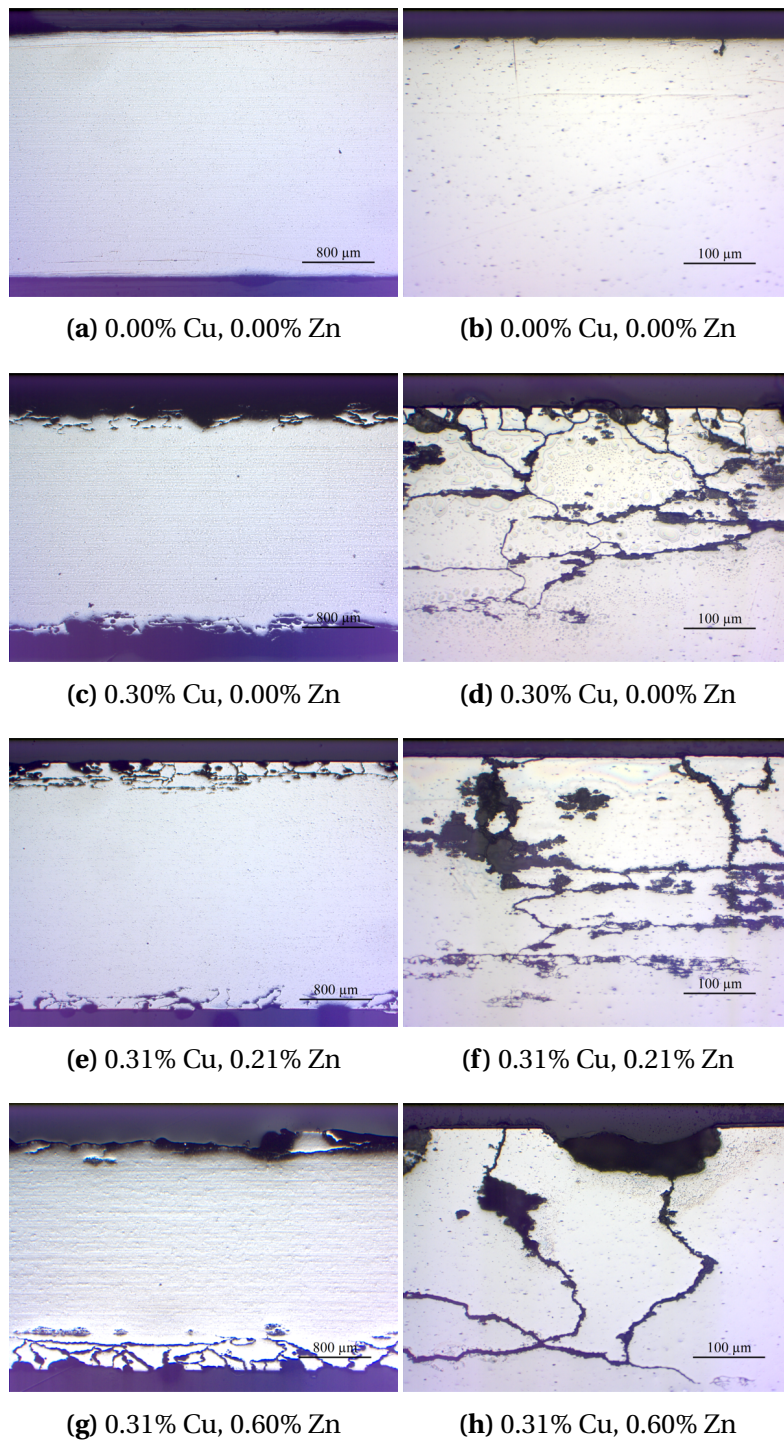


**Figure 4.6:** Optical micrographs (2.5x, 20x) of cross-sections showing extent of corrosion damages of edge covered specimen with varying Cu and Zn content in the T5 temper (parallel 2). Alloy content is given in wt%.

**T6: solutionised at 540 °C (15 min) and artificially aged at 185 °C (5 h)**

Optical micrographs (2.5x and 20x) of the edge covered specimens in the T6 condition are shown in Figure 4.7. All alloys have suffered IGC to varying extent, except from the Cu and Zn free sample which have experienced only a few shallow IGC pits. The remaining alloys are all susceptible to IGC, showing increased corrosion depth as Zn is introduced and further raised, indicated by average and maximum depth values in Table 4.5. Mass loss values are however not significantly increased until 0.60 wt% Zn is added.

**Table 4.5:** Measured corrosion depths and weight loss for the T6 tempered specimens after IGC testing.

| Cu [wt%] | Zn [wt%] | Corrosion mode     | Avg. corrosion depth [ $\mu\text{m}$ ] | Max. corrosion depth [ $\mu\text{m}$ ] | Weight loss [ $\text{mg}/\text{cm}^2$ ] |
|----------|----------|--------------------|--|--|---|
| 0.00     | 0.00     | local, shallow IGC | 55.4                                   | 85.8                                   | 0.02                                    |
| 0.30     | 0.00     | uniform IGC        | 146                                    | 202                                    | 2.83                                    |
| 0.31     | 0.21     | uniform IGC        | 320                                    | 409                                    | 2.40                                    |
| 0.31     | 0.60     | uniform IGC        | 432                                    | 489                                    | 7.06                                    |



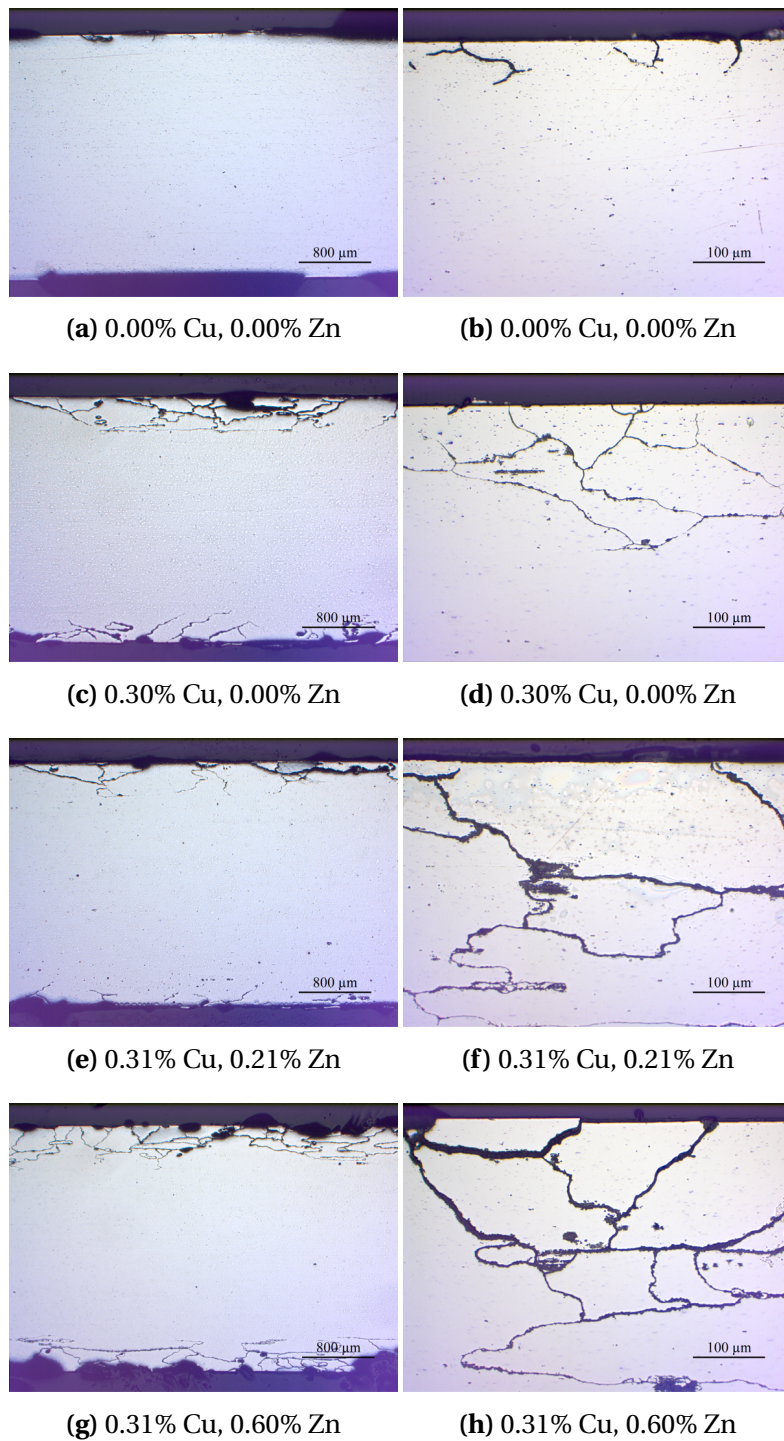


**Figure 4.7:** Optical micrographs (2.5x, 20x) of cross-sections showing extent of corrosion damages of edge covered specimen with varying Cu and Zn content in the T6 temper (parallel 2). Alloy content is given in wt%.

### 4.3.3 Effect of surface to edge ratio

In order to evaluate if the ratio between the surfaces transverse to the extrusion direction and the cut edges, perpendicular to the extrusion direction, had any effect on detecting IGC susceptibility, samples with a larger surface area were prepared and IGC tested accordingly to BS-ISO 11846 (parallel 3). The dimensions in this parallel had a specimen surface area of 20 cm<sup>2</sup> and an edge area of 28% compared to 10 cm<sup>2</sup> and 37-39% for the parallel presented in section 4.3.1.

#### T5: artificially aged at 185 °C (5 h)

Figure 4.8 show results after IGC testing of the larger samples in the T5 temper. The Zn free profiles show no susceptibility to IGC, whereas IGC is introduced when Zn is added. Only localised IGC is observed when the Zn level is at 0.21 wt% , though the corrosion mode becomes uniform when 0.60 wt% Zn is reached. Corrosion depth and weight loss values are found in Table 4.6.

**Table 4.6:** Measured corrosion depths and weight loss for the T5 tempered specimens after IGC testing.

| Cu [wt%] | Zn [wt%] | Corrosion mode     | Avg. corrosion depth [μm] | Max. corrosion depth [μm] | Weight loss [mg/cm <sup>2</sup> ] |
|----------|----------|--------------------|---------------------------|---------------------------|-----------------------------------|
| 0.00     | 0.00     | none               | -                         | -                         | 0,61                              |
| 0.30     | 0.00     | none               | -                         | -                         | 4.87                              |
| 0.31     | 0.21     | local, shallow IGC | 192                       | 312                       | 5.69                              |
| 0.31     | 0.60     | uniform IGC        | 286                       | 471                       | 8.56                              |

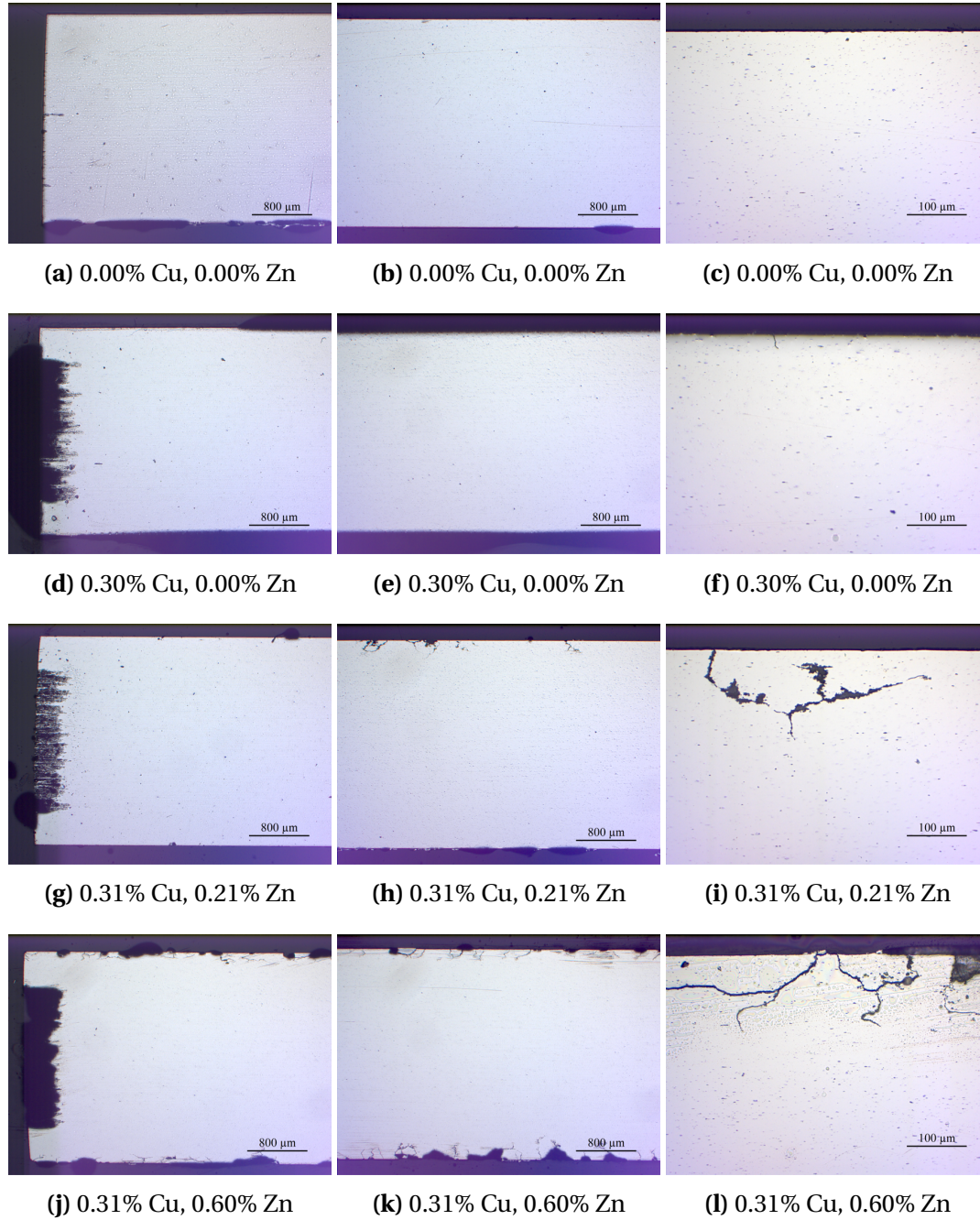


**Figure 4.8:** Optical micrographs (2.5x, 20x) of cross-sections showing extent of corrosion damages with varying Cu and Zn content for the T5 temper (parallel 3). Alloy content is given in wt%.

**T6: solutionised at 540 °C (15 min) and artificially aged at 185 °C (5 h)**

Optical micrographs (2.5x and 20x) of the T6 tempered profiles are presented in Figure 4.9. All variations of alloy composition have experienced IGC to a varying degree, ranging from local attacks to uniform and deep IGC attacks. IGC becomes uniform when Cu is added to the alloy and becomes deeper when alloyed with 0.21 wt% Zn, although no significant weight loss change is detected, according to Table 4.7. When the Zn content reaches 0.60 wt% , the depth and extent of the IGC attacks increases dramatically as seen Figure 4.9k and supported by weight loss and corrosion depth values in Table 4.7.

**Table 4.7:** Measured corrosion depths and weight loss for the T6 tempered specimens after IGC testing.

| <b>Cu [wt%]</b> | <b>Zn [wt%]</b> | <b>Corrosion mode</b> | <b>Avg. corrosion depth [μm]</b> | <b>Max. corrosion depth [μm]</b> | <b>Weight loss [mg/cm<sup>2</sup>]</b> |
|-----------------|-----------------|-----------------------|----------------------------------|----------------------------------|--|
| 0.00            | 0.00            | local IGC             | 146                              | 301                              | 1.17                                   |
| 0.30            | 0.00            | uniform IGC           | 227                              | 295                              | 3.29                                   |
| 0.31            | 0.21            | uniform IGC           | 283                              | 351                              | 3.27                                   |
| 0.31            | 0.60            | uniform IGC           | 389                              | 473                              | 7.41                                   |



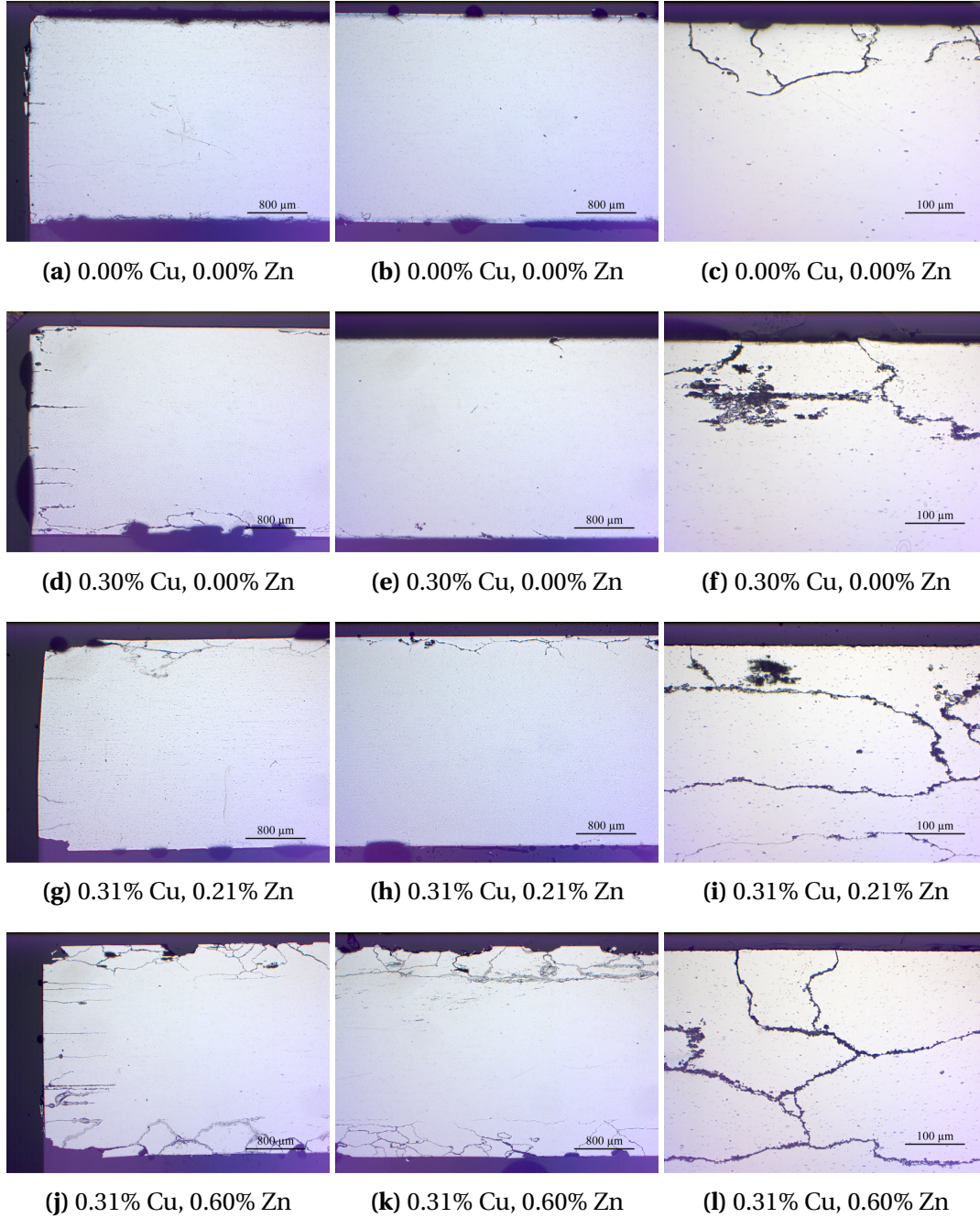


**Figure 4.9:** Optical micrographs (2.5x, 20x) of cross-sections showing extent of corrosion damages with varying Cu and Zn content for the T5 temper (parallel 3). Alloy content is given in wt%.

### 4.3.4 IGC susceptibility on fibre structure

To be able to examine whether the fibrous region in the T5 tempered alloys, as shown in Figure 4.1, was susceptible to IGC from the transverse extrusion direction (i.e not from the edges), sample surfaces were ground until the fibrous region appeared on one side (parallel 4). The samples were corrosion tested, and metallographically examined. This test procedure was only performed on the T5 profiles, as the T6 profiles did not possess a fibrous microstructure.

The optical micrographs (2.5x and 20x) of these profiles are seen in Figure 4.10. The Cu containing alloys experienced severe corrosion attacks on the fibre region of the profile, and detailed micrographs of the samples, as seen in Figure 4.10d and 4.10f strongly indicate that these corrosion attacks are intergranular. No IGC was detected on the recrystallised surface of these alloys. The fibrous region of the Cu and Zn free alloy however, show nearly no susceptibility to IGC. At maximum Zn content, the recrystallised surface has experienced some shallow IGC attacks as well, seen in Figure 4.10g. The highest weight loss value is found in this alloy, although the corrosion depth of the fibrous region seem more shallow than for the two other alloys which have suffered from IGC, seen when comparing Figure 4.10h to 4.10d and 4.10f. The reason for this might be the alloy has suffered from grain detachment due to extensive IGC. Furthermore, the IGC susceptible samples did also suffer severe edge corrosion, although no micrographs of these damages were obtained.

**Table 4.8:** Measured corrosion depths and weight loss for the T5 tempered specimens after IGC testing.

| Cu [wt%] | Zn [wt%] | Corrosion mode | Avg. corrosion depth [ $\mu\text{m}$ ] | Max. corrosion depth [ $\mu\text{m}$ ] | Weight loss [ $\text{mg}/\text{cm}^2$ ] |
|----------|----------|----------------|--|--|---|
| 0.00     | 0.00     | none           | -                                      | -                                      | 0.82                                    |
| 0.30     | 0.00     | uniform IGC    | 126                                    | 145                                    | 8.14                                    |
| 0.31     | 0.21     | uniform IGC    | 173                                    | 205                                    | 11.9                                    |
| 0.31     | 0.60     | uniform IGC    | 178                                    | 263                                    | 19.6                                    |

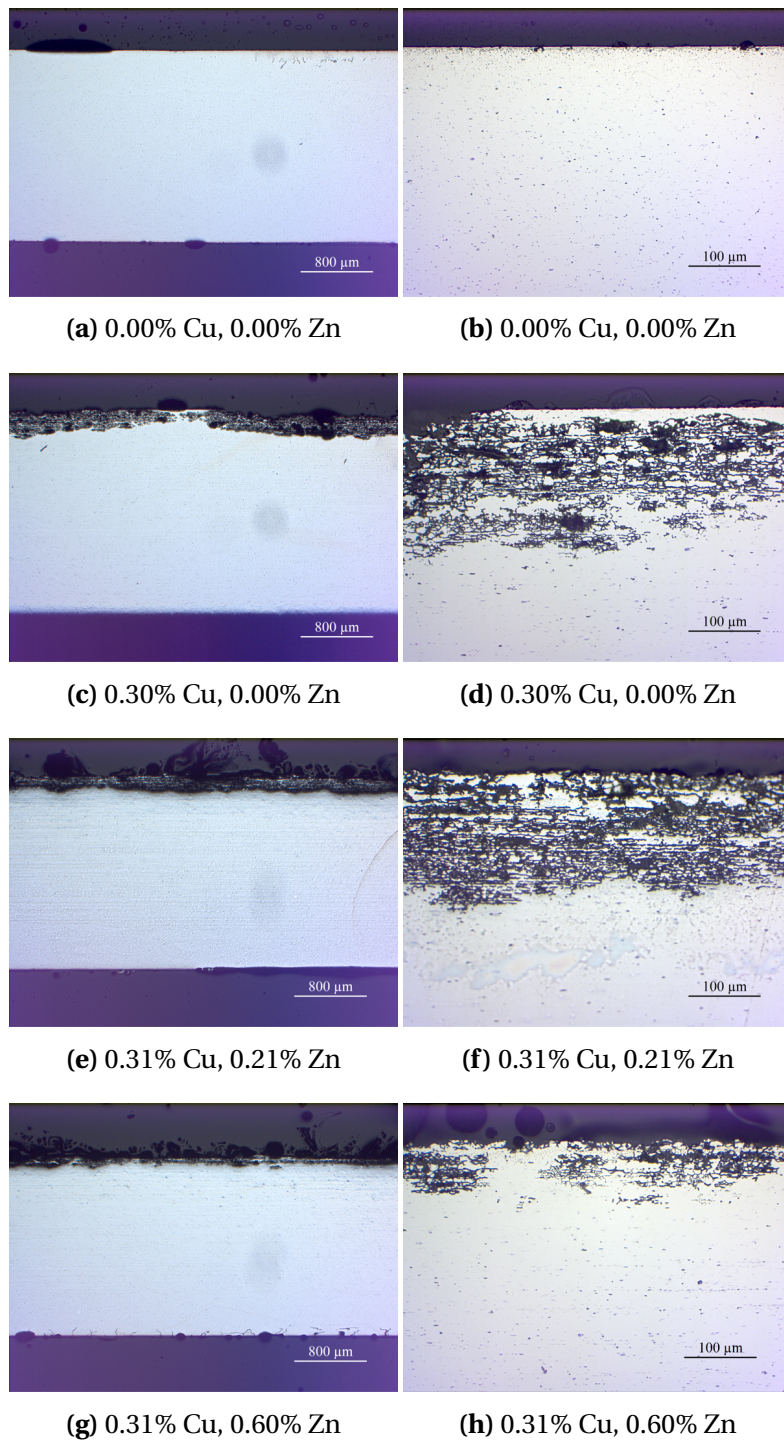


**Figure 4.10:** Optical micrographs (2.5x, 20x) of cross-sections showing extent of corrosion damages of edge covered specimen with varying Cu and Zn content in the T5 temper (parallel 4). Alloy content is given in wt%.

## 4.4 SEM imaging of surface after IGC test

The surface of all IGC tested specimen were imaged in SEM after the corrosion test. A selection of the results are presented here, while the remaining images can be found in Appendix C.

Figure 4.11 presents the SEM images of selected profiles after the standard execution of the IGC test (parallel 1). Images show the Cu containing profiles with varying Zn content in both the T5 and the T6 temper. The 0.30 wt% Cu, 0.00 wt% Zn profile in the T5 temper display shallow etching along the grain boundaries, whereas the same alloy composition in the T6 temper show apparent IGC attack resulting in grain fallout as well as uniform surface etching, seen when comparing Figure 4.11a and 4.11b. As 0.2 wt% Zn is introduced, the T5 temper shows deeper corrosion along parts of the grain boundary, seen in Figure 4.11c. In Figure 4.11d, the corrosion damage of the T6 temper resembles the one observed in Figure 4.11b, with deep corrosion attacks and indications of grain detachment. The corrosion morphology of the profiles with 0.60 wt% Zn alloy for both tempers, imaged in Figure 4.11e and 4.11f, are very similar. Larger grains have detached from the surface and the IGC attacks seems to favour propagation into the material rather than spreading along the grain boundaries on the surface, as observed in the previous images.

SEM images of all the T5 tempered profiles ground to the fibre region are presented in Figure 4.12. The Cu and Zn free alloy in Figure 4.12a seems fairly resistant to severe corrosion, as only uniform etching has occurred on the surface along with some shallow pits. The degree of corrosion is however strongly increased when Cu is present, as seen for the profiles in Figure 4.12b-4.12d. Heavy corrosion is found on all specimens along with remains of corrosion products distributed on the heavily corroded surface. Large areas of metal have also been detached from the samples. The corrosion behaviour of the 0.60 wt% Zn however seem to be more severe than the profiles with 0.00 wt% Zn and 0.21 wt% Zn, respectively. As seen in Figure 4.12d, the corrosion has penetrated deeply into the bulk material.



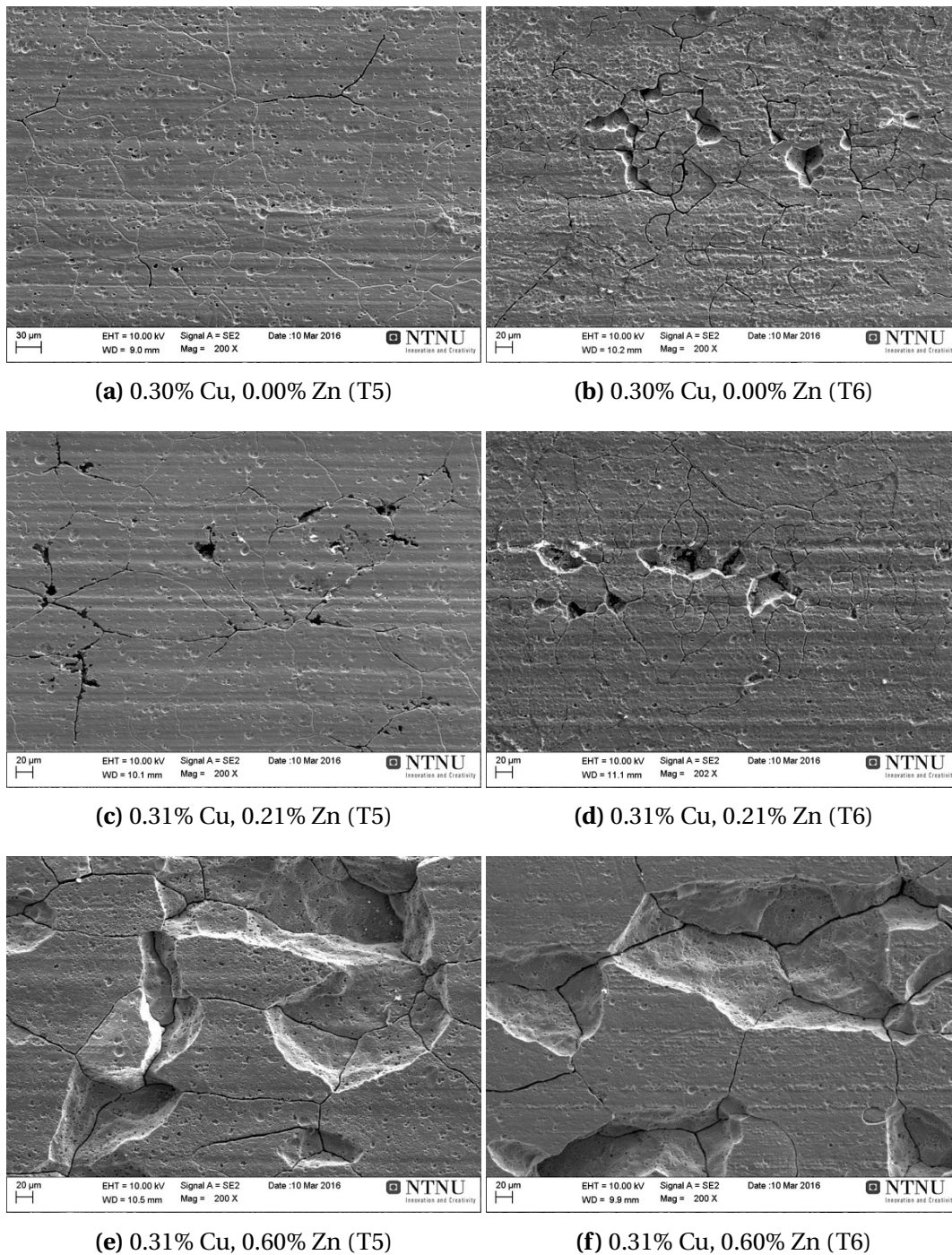


**Figure 4.11:** SEM images (200X) of surface after corrosion testing in a standard manner on selected specimens (parallel 1), and the difference in corrosion behaviour with ageing treatment and composition. Alloy composition given in wt% .

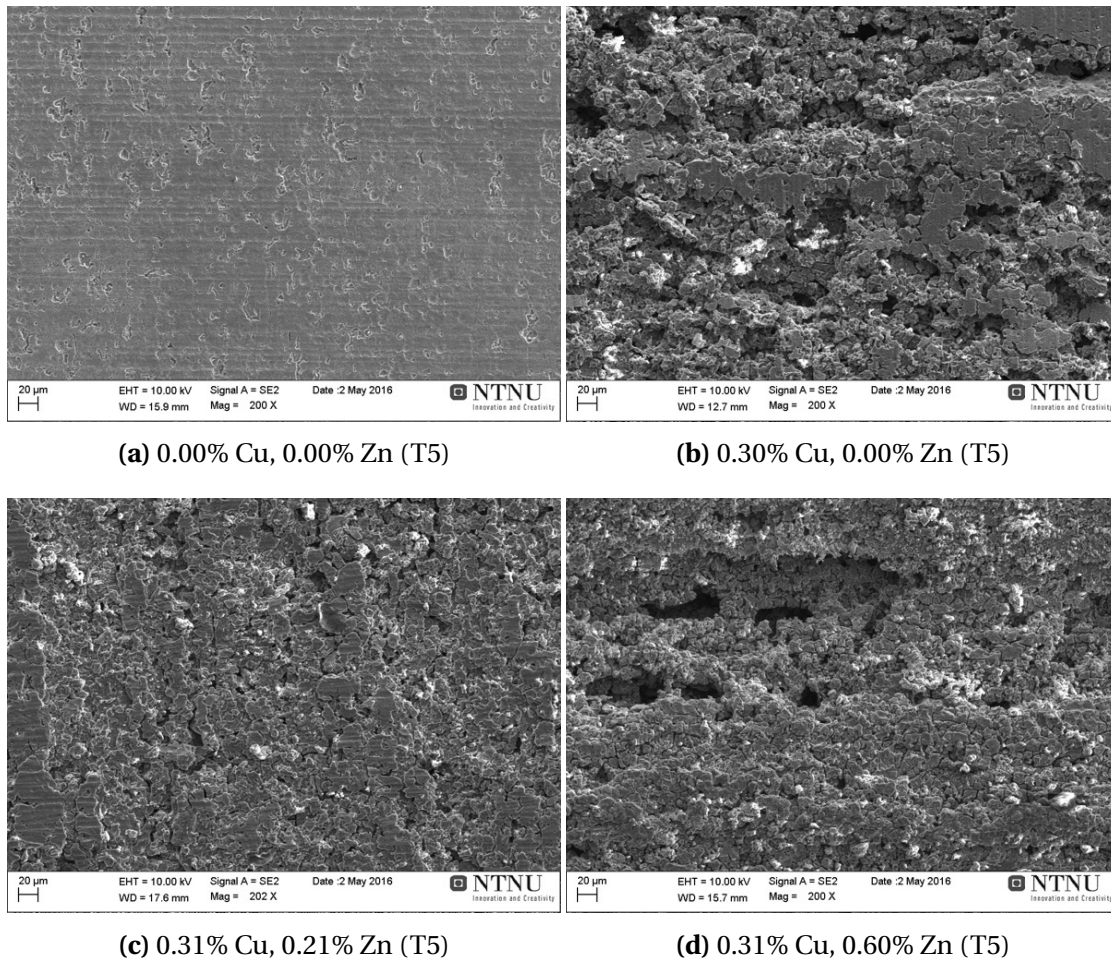


**Figure 4.12:** SEM images (200X) of surface after corrosion testing on specimens ground to fibre structure (parallel 4), and the difference in corrosion behaviour with chemical composition. Alloy composition given in wt% .

## 4.5 OCP measurements

OCP measurements were primarily conducted to examine if differences in OCP between edges and surface on the same alloy could be detected, due to the dissimilar microstructure. The test was carried out using the test electrolyte provided by the BS-ISO 11846 (method B) standard [78], the same electrolyte used during IGC testing. In addition, the OCP was measured for 24 h. Results from the other OCP parallel can be found in Appendix E. A graphic presentation of the OCP measurement of the 0.30 wt% Cu, 0.00 wt% Zn alloy is found in Figure 4.13 for the edge and the surface, respectively.

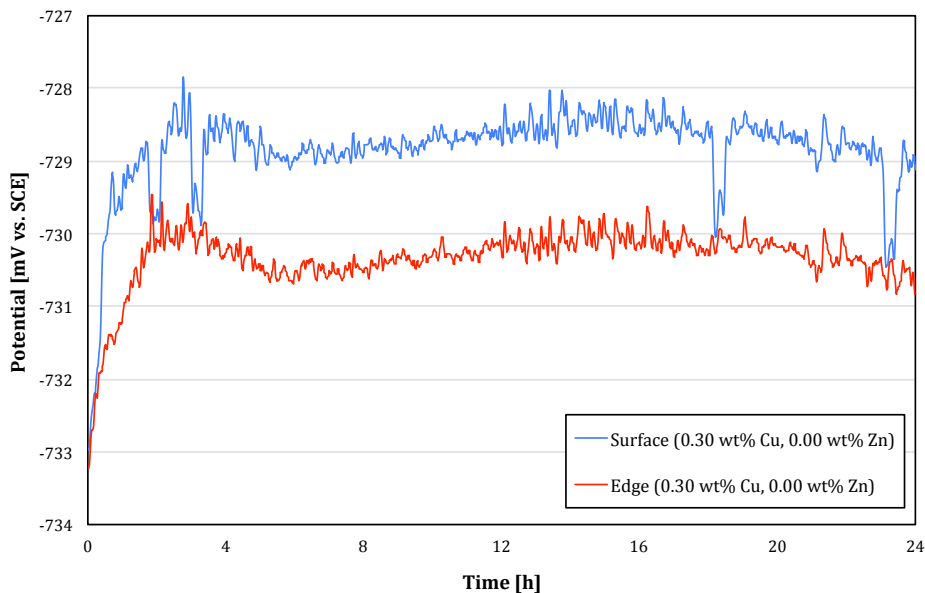


**Figure 4.13:** 24 h measurement of OCP on the surface and edge, respectively, of the 0.30 wt% Cu, 0.00 wt% Zn profile in the T5 temper.

The OCP curve measured from the edge was lower than at the surface, although the potential difference is rather small and remains fairly constant at approximately 1.5 mV. The OCP curves for both areas behave quite correspondingly throughout the experiment. Both show an increase in potential right after the immersion, however the OCP stabilises around 3 h into the measurements.

Even though the OCP measurements have a potential difference of only 1.5 mV between the edge and surface, images of the corroded areas presented in Figure 4.14 strongly suggest that the edge has suffered from heavier corrosion than the surface. Numerous pits are distributed uniformly on the entire surface sample, however they are relatively widely spaced compared to the denser corrosion attack seen on the edge sample. The corrosion attack on the edge sample seems to be confined to the fibrous region of the extruded specimen, seen as the darker grey area in the centre

of the edge.

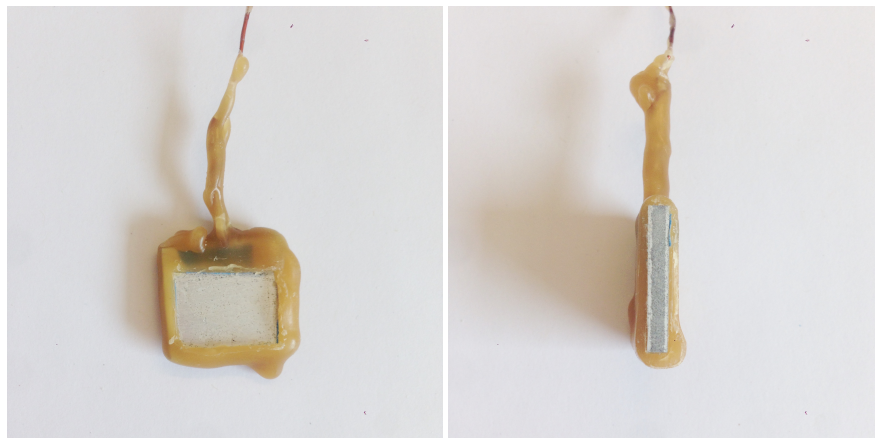


**Figure 4.14:** Images of the corrosion damage on the surface and edge of the 0.30 wt% Cu, 0.00 wt% Zn, after 24 hour OCP measurement in the BS-ISO 11846 (method B) test solution.

Figure 4.15 shows the graph visualising OCP measurements performed on the 0.31 wt% Cu, 0.60 wt% Zn profile respectively for the edge and surface. Both the edge and surface potential reveals a more active behaviour during the first hour, whereas an increase in OCP occurs subsequently over a wide time interval.

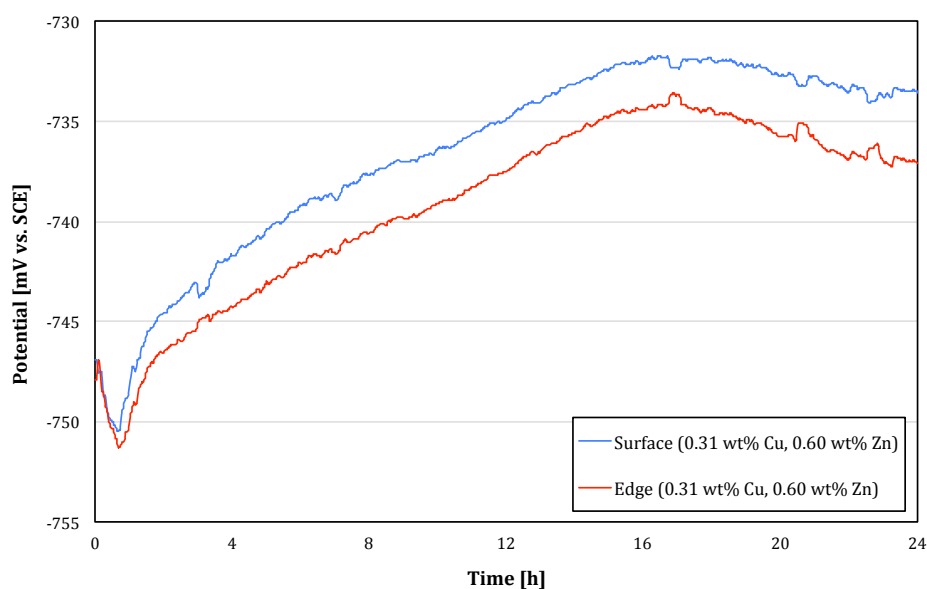


**Figure 4.15:** 24 h measurement of OCP on the surface and edge, respectively, of the 0.30 wt% Cu, 0.60 wt% Zn profile in the T5 temper.



The OCP values seem to stabilise for both areas around 12 h after immersion. Furthermore, the curves display a similar behaviour throughout the entire experiment. A potential difference of approximately 2.5 mV is observed between the edge and surface, and similarly to the 0.30 wt% Cu, 0.00 wt% Zn profile, the potential difference is rather small.

Although the difference in OCP between the edge and surface is nearly insignificant, the corrosion extent experienced by the two areas are somewhat different. Figure 4.16 shows images of the two test specimen after OCP measurement. The surface sample has been heavily corroded, and the irregularly shaped pits resembles grain detachment caused by IGC. The edge sample on the other hand, show a clearly confined area that has suffered from severe corrosion. The confined corroded region on the edge appear to correspond to the fibrous microstructure of the sample. A weak interaction between the samples seems to occur throughout the measurements, as the curves appear to mirror each other at irregularities.

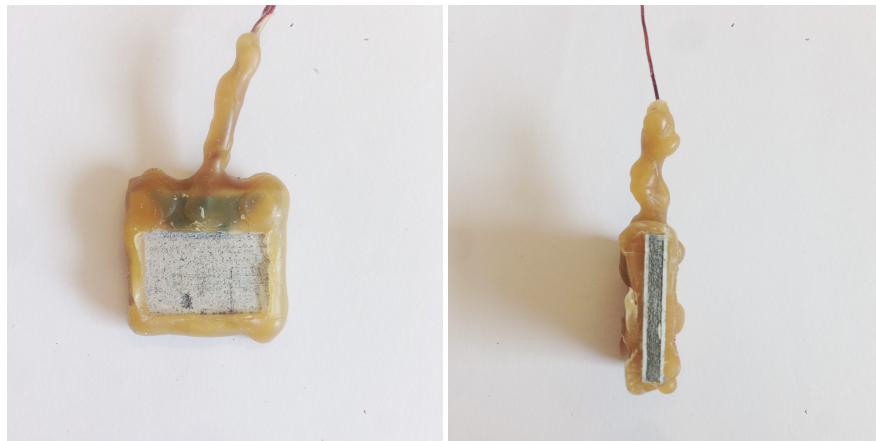


**Figure 4.16:** Images of the corrosion damage on the surface and edge of the 0.31 wt% Cu, 0.60 wt% Zn, after 24 hour OCP measurement in the BS-ISO 11846 (method B) test solution.

## 4.6 Grain boundary analysis and STEM imaging

STEM imaging and EDS analysis was conducted on the 0.31 wt% and 0.60 wt% Zn profile in the T5 temper on a high angle boundary and a low angle boundary. Images are taken parallel to the extrusion direction, i.e. images visualises down the fibre direction. The distinction between high and low angle boundary was done by comparing diffraction patterns, in addition to comparing the orientation of the particles on each side of the boundary. Diffraction patterns are presented in Appendix D. Line scans of the alloying elements at the grain boundaries were also collected. All images and data from the STEM and EDS analysis were acquired by John C. Walmsley from SINTEF Materials and Chemistry.

### High angle grain boundary

Figure 4.17 shows overview images of the high grain boundary to be analysed at two different magnifications. Elemental maps from the grain boundary in Figure 4.18 are taken of the highlighted area in Figure 4.18a. The elemental maps show that a PFZ primarily depleted of Mg and Si. The depletion of Cu is rather narrow, although the formation of the Cu rich film on the grain boundary is very clear. The images however do not show any evident segregation of Zn, though a slight enrichment of Zn on the grain boundary is detected. Nevertheless, the enrichment is not as pronounced as for Cu. An interesting observation here is that Zn has been partly incorporated in the depicted precipitate together with Mg, Si and Cu. The high detection of Mg, Si and Cu indicate that the precipitate is some type of Q phase.

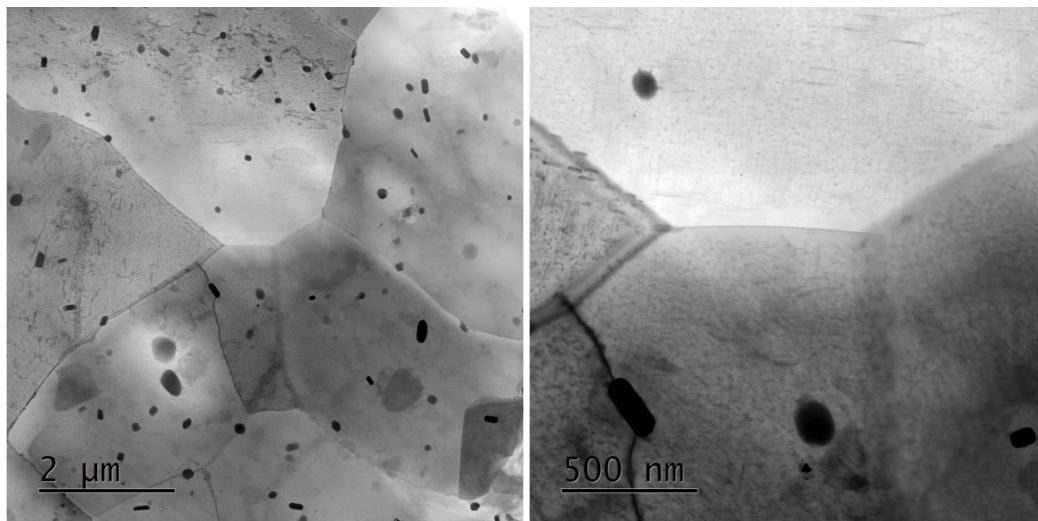


**Figure 4.17:** STEM images of the low angle grain boundary microstructure and a detailed image of the grain boundary and intermetallic particle to be analysed.

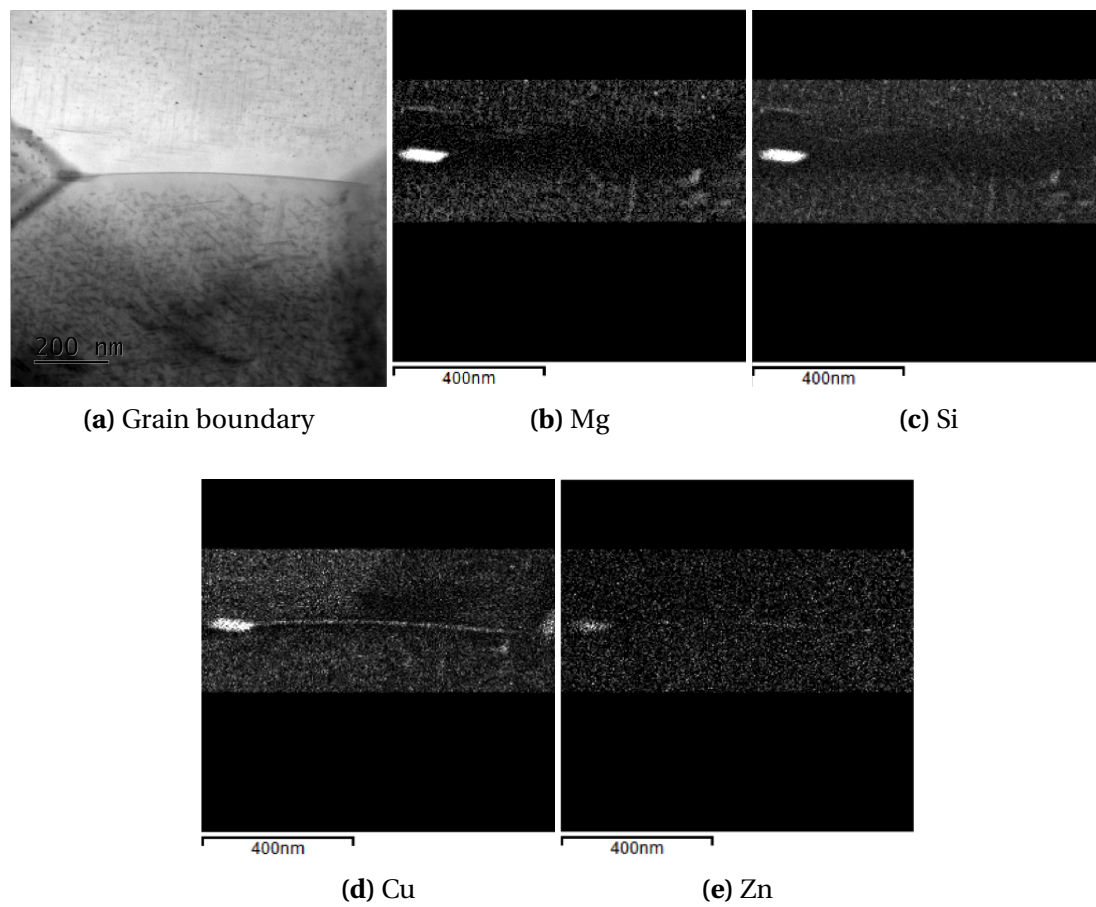


**Figure 4.18:** STEM mapping analysis of the grain boundary depicted in Figure 4.17 for profile 0.31 wt% Cu and 0.60 wt% Zn in T5. All linear scales are 400 nm, except from the linear scale in Figure 4.18a which is 200 nm.

### Low angle grain boundary

Figure 4.19 show parts of a low angle grain boundary in the 0.31 wt% Cu and 0.60 wt% Zn profile in the T5 temper. Figure 4.20 presents selected elemental maps of the grain boundary depicted in Figure 4.20a. The grain boundary appears to be densely decorated with precipitates rich in Mg and Si, although a slight detection of Cu can be observed. The PFZ is mainly depleted of the main alloying elements Mg and Si, and any depletion of Cu is hardly visible. Furthermore, the expected formation of a Cu enriched film at the grain boundary is not evident in this elemental map, in contrast to the elemental maps of the high angle grain boundary.

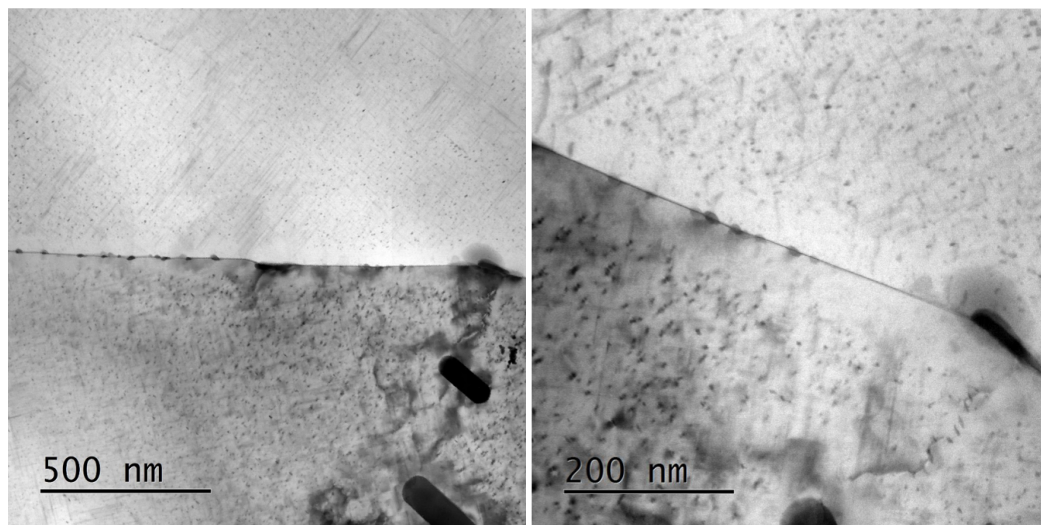


**Figure 4.19:** STEM images of the high angle grain boundary microstructure and a detailed image of the grain boundary and intermetallic particle to be analysed.

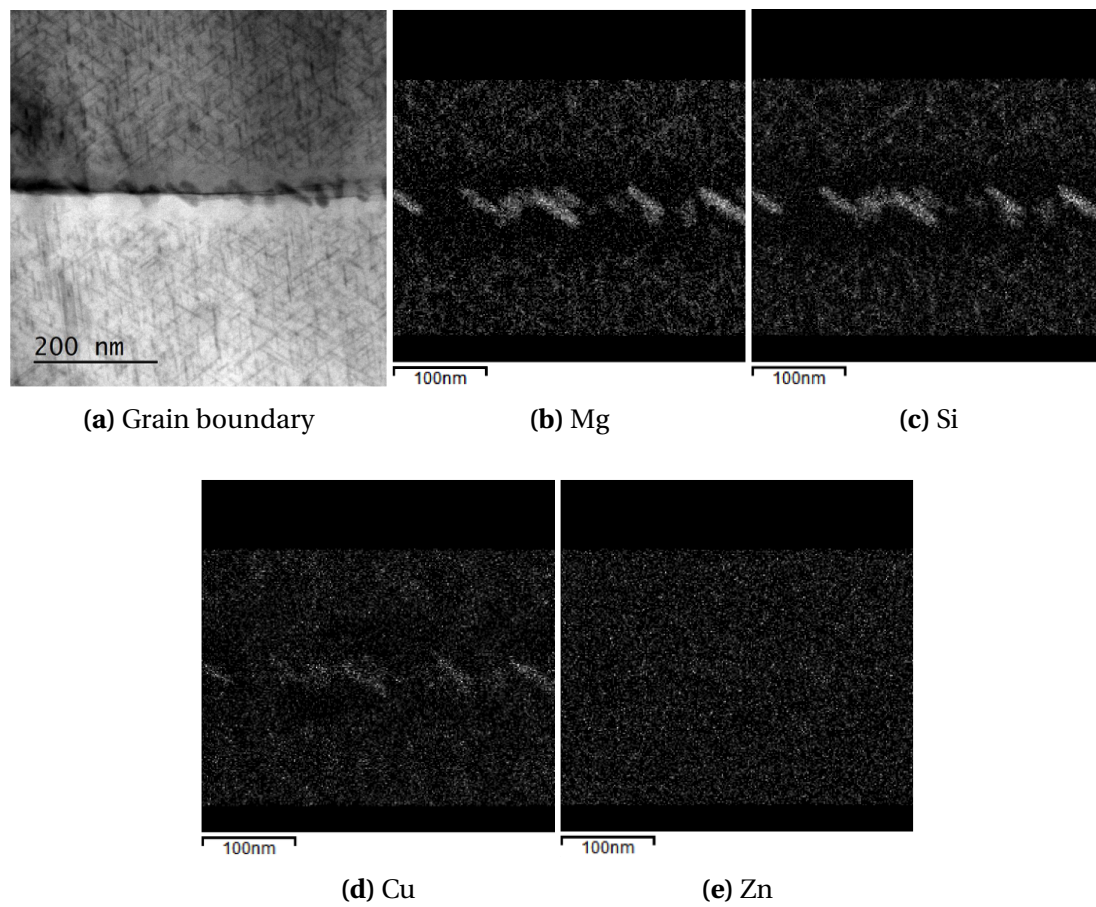


**Figure 4.20:** STEM mapping analysis of the grain boundary depicted in Figure 4.17 for profile 0.31 wt% Cu and 0.60 wt% Zn in T5. All linear scales are 100 nm, except from the linear scale in Figure 4.18a which is 200 nm.

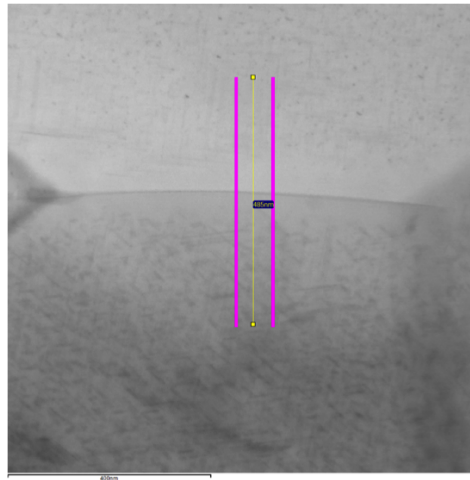
### EDS line scans of the grain boundaries

EDS line scans were collected to quantify the segregation of the alloying elements across the grain boundaries and are supplementary to the EDS elemental maps presented in Figure 4.18 and 4.20. The grey dotted line in Figure 4.22 and 4.24 represent the approximate location of the grain boundary.

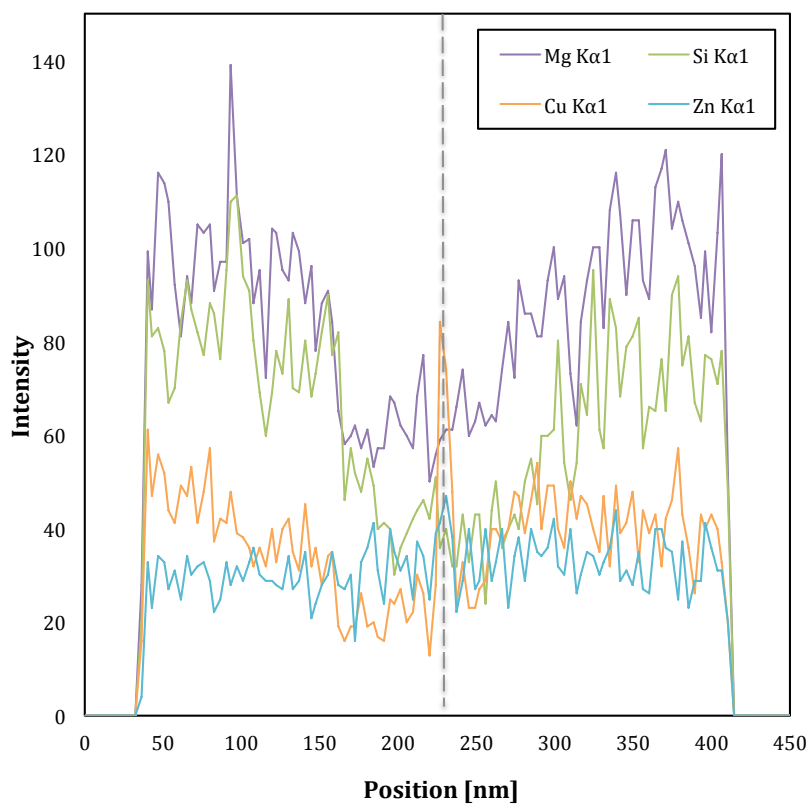
A line scan from the high angle boundary is presented in Figure 4.22 and the highlighted scanning area is shown in Figure 4.21. The line scan shows depletion of the primary alloying elements Mg and Si near the boundary, as seen in the elemental maps in Figure 4.18b and 4.18c. Zn on the other hand seems to be evenly distributed across the boundary, i.e. there is no apparent indication of any segregation for this particular area even though some enrichment can be detected on the elemental map in Figure 4.18e. The intensity of Cu reaches a narrow peak around the area of maximum depletion of Mg and Si, pointing towards the existence of a Cu enriched layer at the grain boundary. A slight depletion of Cu can be detected on the left side of the peak.

Figure 4.23 shows the scanning area of the low angle boundary whilst the line scan is presented in Figure 4.24. The analysed grain boundary was decorated with small particles, which is evident in the line scan retrieved. The scans show a wide area enriched in Mg and Si, indicating a particle enriched in these elements. Depletion of Mg and Si can be observed in either side of the peak, whereas depletion of Cu is not readily seen, although a slight depletion can be detected. Zn however seems to have remained in solid solution as no segregation is found from the line scan. Furthermore, no pronounced enrichment of Cu at the grain boundary can be observed either, or at least no significant incorporation of Cu in the particle is seen.





**Figure 4.21:** Line scan of the high angle boundary was taken from the highlighted area. Scanning was done across the boundary with a total width of 485 nm. Linear scale of the image is 400 nm.



**Figure 4.22:** A line scan of the highlighted area from Figure 4.21 on the high angle boundary, showing distribution of main alloying elements across the grain boundary. The grey dashed line indicates the approximate location of the grain boundary.

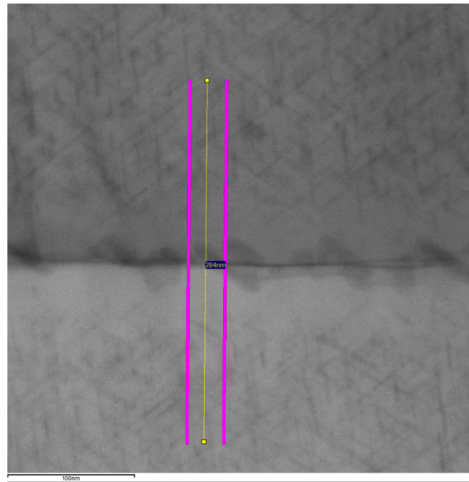


**Figure 4.23:** Line scan of the low angle boundary was taken from the highlighted area. Scanning was done across the boundary with a total width of 281 nm. Linear scale of the image is 100 nm.

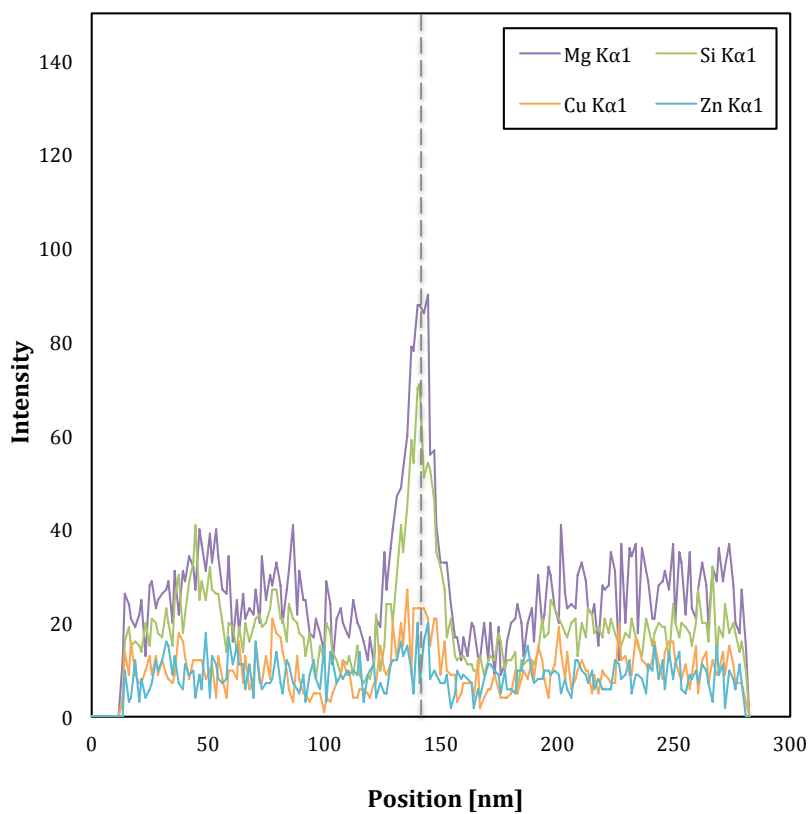


**Figure 4.24:** A line scan of the highlighted area from Figure 4.23 on the low angle boundary, showing distribution of main alloying elements across the grain boundary. The grey dashed line indicates the approximate location of the grain boundary.



## Chapter 5

# Discussion

### 5.1 Effect of heat treatment and alloy composition on hardness properties

Results from Vickers hardness testing indicate that solution heat treatment after extrusion on Cu containing alloys give a slight increase in surface hardness, as detailed section 4.2. Claiming that solution heat treatment improves hardness properties from these results are however disputable, especially when the standard deviation values are taken into account. Considering the calculated errors, the difference in hardness between the T5 and T6 temper is rather minimal. This can be accounted for by the similarity in surface layer microstructure, seen in Figure 5.1, and the identical ageing treatment carried out in both tempers. Notwithstanding, the separate solution heat treatment might result finer precipitates during ageing, which can explain the minor increase in hardness. This process will anneal out dislocations and reduce the precipitation rate, whereas as-extruded profiles have higher dislocation density which facilitates higher precipitation rates, as already elaborated in section 2.3.3. Accelerated precipitation kinetics have been suggested to form coarser particles [63].

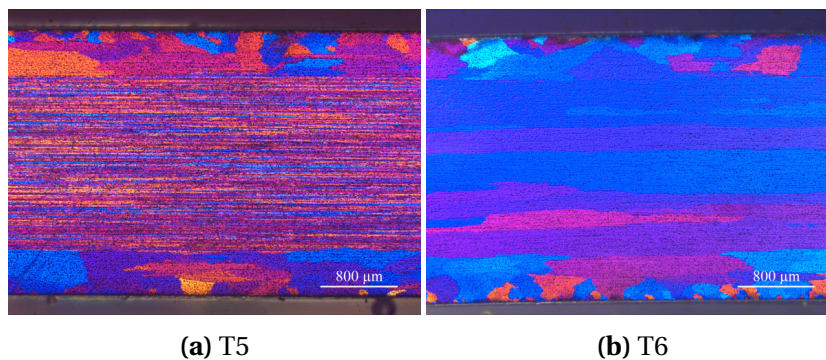


**Figure 5.1:** The difference in microstructure on a 0.00 wt% Cu, 0.00 wt% Zn alloy in the T5 and T6 temper, respectively. The recrystallised surface layer in both tempers is however similar.

Other mechanical testing methods might have revealed a larger difference in for instance tensile

strength between the tempers, especially due to the heterogeneous microstructure characteristic for the T5 profiles. The highly directional elongated grains give rise to anisotropic properties, and the mechanical features are to a large extent dependent on direction. Solution heat treatment after extrusion has caused complete recrystallisation of the fibrous region achieved after extrusion, probably due to the Mn dispersoids being unable to impede recrystallisation of the fibrous grains at the given temperature and holding time.

Nevertheless, alloying with Cu has the largest impact on raising hardness in these alloys. As elaborated in section 2.2, the presence of Cu in AlMgSi alloys will improve the hardening potential during ageing due to several mechanisms. The formation of quaternary precipitates, as the reported L phase, contribute to strengthening in combination with the  $\beta''$  phase. In addition, the presence of Cu leads to finer precipitate microstructure, dispersion and a higher precipitate volume fraction. On the contrary, alloying with Zn did not have any significant effect on the hardness. As reported by Saito et al. [46], Zn remained mainly in solid solution when added to AlMgSi alloys. Results from the EDS analysis supports this finding. Although alloying elements in solid solution contributes greatly to strengthening in some alloys, this mechanism is not as effective in age hardenable alloys. The strengthening from hardening phases and precipitates is more significant, and the strong influence in hardness from Cu may have suppressed the hardening effect Zn had in the study by Saito et al. [46].

## 5.2 IGC susceptibility in AlMgSi(Cu,Zn)

One of the main objectives of this work was to evaluate whether the addition of Zn could reduce the IGC susceptibility in copper containing AlMgSi alloys. The proposed mechanism was that Zn could segregate to the grain boundaries during artificial ageing and reduce the cathodic nature of the grain boundary film. The Cu rich film found in quaternary AlMgSi alloys increases the electrochemical potential difference between the grain boundary and the anodic PFZ. If Zn was to precipitate along with Cu, the potential difference was believed to be reduced, concurrently the driving force for IGC. However, the results obtained from this work indicate strongly that the presence of Zn has a detrimental effect on IGC resistance, thus contradicting the initial hypothesis.

The tested profiles were heat treated to the T5 and T6 temper. Other than heat treatment, the variation in Cu and Zn level is the primary consideration when the IGC susceptibility is assessed. The only difference between the T5 and T6 temper is a separate solution heat treatment after extrusion on the latter. Apart from SHT, both tempers have been artificially aged to peak hardness. The following discussion is based on the results retrieved from the IGC tested edge covered specimens (parallel 2), in order to eliminate any influence edge effects may have on the corrosion morphology on the surface. This matter will be addressed in further sections.

### 5.2.1 Effect of Zn on IGC susceptibility in T5 and T6 profiles

For the T5 tempered profiles, the addition of Zn to 6082 alloys containing 0.31 wt% Cu had a detrimental effect on the IGC resistance. No change in corrosion depth was observed when 0.21 wt% Zn was added, although weight loss increased. From Figure 5.2b, it appears that the addition of Zn has led to cavity widening rather than deeper IGC attacks. IGC was strongly accelerated when the Zn content reached 0.60 wt%, as the measured corrosion depth and weight loss values increased significantly. The severity of IGC is primarily evaluated on the premise of measurements presented in Table 4.4. Nonetheless, the IGC in the maximum Zn profile seems to propagate deeply into the material without extensive spreading along grain boundaries parallel to the working direction, seen in Figure 5.2c. The difference is distinctive if compared to the corrosion damages found in Figure 5.2a and 5.2b. This behaviour seems to have an effect on large grains detaching from the surface in these high Zn alloys, also seen in SEM images presented previously in Figure 4.11e. The increased weight loss measured in these profiles is probably owed to this.

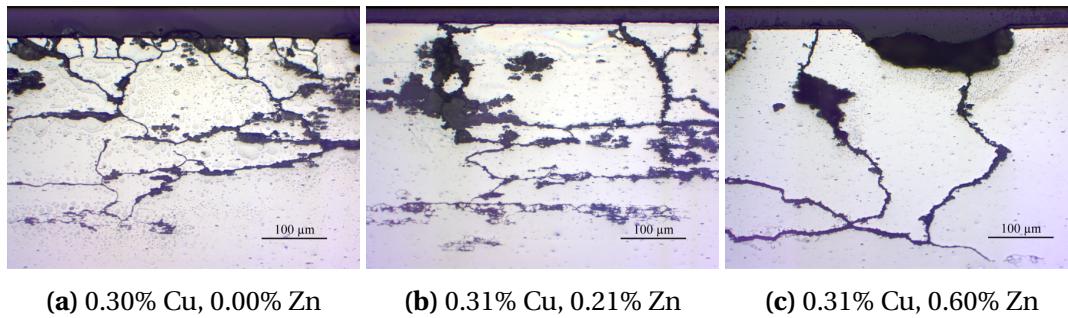


**Figure 5.2:** Optical micrographs (20x) showing the IGC development on T5 tempered profiles with increasing Zn content. Specimens are from the edge covered test parallel.

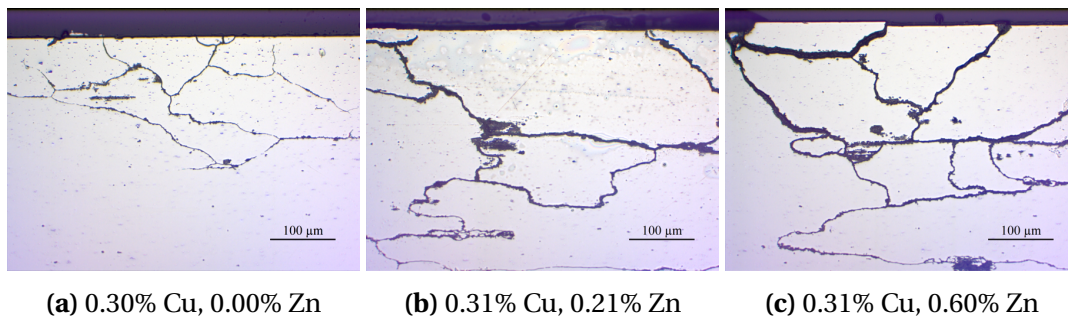


**Figure 5.3:** Optical micrographs (20x) showing the IGC development on T6 tempered profiles with increasing Zn content. Specimens are from the edge covered test parallel.

IGC susceptibility in the T6 tempered profiles reveal similar trends as for the T5 profiles. The IGC attacks penetrate deeper with increasing Zn content, which can be observed to some extent in

Figure 5.3. Table 4.5 show however no significant variation in weight loss when 0.21 wt% Zn is introduced, although the corrosion depth increases significantly. This is however not unusual, as IGC is not necessarily related to significant weight loss. Higher weight loss values observed for the 0.60 wt% Zn alloy, are most likely caused by grain fallout due to extensive IGC, as observed for the identical alloy in the T5 temper. Corrosion depth was also increased when the Zn level reached 0.60 wt%.

A noteworthy difference between the T5 and T6 temper is that the Cu and Zn free profile in the T5 condition is completely resistant to IGC, whereas the T6 temper has experienced some local, although shallow IGC attacks. A comparison is found in Figure 5.4. Additional solution heat treatment after extrusion seems to introduce some IGC susceptibility in copper free AlMgSi alloys. Even though sign of IGC is evident in this alloy, the extent of the damages attained from this accelerated test is not considered as practically significant [63]. As no amount of Cu and Zn is present, the source of IGC is likely to be caused by Si in excess. Regardless, the seemingly detrimental effect Si in excess may have on IGC resistance in the T6 condition cannot be of great importance, since IGC is not apparent for the same alloy in T5 condition.

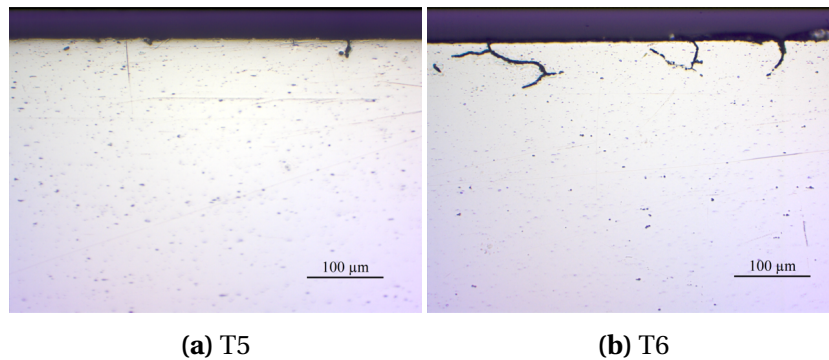


**Figure 5.4:** Optical micrographs (20x) showing the IGC susceptibility in a Cu and Zn free 6082 alloy in the T5 and T6 condition, respectively. Specimens are from the edge covered test parallel.

Another observation is the difference in IGC morphology, as seen in Figure 5.2. IGC propagation in T6 leads to narrow and deeper corrosion depths, while the propagation development in T5 seems to favour cavity widening resembling pitting. The increased dislocation density in the T5 profiles may have led to coarser particle precipitation as already described in the aforementioned section. Since Cu is partly incorporated into these particles, enrichment of Cu might occur during corrosion when the more anodic constituents are leached out. This can possibly elucidate the widened and pitting-like IGC morphology on the temper which has not been solution heat treated after hot deformation. Furthermore, the pitting-like morphology on the T5 temper explain the higher weight loss experienced, compared to the T6 profiles. IGC depth also seemed to increase when 0.21 wt% Zn was added to a T6 temper, whereas the depth in the T5 alloy remained relatively un-

changed. These assertions cannot be fully disclosed with certainty however, as the difference is not very obvious.

Nevertheless, Zn seems to achieve the same effect on IGC susceptibility in both tempers. IGC was introduced when 0.30 wt% Cu was added, and the corrosion extent increased when the Zn level was raised to 0.21 wt% Zn. The corrosion rate accelerated even further when the maximum Zn level of 0.60 wt% was reached.

### 5.2.2 Effect of Zn on grain boundary chemistry

Analysis of the grain boundary chemistry in a 0.31 wt% Cu, 0.60 wt% Zn alloy in T5, revealed an enrichment of Cu along the grain boundary, confirming the frequently reported Cu rich film [10, 66–68]. The elemental map of Zn showed a only a slight enrichment at the grain boundary, although not nearly evident as for Cu. The reported Zn film found in a 1 wt% Zn AlMgSi alloy by Saito et al. is not as apparent in these results. Furthermore, the existence of a PFZ was found as the elemental maps of Mg and Si showed extensive depletion at the area adjacent to the grain boundary. Depletion of Cu was not as visible, although a narrow area absent of Cu was detected near the Cu rich film. No depletion of Zn was observed and Zn seemed to mostly remain in solid solution. These observations contribute to elucidate the mechanism for the observed IGC attacks on the T5 tempered alloys.

Firstly, IGC susceptibility commences when 0.30 wt% Cu is introduced, due to the formation of a highly cathodic Cu rich film at the grain boundaries. At the same time, diffusion of Mg and Si atoms renders the adjacent area depleted of solute atoms, resulting in an active PFZ. In corrosive media, extensive IGC occurs due to the preferential dissolution of the PFZ. When Zn is eventually added, the alloying element is initially found in solid solution with the Al matrix. Since Zn is more anodic compared to Al in acidified seawater, a potential reduction occurs in the matrix. Contemplating that nobler elements diffuses towards precipitates while Zn remains, the anodic nature of the PFZ is enhanced. Since the Cu rich film is still present, the IGC mechanism is accelerated due to the increase in potential difference. The driving force for IGC is escalated even further when the Zn content increases to 0.60 wt%. Consequently, the observed enhancement of IGC severity in zinc containing AlMgSi(Cu) alloys compared to conventional ones, is owed to the further activation of the PFZ caused by Zn remaining in solid solution. Alloying AlMgSi(Cu) alloys with Zn did not achieve an equivalent effect as alloying with Mg in excess, described by Holmestad et al. [13].

The TEM images also revealed that the larger precipitates mainly consisted of Mg and Si, although large amounts of Cu was also incorporated. Zn however was not as readily incorporated, indicating that the mobility of the aforementioned elements are of a larger magnitude. The low mobility of Zn is probably due to the high solubility of Zn in Al. A Zn rich film on the grain boundary is therefore

not readily achieved in the investigated alloys, although Saito et al. observed a film when Zn level reached 1 wt%. Perhaps a film can be formed when the Zn content reaches an appreciable level. However, this will not necessarily contribute to reduce the overall IGC susceptibility, as more Zn is probably to be found in solid solution with the PFZ. Hence, the desired electrochemical potential difference between the boundary and PFZ may not be considerable enough to eliminate IGC entirely. Even though the elemental maps did detect a slight enrichment of Zn at the grain boundary on the 0.60 wt% Zn profile, the line scan showed that the concentration of Zn was fairly constant. The low amount of Zn enrichment at the boundary is possibly not enough to compensate for the potential difference caused by the Cu film and a Zn rich PFZ.

### **5.3 Effect of edge corrosion on evaluation of IGC susceptibility based on BS-ISO 11846**

A series of IGC tests conducted according to BS-ISO 11846 was carried out to investigate how the edge microstructure affected the obtained results. Testing was performed as specified in Table 3.2. Evaluation of IGC susceptibility of samples after testing was carried out by metallographic examination of the specimen surface. Previous experience has revealed that these particular alloys suffer from considerable corrosion from the edges in the T5 temper, and the obtained results have indicated that the extensive edge corrosion has led to less corrosion on the surface [14]. The results presented in the current thesis indicate strongly that corrosion of the fibrous region from the edges in the T5 profiles has a substantial effect on the corrosion behaviour of the surface on certain alloys. The influence from edge corrosion has been of such extent that any surface corrosion has been entirely concealed on susceptible materials. Especially the 0.30 wt% Cu, 0.00 wt% Zn alloy in the T5 temper, which is known to be highly susceptible to IGC in literature, has shown to be strongly affected. The subsequent discussion will also attempt to elucidate the mechanism behind this phenomenon.

#### **5.3.1 Effect of edge microstructure**

Profiles were aged to the T5 and T6 temper in order to achieve two dissimilar microstructures, as seen in Figure 5.1. As already stated, the recrystallised surface layer is fairly similar between the two conditions, however the microstructure achieved after extrusion is completely recrystallised in the T6 temper. Concurrently, a distinctive edge microstructure is found for each temper. It should be emphasised that the term «edge» in this thesis refers to the cut surface perpendicular to the extrusion direction.



The top row in Figure 5.5 shows the corrosion damages on the 0.31 wt% Cu, 0.21 wt% Zn alloy in the T5 temper, while the corresponding alloy in the T6 condition is presented in the bottom row. The test was carried out in a standard manner (parallel 1) with an exposed specimen area of roughly 10 cm<sup>2</sup>.

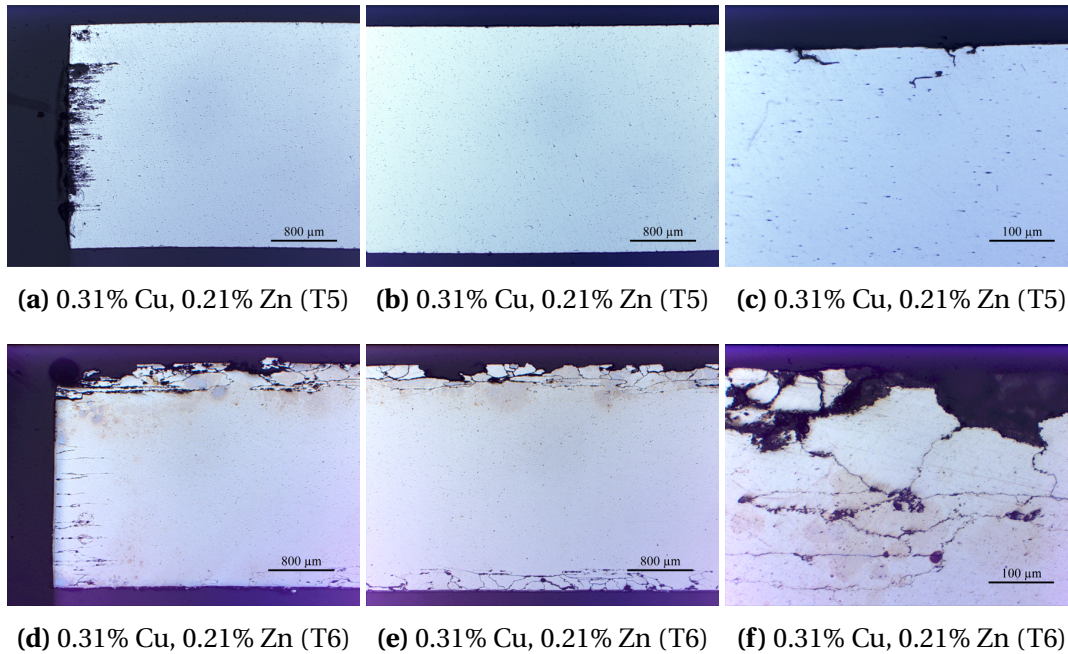


**Figure 5.5:** Optical micrographs (2.5x, 20x) showing the difference in edge and surface corrosion on a 0.31 wt% Cu, 0.21 wt% Zn alloy in the T5 and T6 temper, respectively. Specimens are from the initial testing (parallel 1), with a specimen area of approximately 10 cm<sup>2</sup>. Alloy content is given in wt%.

The most noteworthy observation from this comparison is the difference in extent of surface corrosion between the T5 and T6 microstructure. The specimen surface of the T5 temper is essentially resistant to IGC, only one shallow attack was located. On the contrary, the 6082 profile in the T6 condition suffered from severe IGC on the surfaces. However, the T6 profile does not experience significant corrosion initiated from the edges, whereas this is clearly seen on the T5 profile. Corrosion on the T5 temper appears to occur on the fibrous edge rather than the recrystallised surfaces. The edge is densely corroded and appear to be restricted to the fibrous region of the material. Based on the obtained results, the negligible amount of edge corrosion on the T6 specimens is most likely due to the absence of a fibrous edge.

### 5.3.2 Effect of covering edges

In order to investigate if the exposed fibre structure contributed to the reduced IGC initiation on the recrystallised layer, specimens were subjected to IGC testing with covered edges. The edges were covered with beeswax and the total exposure area was  $10\text{ cm}^2$ , restricted to the recrystallised surface. The total exposure area during IGC testing with covered edges was identical to the previous test, so that any ambiguity related to sample size was eliminated. A comparison of selected results from IGC testing carried out with and without covered edges (parallel 2) is presented in Figure 5.6, and show optical micrographs of a 0.30 wt% Cu, 0.00 wt% Zn alloy in the T5 temper.

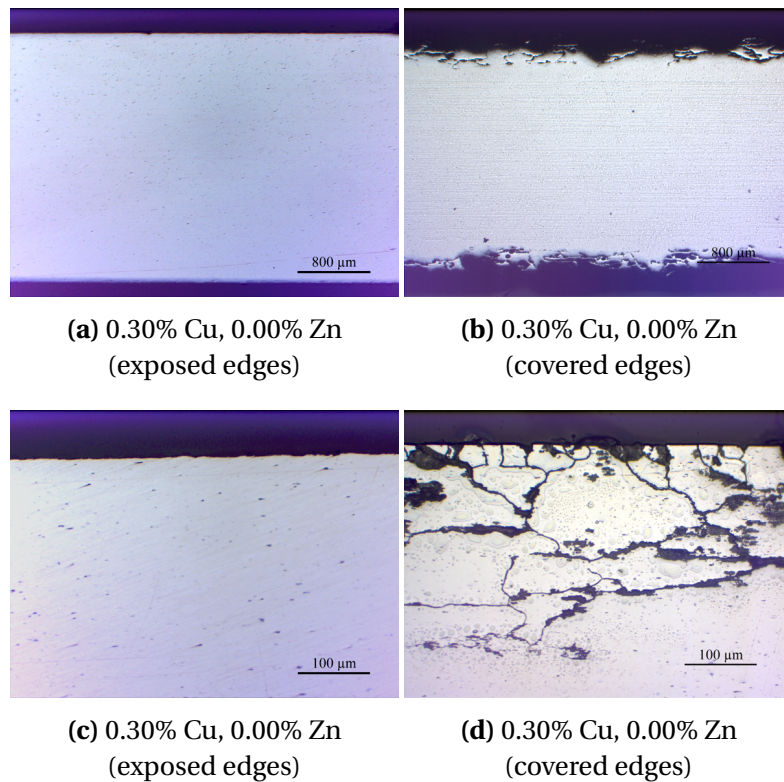


**Figure 5.6:** Optical micrographs (2.5x, 20x) showing the difference in corrosion damage on a 0.30 wt% Cu, 0.00 wt% Zn alloy in the T5 temper with covered and exposed edges, respectively. Alloy content is given in wt%.

The results showed that substantial IGC had occurred on the edge covered sample compared to the one with exposed edges. It can be seen in both Figure 5.6a and 5.6c that the surfaces show no sign of IGC when the edges are exposed during testing. In contrast, the edge covered specimen in Figure 5.6b and 5.6d have suffered uniform IGC with an average IGC depth of  $277\text{ }\mu\text{m}$ . A similar result was also experienced for the 0.30 wt% Cu, 0.00 wt% Zn alloy in the T5 temper. These results are quite remarkable, especially when considering that the two specimens are of the same alloy, size and



temper. The one single difference is the exposure of edges during accelerated testing, which is another indication that edge corrosion has a significant effect on the corrosion behaviour of the recrystallised surface. The only alloy which reveal uniform IGC on the surface was the 0.31 wt% Cu, 0.60 wt% Zn profile, which suggests that this alloy is most susceptible to IGC.

Furthermore, to be entirely certain that edge corrosion of the fibrous texture was the main cause for concealing IGC susceptibility, IGC testing on edge covered T6 specimens was also carried out. Figure 5.7 shows results for the 0.30 wt% Cu, 0.00 wt% Zn alloy in the T6 condition. The type and extent of surface corrosion on specimens with and without exposed edges is fairly identical. Cavity widening is more pronounced however on the exposed edge specimen. As described previously, the T6 temper does not experience edge corrosion to a large degree, hence covering the edges does not result significant increase in IGC on the surface in contrast to what is observed on the T5 profiles. The risk of concealing IGC susceptibility is only evident for the T5 profiles with a fibrous grain structure.

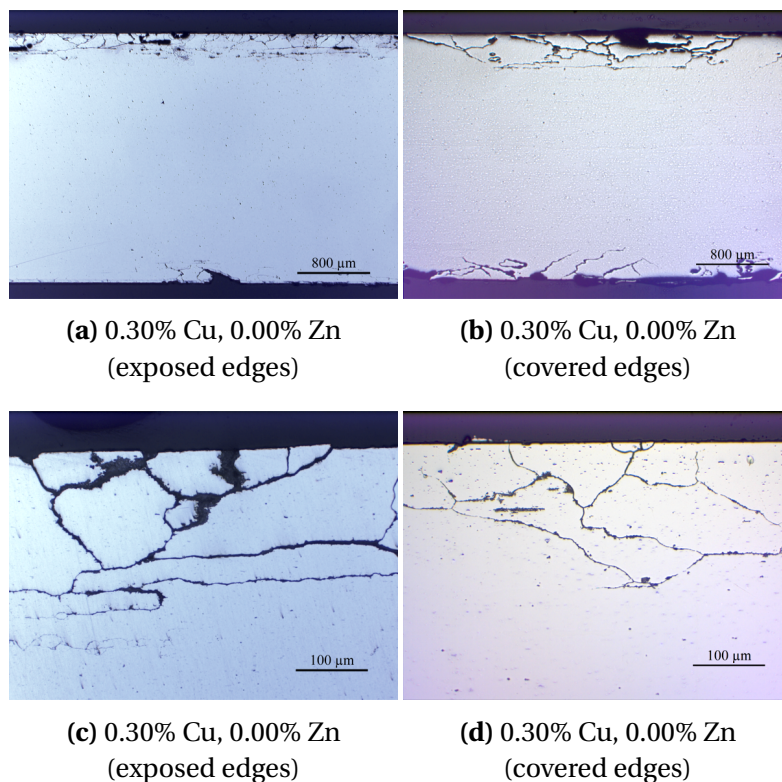


**Figure 5.7:** Optical micrographs (2.5x, 20x) showing the difference in corrosion damage on a 0.30 wt% Cu, 0.00 wt% Zn alloy in the T6 temper with covered and exposed edges, respectively. Alloy content is given in wt%.

The cut surface perpendicular to the extrusion direction exposes the the fibre structure to corrosive media. As the fibrous region has a high grain boundary density, the cut surface provides numer-

ous of favourable sites for corrosion initiation, resulting in the observed edge corrosion. The lower amount of accessible grain boundaries on the recrystallised surface may render the cut surface, i.e. the edges, more preferable sites for corrosion initiation. The Al matrix on the cut surface has a high degree of heterogeneities facilitated by the numerous grain boundaries, and the oxide layer may therefore not be as stable or easily re-passivated compared to the oxide layer on the recrystallised surface. In other words, the cut surface exposing the fibrous structure might act similarly to a sacrificial anode on the specimen during the IGC test. This can account for the more severe corrosion on the edges, while the recrystallised surface appears nearly intact.

### 5.3.3 Effect of edge to surface ratio

Another investigated factor was the sample size of the tested specimens. The BS-ISO 11846 standard recommend the specimen area not to exceed 20 cm<sup>2</sup>. An additional set of samples with the maximum allowed exposure area was tested (parallel 3). Compared to the previously discussed specimens, these samples were approximately twice the size. A small reduction of edge/surface ratio is achieved when the sample size is increased, and the edges of the larger specimen amounted to around 28% of the total area. The preceding samples sized 10 cm<sup>2</sup> had an edge area of 37-39 %. The experiment was carried out to examine whether a lower edge/surface ratio will reduce or increase the «sacrificial effect» of the edges. Figure 5.8 show a comparison of a 0.31 wt% Cu, 0.21 wt% Zn profile in the T5 temper with the two edge surface ratios.

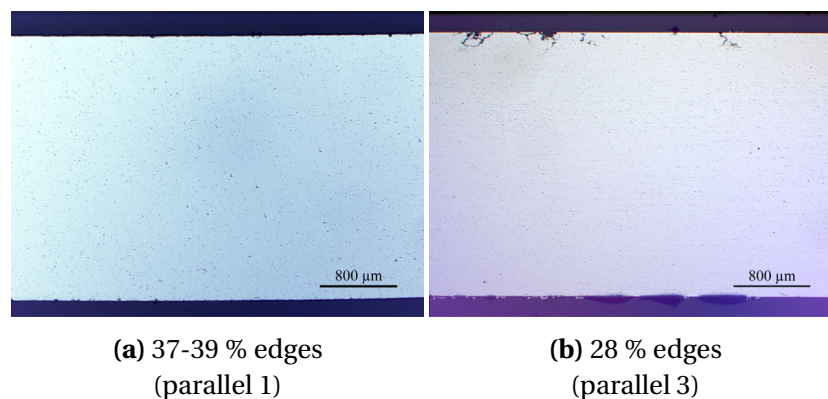


**Figure 5.8:** Optical micrographs (2.5x) showing the corrosion damages on a 0.31 wt% Cu, 0.21 wt% Zn alloy in the T5 temper with varying edge/surface ratio.

A few shallow and highly localised IGC attacks was found on the specimen with lower edge/surface ratio (parallel 3) with an average IGC depth of 192 μm, seen in Figure 5.8b, whereas the specimen with larger edge area (parallel 1) was resistant to surface corrosion. Deeper corrosion depths were also found on the 0.31 wt% Cu, 0.60 wt% Zn alloy from parallel 3. However, the difference

between these two parallels are not exceedingly evident and therefore not entirely certain. In addition, the samples with lower edge/surface ratio did suffer extensive edge corrosion. Consequently, the results do not strongly support that a lower edge/surface ratio will induce more IGC on the surfaces of susceptible profiles, as no change was observed with edge size in the 0.30 wt% Cu, 0.00 wt% Zn profile.

The weak trend observed does also contradict the theory on anode-to-cathode area related to galvanic corrosion. A lower anode/cathode ratio will increase the corrosion rate of the more active material [82]. The reason why the results contradicts this remains unclear. A possible mechanism is that the increased corrosion rate leads to greater ohmic resistance as the corrosion products build up, leading to more rapid initiation at the surface when the edges corrosion of the edges stagnates. Nevertheless, this is merely a suggestion, and the difference in edge/surface ratio between the parallels is rather minor. Perhaps a larger dissimilarity in ratio would have provided clearer results. Testing on larger samples is however restricted by BS-ISO 11846, hence a complete elimination of edge corrosion affecting the IGC-test results by increasing sample size is not possible. Caution has to be made when calculating the edge area of the specimens. If specimens are taken from the edge of the original extruded profile, one of the edge surfaces parallel to the working direction will possess a recrystallised surface.

#### 5.3.4 IGC susceptibility on fibrous region in T5 profiles

The recurring observation from IGC testing was severe corrosion from the edges on the T5 profiles, and the final test parallel (parallel 4) investigated the IGC susceptibility of the fibrous region. Prior to this test, corrosion susceptibility of this region was only observed being initiated parallel to the extrusion direction. In this parallel, the susceptibility of the fibrous region was examined transverse to the working direction. Test specimens of the T5 profiles were ground to remove the recrystallised layer in one direction, to about 2 mm thick. The opposite surface was left intact. Anodisation was carried out on one sample to ensure that the fibrous layer was reached, as seen in Figure 5.9.

Results indicated strongly that the fibrous layer was highly susceptible to IGC from the transverse direction. This was evident for all alloy compositions except the Cu and Zn free profile, which appeared essentially corrosion resistant apart from uniform etching revealed by the SEM micrograph in Figure 4.12a. The IGC susceptible alloys did experience edge corrosion, although micrographs of these damages were not acquired. An interesting observation for the 0.30 wt% Cu, 0.00 wt% Zn and 0.31 wt% Cu, 0.21 wt% Zn alloys was the absence of IGC damages on the recrystallised surface which had not been removed. It appears that the entire fibrous region in all directions are more preferable sites for IGC than the recrystallised surface layer. However, the 0.31 wt% Cu, 0.60 wt%

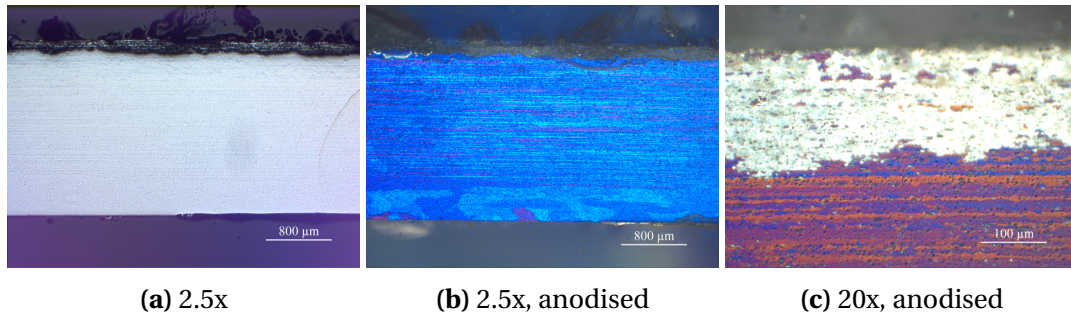


**Figure 5.9:** Optical micrographs showing the fibrous region and the microstructure after anodisation of a 0.31 wt% Cu, 0.21 wt% Zn alloy in the T5 temper.

Zn profile experienced uniform, though very shallow, IGC on the recrystallised surface as well, visualised in Figure 5.10. Again the results support that the increased Zn content render the 6082 alloys more susceptible to IGC in general. The measured average IGC depth on the fibrous surface for the maximum Zn alloy was 178 µm, similar to the profile with 0.21 wt% Zn. This alloy did however seem to experience grain fallout during cutting and polishing, one of the disadvantages related to performing metallographic examination of IGC in LM [72]. Consequently, the actual average IGC depth was probably closer to the maximum measured depth.

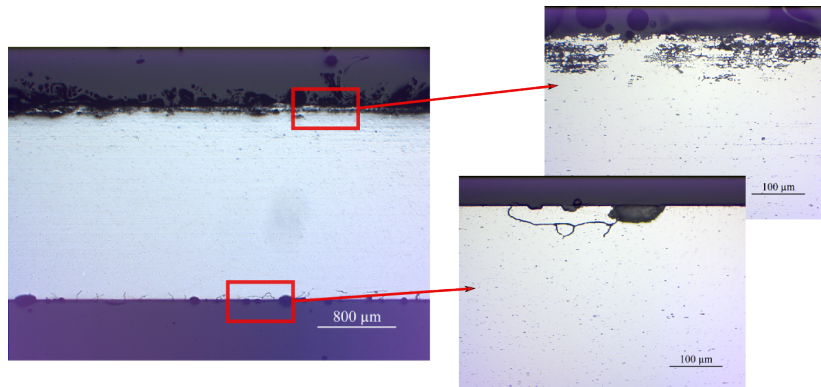


**Figure 5.10:** Optical micrographs (2.5x, 20x) showing the corrosion damages on a 0.31 wt% Cu, 0.21 wt% Zn alloy in the T5 temper with varying edge/surface ratio.

The obtained results contradict the literature review in section 2.3.3, where some studies have claimed that the fibrous region is not susceptible to IGC, at least relative to the recrystallised layer. Especially Minoda and Yoshida [61, 62] reported that a 6061 alloy, containing 0.33 wt% Cu, ground to the fibrous region did not display any significant IGC, whereas uniform IGC was found on the recrystallised surface. The two main differences between the alloy from the study and the 0.30 wt% Cu, 0.00 wt% Zn alloy investigated in this thesis is the Si content and the ageing treatment. In the study by Minoda and Yoshida, the Si level was 0.54 wt% and Mg level at 1.03 wt% while the ageing

treatment corresponded to near overageing relative to the treatment performed in this work. Si in excess, as for the current alloys, may increase IGC susceptibility together with the ageing treatment to peak hardness. Mg in excess and overageing has been reported to increase IGC resistance, as detailed in section 2.3.1 and 2.3.3. A Mg/Si ratio with Mg in excess was reported by Holmestad et al. to increase IGC resistance [13], while overageing was claimed by Svenningsen et al. to reduce IGC by coarsening the Cu film [63]. Furthermore, Minoda and Yoshida also suggested that PFZs were more likely to be found in high angle boundaries, more frequently found in recrystallised microstructures with randomly orientated grains. In contrast, PFZ were claimed to be less frequent in low angle boundaries in the highly directional microstructures [61]. The TEM studies carried out in this thesis did detect a PFZ in a low angle boundary, and the degree of depletion was fairly identical to the PFZ found in the high angle boundary, seen by comparing Figure 4.24 and 4.22 in section 4.6. However, thorough investigation on the influence of grain boundary orientation on IGC mechanism has been beyond the scope of this work. The exact explanation for the inconsistency between obtained results with literature remains therefore ambiguous.

### 5.3.5 Open circuit potential of edge and surface

OCP measurements were briefly carried out separately on the edge and the surface to detect any differences in OCP. Measurements were done on the 0.30 wt% , 0.00 wt% Zn and 0.31 wt% Cu, 0.60 wt% Zn alloys in the T5 condition. The results showed that a deviation of 1.5-3 mV was found between the edge and surface on both alloys. Whether this difference in corrosion potential is considerable enough to initiate a galvanic corrosion-like mechanism remains unclear. A dissimilarity in a few mV has been stated to have an effect for microgalvanic systems as grain boundaries (K. Nisancioglu, FICAL Technical meeting, 27.05.2016), although limited literature exists to verify this. A slight difference in OCP between the edge and surface was nonetheless observed on both alloys. The OCP curves for the surface on the two alloys are plotted in Figure 5.11, and shows the influence 0.60 wt% has on the OCP. Adding Zn to a 0.31 wt% Cu alloy directs the potential towards more negative values, which is to be expected. Zinc has a lower potential than Al in acidic environment.

However, assessing corrosion behaviour of alloys based solely OCP on measurements is not sufficient. OCP does not provide information on corrosion rate. Potentiodynamic polarisation in combination with OCP measurements would have contributed to a better understanding of the interaction between the fibrous edges and the recrystallised surface. In addition, the test set-up that was used may have not been ideal. The two curves recorded for the 0.31 wt% Cu, 0.60 wt% Zn alloy seemed to interact during the measurements, indicating that possibly a small current was induced. The measurements should probably have been carried out in separate vessels even though the alloy content was identical. Since the OCP difference is so minor, the slightest interactions are very visible. Furthermore, the other OCP parallel in Appendix E does not display the exact same

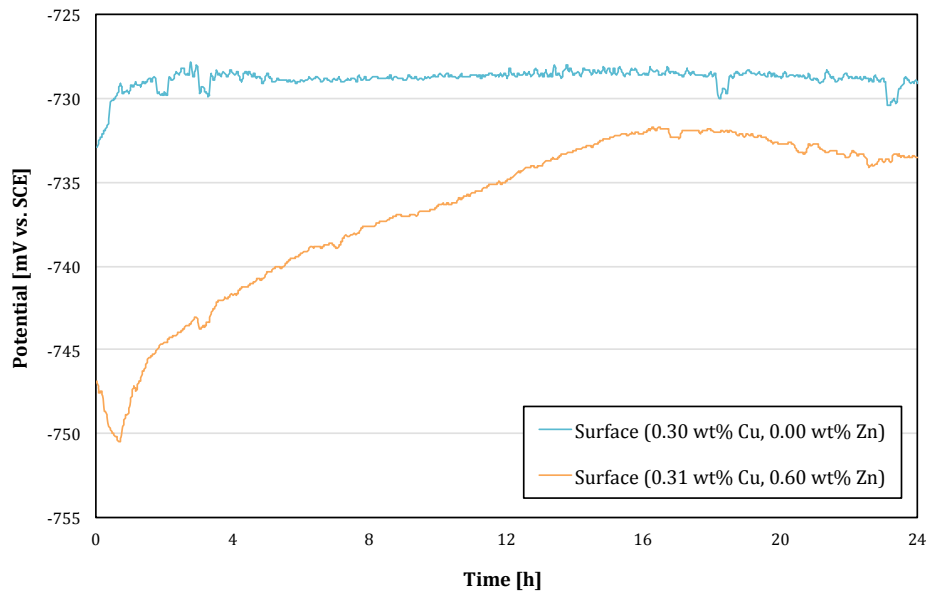


**Figure 5.11:** 24 h OCP measurement comparing the effect of 0.60 wt% Zn in a 6082 alloy containing 0.3 wt% Cu.

behaviour as the presented results, especially not the measurements done on the 0.30 wt% Cu, 0.00 wt% Zn alloy. The OCP measured according to this method appear to be highly responsive to any deviation in test preparation due to the scattering results. The test specimen might for instance be sensitive to the alkaline etch performed prior to testing. Any variance in the duration of the smut and desmutting process could be of importance.

### 5.3.6 Practical significance

This thesis has attempted to approach possible challenges related to IGC testing systematically when testing according to BS-ISO 11846. In terms of practical significance, these results may be relevant to how corrosion testing should be carried out. The industry and researchers rely heavily on the accuracy of these standards, as they provide a system for assessing corrosion susceptibility in engineering materials. Consequently, the recurring observation from this work may have a significant impact on how IGC susceptibility is interpreted, as they strongly indicate that sensitivity to IGC can be concealed for particular microstructures. In this instance, certain susceptible profiles with a fibrous grain structure, which had severely corroded edges, showed no sign of IGC. This may, in worst case, lead to improper interpretation of the results, where susceptible materials are not identified and is rather assessed as resistant. Another challenge is complications related to comparing results among researchers, as the microstructure of the tested alloys are not always identified in studies. The BS-ISO 11846 does not provide any specifications on microstructure,



although it states that corrosion close to edges should not be examined during metallographic examination. Nevertheless, the standard does not account for that corrosion of the exposed fibrous microstructure might impede IGC initiation on the surface to be examined. A rather bold suggestion derived from the obtained results is that the standard should perhaps be revised and include microstructural effects, and how they may influence the degree of IGC on susceptible materials.

This could be achieved by requiring edges to be covered, although the method utilised here with beeswax is not necessarily an optimal solution. The removal of beeswax is challenging and make weight loss measurements inaccurate as residual beeswax is often present. Furthermore, as the beeswax is heated, investigation on whether this might affect precipitation and thus the corrosion behaviour may be advised.

## 5.4 Further work

Potenitodynamic polarisation should be carried out to investigate the corrosion rates on the recrystallised surface and fibrous edge, respectively. This can contribute to clarify if the edge microstructure on the T5 profiles are more rapidly corroded relative to the recrystallised surface. In addition, measuring the corrosion rate can reveal if the small deviation in OCP between the edge and surface is considerable enough to initiate galvanic corrosion-like mechanisms, where the fibrous edges act as a sacrificial anode.

Additional OCP measurements of the edge and surface specimens should be obtained, and the measurements should be conducted in separate vessels even though the alloy composition is identical. This is to avoid any risk of interaction between the two samples in the same electrolyte.

A more thorough study on the main cause for severe corrosion on the fibrous texture could be of interest. Investigation on whether high grain boundary density or the grain boundary angles has the largest influence on corrosion behaviour could be done by in-depth TEM studies of the grain boundary microstructure dependent on grain boundary angle, and EBSD characterisation on grain orientation in the different textures. These techniques could contribute to elucidate the mechanism behind the observed corrosion of the fibrous texture.

Further investigation on whether Zn can decrease the IGC susceptibility in AlMgSi(Cu) alloys is not highly recommended from a commercial perspective, as these alloys have been proven to display poor IGC resistance in the peak aged condition compared to Zn free alloys. The alloys are unsuitable for structural applications in maritime environment due to the high IGC susceptibility. Focus should be directed towards optimising thermomechanical treatment of the existing alloys to achieve the most favourable combination of mechanical properties and IGC resistance, or to find other alloying additions that can counteract the IGC susceptibility induced by Cu. A suggestion is

the addition of lithium. Lithium is more anodic than aluminium and has a lower solubility in the Al matrix than Zn. The alloying element might therefore segregate to the grain boundaries more readily than what was observed for Zn. Furthermore, Li is a light element and is known to reduce the structural mass when alloyed in Al, as in Al-Li alloys. Perhaps the formation of a Li rich film at the grain boundary can reduce the cathodic nature caused by Cu, and concurrently reduce the electrochemical potential difference between the boundary and PFZ, correspondingly to what is observed when Mg is alloyed in excess.



## Chapter 6

# Conclusion

The objective of this study was to contribute to a better understanding on how edge microstructure affects results on IGC susceptibility when copper containing AA6082 alloys modified with Zn are tested according to BS-ISO 11846. Furthermore, whether the addition of Zn could reduce the IGC susceptibility in these alloys was also investigated. Specific parameters related to the IGC test execution was varied and several test parallels were conducted to examine how edge microstructure affected the IGC results. The IGC testing was performed on extruded profiles of four different alloy compositions with varying Cu and Zn content in the T5 and T6 temper.

Results strongly indicated that edge microstructure had a significant effect on the IGC behaviour at the recrystallised surface. Corrosion susceptible T5 profiles which possessed a fibrous microstructure experienced severe corrosion on the edges, initiated at the cut surface perpendicular to the extrusion direction. The edge corrosion was mainly confined to the fibrous texture, whereas the surface experienced far less corrosion. This was fairly evident for the 0.30 wt% Cu, 0.00 wt% Zn and 0.31 wt% Cu, 0.21 wt% Zn alloys. Covering the fibrous edge of these alloys led to extensive IGC on the surface, suggesting that the fibrous edges acted as some form of sacrificial anode. The textured edges might be more preferable sites for corrosion initiation due to the high grain boundary density exposed at the cut surface. A slight deviation in OCP was observed for respectively the edge and surface of T5 tempered profiles with a fibrous edge. This sacrificial-like effect was not observed on the T6 profiles that had a fully recrystallised microstructure. The severely corroded fibrous edges seemed to conceal IGC susceptibility on the recrystallised surface of the specimen, indicating that the BS-ISO 11846 standard is insufficient in accounting for edge effects during testing.

Furthermore, the addition of Zn above 0.21 wt% had a detrimental effect on IGC resistance and the susceptibility was increased when 0.60 wt% Zn was added. STEM imaging and EDS analysis of the 0.31 wt% Cu, 0.60 wt% Zn alloy in the T5 temper revealed that the frequently reported Cu film was present at the grain boundaries, in addition to the existence of a PFZ mainly depleted of Mg and Si. Zn however remained primarily in solid solution with the Al matrix, as no evident segregation was observed. Further activation of the PFZ was therefore believed to occur. In combination with the Cu rich film at the grain boundary, this may be a possible explanation for the observed increase in IGC when Zn is added to AlMgSi(Cu) alloys.



# Bibliography

- [1] B. Thundal. *Aluminium*. Almqvist & Wiksell Förlag, Kristianstad, 1991.
- [2] F.M. Mazzolani. New Challenges for Aluminium Structures : An Introduction Structural Applications of Aluminium in Civil Engineering Fields of Application. *Structural Engineering International*, (4):1–4, 2006.
- [3] J. Hirsch. Aluminium in Innovative Light-Weight Car Design. *Materials Transactions*, 52(5):818–824, 2011.
- [4] D. Carle and G. Blount. The suitability of aluminium as an alternative material for car bodies. *Materials & Design*, 20:267–272, 1999.
- [5] W.S. Miller, L. Zhuang, J. Bottema, A.J. Wittebrood, P. De Smet, A. Haszler, and A. Vieregge. Recent development in aluminium alloys for the automotive industry. *Materials Science and Engineering: A*, 280(1):37–49, 2000.
- [6] G.B. Burger, A.K. Gupta, P.W. Jeffrey, and D.J. Lloyd. Microstructural control of aluminum sheet used in automotive applications. *Materials Characterization*, 35(1):23–39, 1995.
- [7] H. Helms and U. Lambrecht. Energy Savings by lightweighting (Final report). Technical Report January, IFEU - Institute for Energy and Environmental Research, 2004.
- [8] European Aluminium Association. Stiffness Relevance and Strength Relevance in Crash of Car Body Components. Technical Report May, European Aluminium Association, 2010.
- [9] G. Svenningsen, J.E. Lein, A. Bjørgum, J.H. Nordlien, Y. Yu, and K. Nisancioglu. Effect of low copper content and heat treatment on intergranular corrosion of model AlMgSi alloys. *Corrosion Science*, 48(1):226–242, 2006.
- [10] G. Svenningsen, M.H. Larsen, J.C. Walmsley, J.H. Nordlien, and K. Nisancioglu. Effect of artificial aging on intergranular corrosion of extruded AlMgSi alloy with small Cu content. *Corrosion Science*, 48(6):1528–1543, 2006.
- [11] M.H. Larsen, J.C. Walmsley, O. Lunder, and K. Nisancioglu. Effect of Excess Silicon and Small Copper Content on Intergranular Corrosion of 6000-Series Aluminum Alloys. *Journal of The Electrochemical Society*, 157(2):C61, 2010.

- 
- [12] K. Shimizu and K. Nisancioglu. High Resolution SEM Investigation of Intercrystalline Corrosion on 6000-Series Aluminum Alloy with Low Copper Content. *ECS Electrochemistry Letters*, 3(9):C29–C31, 2014.
- [13] J. Holmestad, M. Ervik, C.D. Marioara, and J.C. Walmsley. Investigation of Grain Boundaries in an Al-Mg-Si-Cu Alloy. *Materials Science Forum*, 794-796:951–956, 2014.
- [14] P.V.T. Lam. *Corrosion of 6082 alloys in maritime environment*. Project thesis, Norwegian University of Science and Technology, 2015.
- [15] M. Stoknes, T. Furu, and O. Lunder. *Effect of Copper and Zinc on Corrosion Behaviour and Mechanical Properties in 6082-Alloys*. Master thesis, Norwegian University of Science and Technology, 2015.
- [16] F. King. *Aluminium and its alloys*. John Wiley & Sons Ltd., West Sussex, 1987.
- [17] J.R. Davis, editor. *ASM Specialty Handbook. Aluminium and Aluminium Alloys*. ASM International, 1993.
- [18] I.J. Polmear. *Light Alloys: From Traditional Alloys to Nanocrystals*. Butterworth-Heinemann, 4th edition, 2005.
- [19] A. Almar-Næss. *Metalliske materialer*. Tapir Forlag, Trondheim, 3rd edition, 1967.
- [20] J.K. Solberg. *Teknologiske metaller og legeringer (kompendium)*. Institutt for Materialteknologi, NTNU, Trondheim, 2014.
- [21] J.G. Kaufman. *Introduction to Aluminium Alloys and Tempers*. ASM International, 2000.
- [22] G. Kaufman. Corrosion of Aluminum and Aluminum Alloys. In *ASM Handbook. Corrosion: Materials*, volume 13B, pages 95–121. 2005.
- [23] J.E. Hatch, editor. *Aluminium Properties and Physical Metallurgy*. Number May. ASM International, 1984.
- [24] A. Wimmer, J. Lee, and P. Schumacher. Phase Selection in 6082 Al-Mg-Si Alloys. *BHM Berg- und Hüttenmännische Monatshefte*, 157(8-9):301–305, 2012.
- [25] M. Bauser, G. Sauer, and K. Siegert. *Extrusion*. ASM International, 2nd edition, may 2006.
- [26] O. Reiso. Extrusion of AlMgSi alloys. *Materials Forum*, 28:32–46, 2004.
- [27] T. Pettersen and T. Furu. Extrusions from Heat Treatable Alloys. EN AW-6032, EN AW-6082 and EN AW-7108 - Processing, Microstructure, Simulation and Property Control. In Jürgen Hirsch, editor, *Virtual Fabrication of Aluminium Products. Microstructural Modeling in Industrial Aluminium Fabrication Processes*, chapter 7, pages 65–81. Wiley-VCH, Weinheim, 2006.

- 
- [28] P.K. Saha. *Aluminium Extrusion Technology*. ASM International, Materials Park, 2000.
- [29] T. Sheppard. *Extrusion of Aluminium Alloys*. Springer Science & Business Media, 2013.
- [30] S. Zajac, B. Hutchinson, A. Johansson, and L.-O. Gullman. Microstructure control and extrudability of Al-Mg-Si. *Materials Science and Technology*, 10(4), 1994.
- [31] W.D. Callister and D.G. Rethwisch. *Materials Science and Engineering*. John Wiley & Sons Ltd., 8th edition, 2011.
- [32] K.O. Pedersen, O.-G. Lademo, T. Berstad, T. Furu, and O.S. Hopperstad. Influence of texture and grain structure on strain localisation and formability for AlMgSi alloys. *Journal of Materials Processing Technology*, 200(1-3):77–93, 2008.
- [33] A. Lyons. *Materials for Architects and Builders*. Routledge, London, 5th edition, 2014.
- [34] M. Tercelj, M. Fazarine, G. Kugler, and I. Perus. Increasing mechanical properties of AA6082 by optimizing chemical compositions and processing during extrusion. In C.E. Suarez, editor, *Light Metals 2012*, pages 397–402. John Wiley & Sons Ltd., 2012.
- [35] J. Asensio-Lozano, B. Suárez-Peña, and G. Vander Voort. Effect of Processing Steps on the Mechanical Properties and Surface Appearance of 6063 Aluminium Extruded Products. *Materials*, 7(6):4224–4242, 2014.
- [36] J. Zhang, Z. Fan, Y.Q. Wang, and B.L. Zhou. Equilibrium pseudobinary Al-Mg<sub>2</sub>Si phase diagram. *Materials Science and Technology*, 17(May):494–496, 2001.
- [37] M.H. Jacobs. Phase diagrams, 1999.
- [38] M. Fujda, M. Matvija, and P. Zubko. Comparison of the Natural Ageing Behaviour of EN AW 6082 and Lead Free EN AW 6023 Aluminium Alloys. *Key Engineering Materials*, 586(9):125–128, 2014.
- [39] C.D. Marioara, S.J. Andersen, T.N. Stene, H. Hasting, J. Walmsley, A.T.J. Van Helvoort, and R. Holmestad. The effect of Cu on precipitation in Al-Mg-Si alloys. *Philosophical Magazine*, 87(23):3385–3413, 2007.
- [40] R. Holmestad, R. Bjørge, F.J.H. Ehlers, M. Torsæter, C.D. Marioara, and S.J. Andersen. Characterization and structure of precipitates in 6xxx Aluminium Alloys. *Journal of Physics: Conference Series*, 371:12082, 2012.
- [41] D.J. Chakrabarti and D.E. Laughlin. Phase relations and precipitation in Al-Mg-Si alloys with Cu additions. *Progress in Materials Science*, 49(3-4):389–410, 2004.

- [42] G.A. Edwards, K. Stiller, G.L. Dunlop, and M.J. Couper. The precipitation sequence in Al-Mg-Si alloys. *Acta Materialia*, 46(11):3893–3904, 1998.
- [43] Y. Ohmori, L.C. Doan, and K. Nakai. Ageing Processes in Al-Mg-Si Alloys during Continuous Heating. *Materials Transactions*, 43(2):246–255, 2002.
- [44] S.P. Ringer and K. Hono. Microstructural evolution and age hardening in aluminium alloys: atom probe field-ion microscopy and transmission electron microscopy studies. *Materials Characterization*, 44(1-2):101–131, 2000.
- [45] C.D. Marioara, S.J. Andersen, J. Røyset, O. Reiso, S. Gulbrandsen-Dahl, T.E. Nicolaisen, I.E. Opheim, J.F. Helgaker, and R. Holmestad. Improving thermal stability in Cu-containing Al-Mg-Si alloys by precipitate optimization. *Metallurgical and Materials Transactions A: Physical Metallurgy and Materials Science*, 45(7):2938–2949, 2014.
- [46] T. Saito, S. Wenner, E. Osmundsen, C.D. Marioara, S.J. Andersen, J. Røyset, W. Lefebvre, and R. Holmestad. The effect of Zn on precipitation in Al-Mg-Si alloys. *Philosophical Magazine*, 94(21):2410–2425, 2014.
- [47] C.D. Marioara, S.J. Andersen, H.W. Zandbergen, and R. Holmestad. The influence of alloy composition on precipitates of the Al-Mg-Si system. *Metallurgical and Materials Transactions A: Physical Metallurgy and Materials Science*, 36(13):691–702, 2005.
- [48] S.K. Kairiy, P.A. Rometsch, K. Diao, J.F. Nie, C.H.J. Davies, and N. Birbilis. Exploring the electrochemistry of 6xxx series aluminium alloys as a function of Si to Mg ratio, Cu content, ageing conditions and microstructure. *Electrochimica Acta*, 190:92–103, 2016.
- [49] W.F. Gale and T.C. Totemeier. Heat treatment. In *Smithells Metals Reference Book*, chapter 29. Butterworth-Heinemann, 8th edition, 2003.
- [50] G. Marshall, P. Evans, R. Ricks, J. Hirsch, and A. Green. Strengthening Processes (aluMATTER).
- [51] R.R. Ambriz and D. Jaramillo. Mechanical Behavior of Precipitation Hardened Aluminum Alloys Welds. *Light Metal Alloys Applications*, (Figure 1):35–59, 2014.
- [52] W. Soboyejo. *Mechanical Properties of Engineered Materials*. Marcel Dekker, Inc., New York, 2003.
- [53] C. Vargel, M. Jacques, and M.P. Schmidt. *Corrosion of Aluminium*. Elsevier, 2004.
- [54] K. Nisancioglu. Corrosion and protection of aluminum alloys in seawater. In D Féron, editor, *Corrosion Behaviour and Protection of Copper and Aluminium Alloys in Seawater (EFC 50)*, chapter 9, pages 145–155. Woodhead Publishing Limited, 2007.

- [55] G. Svenningsen, M.H. Larsen, J.H. Nordlien, and K. Nisancioglu. Effect of high temperature heat treatment on intergranular corrosion of AlMgSi(Cu) model alloy. *Corrosion Science*, 48(1):258–272, 2006.
- [56] K. Nisancioglu. Corrosion of Aluminium and Aluminium Alloys. In *Corrosion and corrosion protection (compendium)*, chapter 25, pages 1–17. Institutt for Teknisk Elektrokjemi, NTH, Trondheim, 2013.
- [57] P.E.J. Flewitt and R.K. Wild. *Grain Boundaries - Their Microstructure and Chemistry*. John Wiley & Sons Ltd., Chichester, 2001.
- [58] G. Svenningsen. *Intergranular Corrosion of AA6000-Series Aluminium Alloys*. Doctoral thesis, Norwegian University of Science and Technology, 2005.
- [59] M.H. Larsen, J. Mårdalen, A.J. Davenport, F. Eckermann, F. De Carlo, and K. Nisancioglu. In Situ X-ray Microtomography Study of Intergranular Corrosion in a 6000-series Aluminium Alloys. *ECS Meeting Abstract*, 212:6000, 2007.
- [60] P.A. Schweitzer. *Fundamentals of Metallic Corrosion: Atmospheric and Media Corrosion of Metals*. CRC Press Taylor & Francis Group, 2nd edition, 2007.
- [61] T. Minoda and H. Yoshida. Effect of grain boundary characteristics on intergranular corrosion resistance of 6061 aluminum alloy extrusion. *Metallurgical and Materials Transactions A*, 33(9):2891–2898, 2002.
- [62] T. Minoda and H. Yoshida. The Effect of Microstructure on Intergranular Corrosion Resistance of 6061 Alloy Extrusion. *Materials Science Forum*, 331-337:1689–1694, 2000.
- [63] G. Svenningsen, M.H. Larsen, J.H. Nordlien, and K. Nisancioglu. Effect of thermomechanical history on intergranular corrosion of extruded AlMgSi(Cu) model alloy. *Corrosion Science*, 48(12):3969–3987, 2006.
- [64] W.J. Liang, P.A. Rometsch, L.F. Cao, and N. Birbilis. General aspects related to the corrosion of 6xxx series aluminium alloys: Exploring the influence of Mg/Si ratio and Cu. *Corrosion Science*, 76:119–128, nov 2013.
- [65] K. Yamaguchi and K. Tohma. Effect of Zn addition on intergranular corrosion resistance of Al-Mg-Si-Cu alloys. In T. Sato, S. Kumai, T. Kobayashi, and Y. Murakami, editors, *Proceedings of the 6th International Conference on Aluminium Alloys, ICCAA-6*, pages 1657–1662, Toyohashi, Japan, 1998. The Japan Institute of Light Metals.
- [66] J. Holmestad, R.H. Mathiesen, R. Holmestad, and J.C. Walmsley. TEM studies of the effect of different Mg/Si-ratios on intergranular corrosion of Al-Mg-Si-Cu alloys. Technical report, Norwegian University of Science and Technology, 2015.

- 
- [67] M.H. Larsen, J.C. Walmsley, O. Lunder, R.H. Mathiesen, and K. Nisancioglu. Intergranular Corrosion of Copper-Containing AA6xxx AlMgSi Aluminum Alloys. *Journal of The Electrochemical Society*, 155(11):C550, 2008.
- [68] S.K. Kairy, T. Alam, P.A. Rometsch, C.H.J. Davies, R. Banerjee, and N. Birbilis. Understanding the Origins of Intergranular Corrosion in Copper-Containing Al-Mg-Si Alloys. *Metallurgical and Materials Transactions A*, 47(3):985–989, 2016.
- [69] F. Eckermann, T. Suter, P.J. Uggowitzer, A. Afseth, and P. Schmutz. The influence of MgSi particle reactivity and dissolution processes on corrosion in Al-Mg-Si alloys. *Electrochimica Acta*, 54(2):844–855, 2008.
- [70] M.H. Larsen and K. Nisancioglu. RELEVANCE OF COPPER AND SILICON IN INTERCRYSTALLINE CORROSION OF AA6000-SERIES ALUMINIUM ALLOYS. pages 2–6.
- [71] V.G. Davydov, V.S. Siniavski, L.B. Ber, K.H. Rendigs, G. Tempus, V.D. Valkov, V.D. Kalinin, Ye.V. Titkova, O.G. Ukolova, Ye.A. Lukina, Ye.I. Shvechikov, and Ye.Ya. Kaputkin. Influence of SSTT, Ageing Regime and Stretching on IGC, Complex of Properties and Precipitation Behavior of 6013 Alloy. *Materials Science Forum*, 331-337:1315–1320, 2000.
- [72] F. Eckermann, T. Suter, P.J. Uggowitzer, A. Afseth, A.J. Davenport, B.J. Connolly, M.H. Larsen, F. De Carlo, and P. Schmutz. In situ monitoring of corrosion processes within the bulk of AlMgSi alloys using X-ray microtomography. *Corrosion Science*, 50(12):3455–3466, 2008.
- [73] T.D. Burleigh. Corrosion of Aluminium and Its Alloys. In G.E. Totten and D.S. MacKenzie, editors, *Handbook of Aluminium: Volume 2: Alloy Production and Materials Manufacturing*, chapter 11. CRC Press Taylor & Francis Group, 2003.
- [74] P. McIntyre and A.D. Mercer. Corrosion Testing and Determination of Corrosion Rates. In L.L. Shreir, editor, *Corrosion Volume 2: Corrosion Control*. Butterworth-Heinemann, 3rd edition, 1994.
- [75] P.R. Roberge. *Handbook of Corrosion Engineering*. McGraw-Hill Education, 2nd edition, 2012.
- [76] J.R. Kissell, S.G. Pantelakis, and G.N. Haidemenopoulos. Aluminium and Aluminium Alloys. In J.K. Wessel, editor, *Handbook of Advanced Materials: Enabling New Designs*, chapter 9, pages 321–463. Wiley-Interscience, 2004.
- [77] ASTM. G110-92: Standard Practice for Evaluating Intergranular Corrosion Resistance of Heat Treatable Aluminum Alloys by Immersion in Sodium Chloride + Hydrogen Peroxide Solution, 2009.
- [78] British Standards Institution. ISO 11846:1995. Corrosion of metals and alloys - Determination of resistance to intergranular corrosion of solution heat-treatable aluminium alloys, 1995.



- 
- [79] Ø. Bauger and T. Furu. Results from Field Testing of Aluminium Extrusions on a Truck for Six Years . Comparisons with Accelerated Corrosion Testing. 2010.
- [80] K. Nisancioglu. Uniform corrosion kinetics. In *Corrosion and corrosion protection (compendium)*, chapter 4, pages 1–15. Institutt for Teknisk Elektrokjemi, NTH, 2013.
- [81] D. Landolt. *Corrosion and Surface Chemistry of Metals*. EPFL Press, Lausanne, Switzerland, 2007.
- [82] M. J. Pryor and D. J. Astley. Guides to Good Practice in Corrosion Control: Bimetallic Corrosion. Technical report, National Physical Laboratory, 2013.



## Appendix A

# Depth of recrystallised layer

The recrystallised layer depth of all T5 samples were measured in LM. The measurements from each profile is presented in Table A.1, and the average recrystallised layer depth values presented in Table 4.1 were calculated from these. A total of ten measurements were taken on arbitrary locations on each specimen.

**Table A.1:** Measurements of the recrystallised surface layer for T5 profiles.

| Profile   | Measurements [ $\mu\text{m}$ ] |     |     |     |     |     |     |     |     |     | Avg. depth [ $\mu\text{m}$ ] |
|-----------|--------------------------------|-----|-----|-----|-----|-----|-----|-----|-----|-----|------------------------------|
| <b>1a</b> | 498                            | 477 | 461 | 448 | 469 | 469 | 415 | 465 | 461 | 494 | 465                          |
| <b>4a</b> | 495                            | 478 | 490 | 433 | 462 | 453 | 458 | 429 | 540 | 420 | 466                          |
| <b>4b</b> | 375                            | 375 | 449 | 441 | 503 | 486 | 425 | 462 | 486 | 408 | 441                          |
| <b>4c</b> | 499                            | 474 | 466 | 453 | 511 | 466 | 519 | 499 | 594 | 437 | 492                          |



## Appendix B

# Vickers hardness measurements

The measured Vickers hardness values for the T5 tempered profiles are listed in Table B.1, while the values for the T6 profiles are in Table B.2. Six indents were made on each sample, and the average HV values used in Figure 4.3 were calculated from these measurements. Standard deviation values were calculated from equation B.1, where  $s$  is the standard deviation,  $N$  is sample set size,  $x_i$  is one value in the set and  $\bar{x}$  is the average of the set of values.

$$s = \sqrt{\frac{1}{N-1} \sum_{i=1}^N (x_i - \bar{x})^2} \quad (\text{B.1})$$

**Table B.1:** Vickers hardness measurements for profiles in the T5 temper.

| Profile   | Measurements [HV1] |       |       |       |       |       |       |       |       |       | Avg. [HV1] | $s$  |
|-----------|--------------------|-------|-------|-------|-------|-------|-------|-------|-------|-------|------------|------|
| <b>1a</b> | 114.9              | 117.5 | 110.0 | 110.2 | 107.1 | 113.0 | 112.2 | 112.0 | 108.4 | 104.4 | 111.0      | 3.82 |
| <b>4a</b> | 122.0              | 125.1 | 125.7 | 121.9 | 128.0 | 126.0 | 123.2 | 124.1 | 129.0 | 121.8 | 124.7      | 2.55 |
| <b>4b</b> | 125.4              | 120.1 | 120.5 | 123.8 | 125.5 | 122.4 | 127.3 | 127.5 | 119.3 | 125.5 | 123.7      | 3.00 |
| <b>4c</b> | 124.5              | 122.4 | 122.1 | 124.3 | 120.2 | 112.6 | 122.3 | 123.9 | 121.9 | 123.1 | 121.7      | 3.46 |

**Table B.2:** Vickers hardness measurements for profiles in the T6 temper.

| Profile   | Measurements [HV1] |       |       |       |       |       |       |       |       |       | Avg. [HV1] | $s$  |
|-----------|--------------------|-------|-------|-------|-------|-------|-------|-------|-------|-------|------------|------|
| <b>1a</b> | 125.6              | 127.7 | 114.4 | 126.7 | 124.4 | 118.0 | 124.6 | 125.0 | 118.0 | 128.1 | 123.1      | 4.93 |
| <b>4a</b> | 133.5              | 135.1 | 136.7 | 131.4 | 134.2 | 134.0 | 132.4 | 129.3 | 136.2 | 133.2 | 133.6      | 2.21 |
| <b>4b</b> | 134.3              | 130.8 | 129.2 | 130.4 | 134.7 | 140.8 | 132.3 | 140.2 | 138.2 | 142.6 | 135.4      | 4.80 |
| <b>4c</b> | 132.5              | 135.8 | 133.5 | 127.5 | 128.6 | 132.6 | 133.3 | 140.8 | 133.4 | 132.3 | 133.0      | 3.65 |

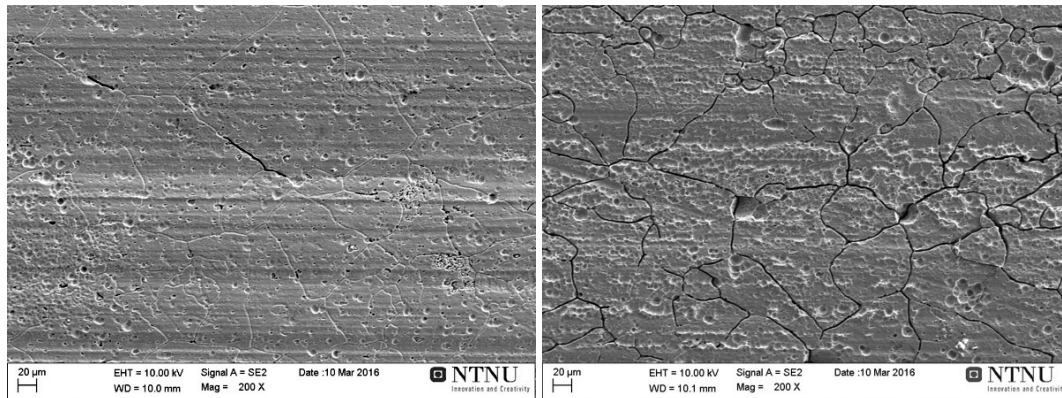


## Appendix C

# SEM imaging of surface corrosion damages

SEM images of corroded samples after IGC testing from various test parallels are presented in Figure C.1, C.2 and C.3.

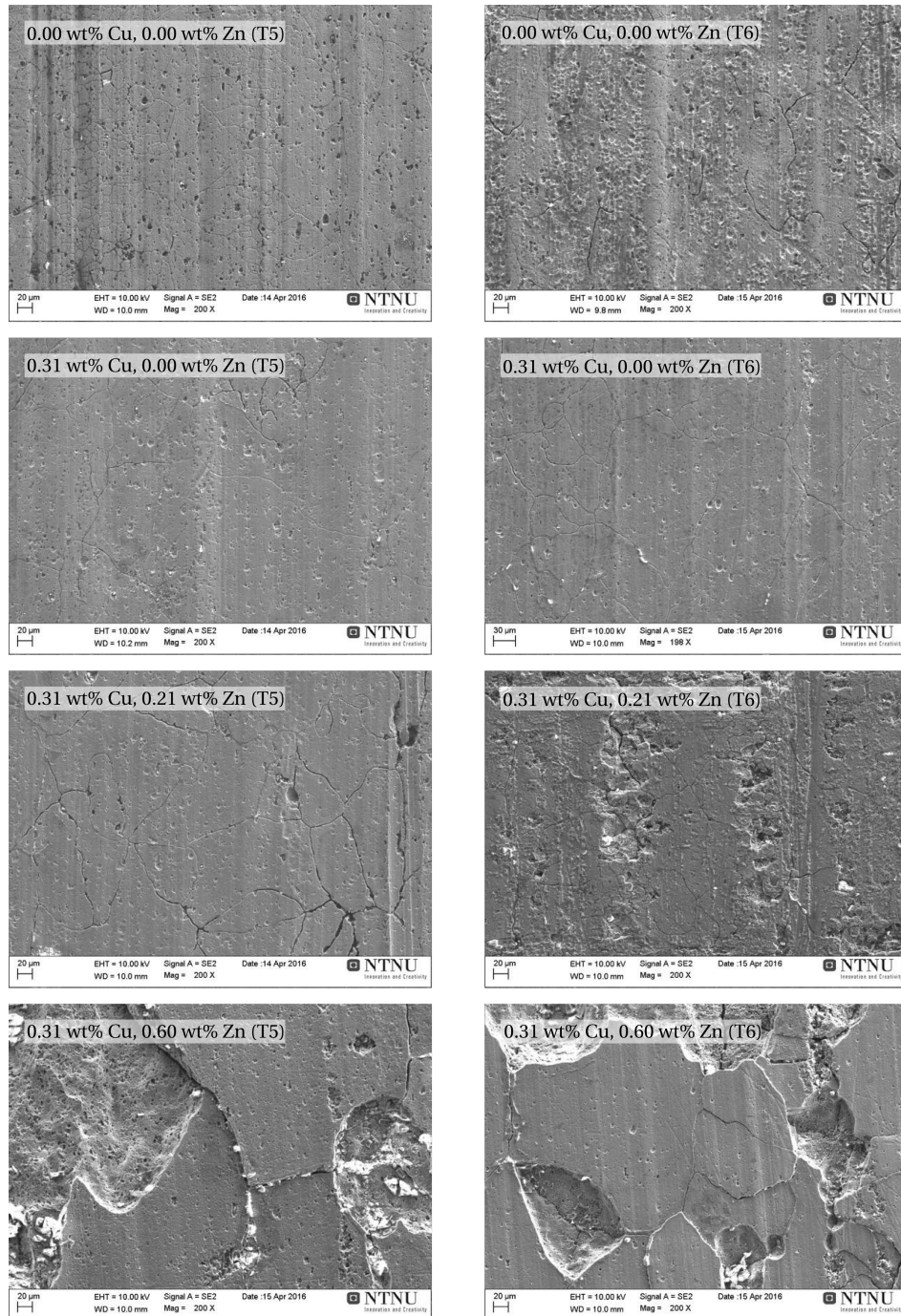
### Parallel 1: standard execution



**(a)** 0.00% Cu, 0.00% Zn (T5)

**(b)** 0.00% Cu, 0.00% Zn (T6)

**Figure C.1:** SEM images (200X) of surface after corrosion testing on selected specimens, and the difference in corrosion behaviour with ageing treatment. Alloy composition given in wt% .

**Parallel 2: edge covered specimens**

**Figure C.2:** SEM images (200X) of surface after corrosion testing on selected specimens, and the difference in corrosion behaviour with ageing treatment. Alloy composition given in wt% .



### Parallel 3: reduced edge/surface ratio

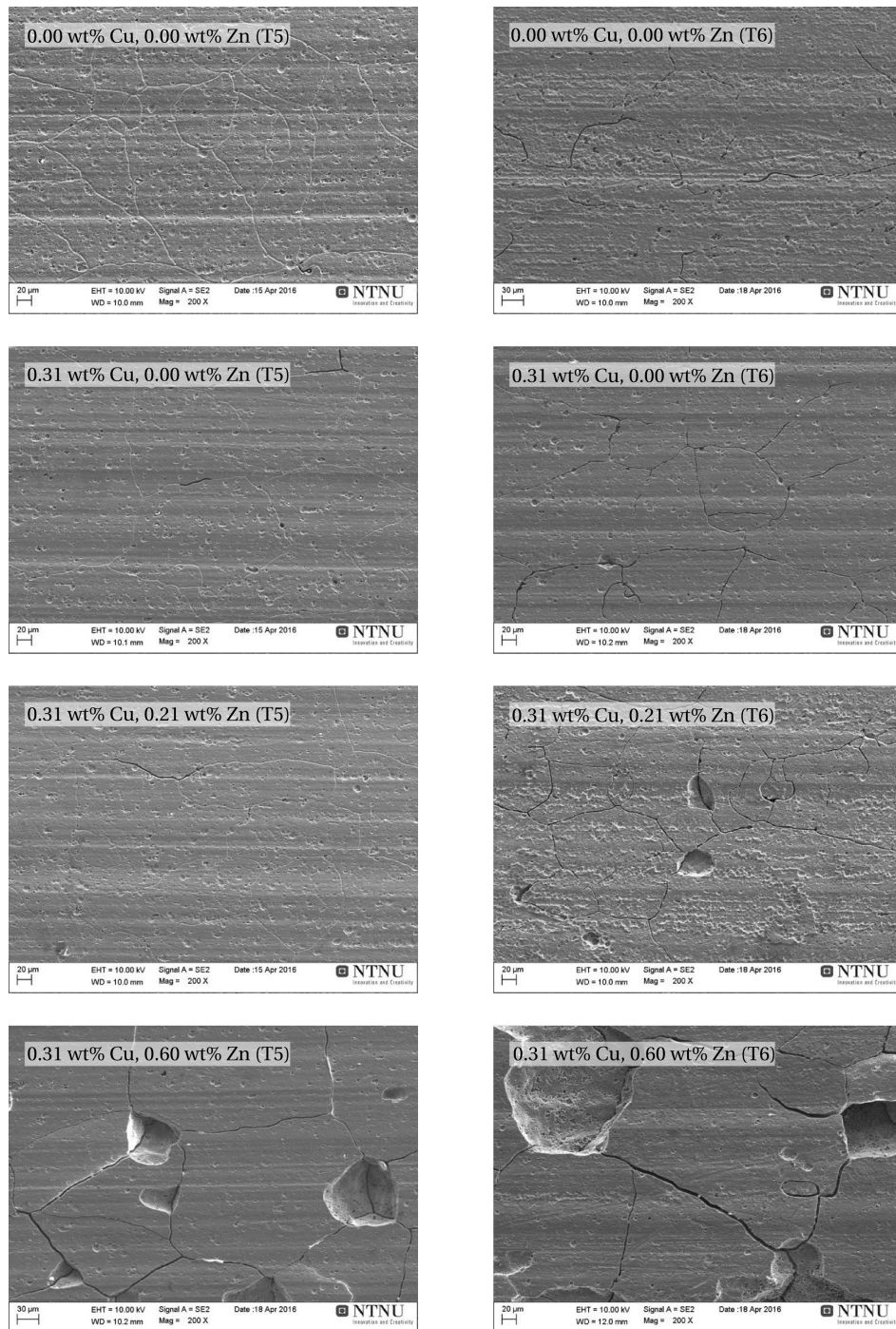


**Figure C.3:** SEM images (200X) of surface after corrosion testing on selected specimens, and the difference in corrosion behaviour with ageing treatment. Alloy composition given in wt% .



## Appendix D

# Diffraction patterns from grain boundaries

Diffraction patterns shown in Figure D.1 and D.2 are taken from the high and low angle grain boundary, respectively. The patterns were taken of the grains on each side of the boundary to roughly estimate whether the boundary was a high or low angle one during the TEM analysis presented in section 4.6. The patterns were not indexed. All images were acquired by John C. Walmsley from SINTEF Materials and Chemistry.

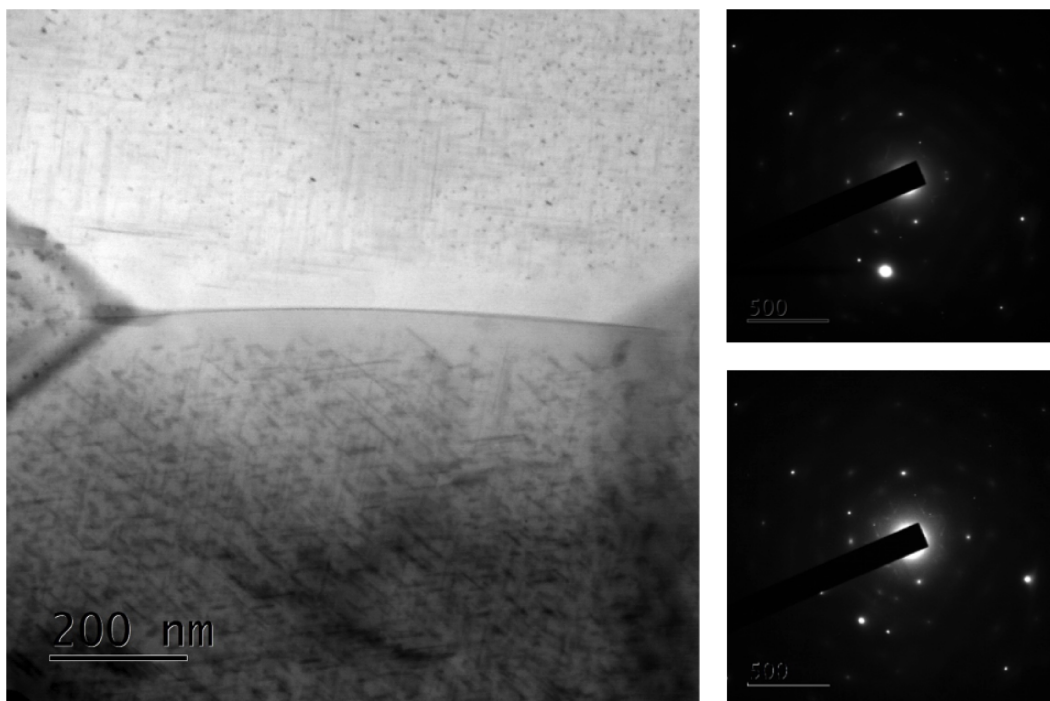


**Figure D.1:** Diffraction patterns from the grains on each side of the high angle boundary. Linear scale on the diffraction patterns is 500 nm.

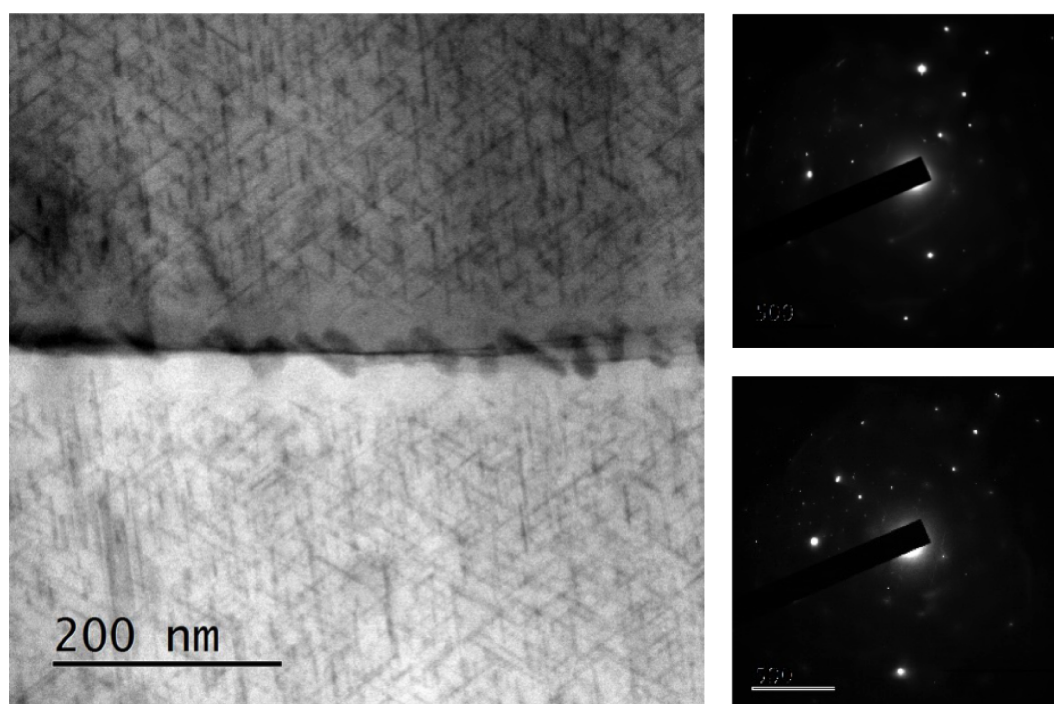


**Figure D.2:** Diffraction patterns from the grains on each side of the low angle boundary. Linear scale on the diffraction patterns is 500 nm.

## Appendix E

### OCP measurements

The other OCP measurement parallel conducted on the edge and surface of the T5 tempered profiles are found in Figure E.1 and E.2. OCP was measured for the 0.30 wt% Cu, 0.00 wt% Zn and 0.31 wt% , 0.60 wt% Zn alloys.

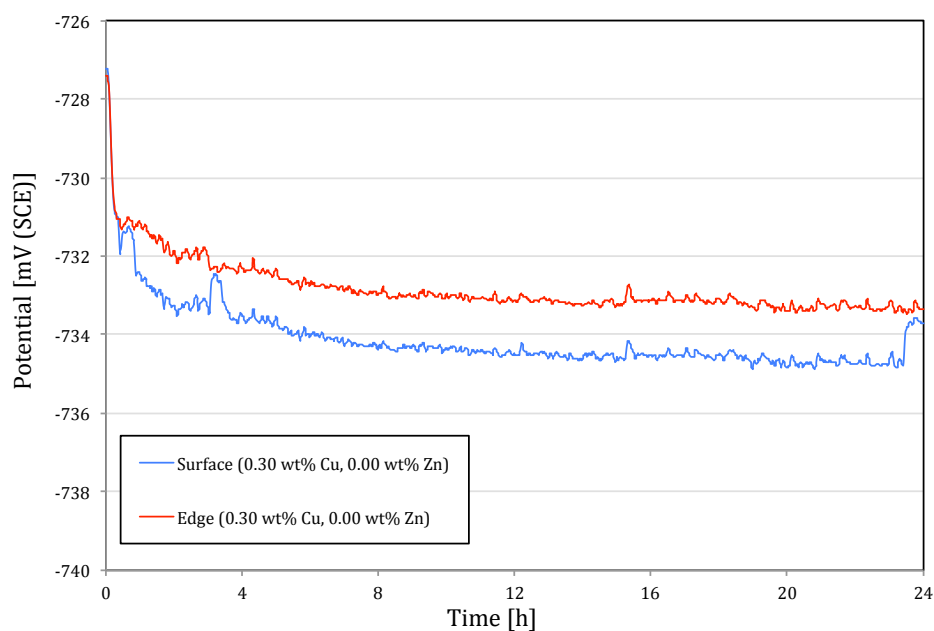


**Figure E.1:** 24 h OCP measurements of the edge and surface of a T5 tempered 0.30 wt% Cu, 0.00 wt% Zn alloy.

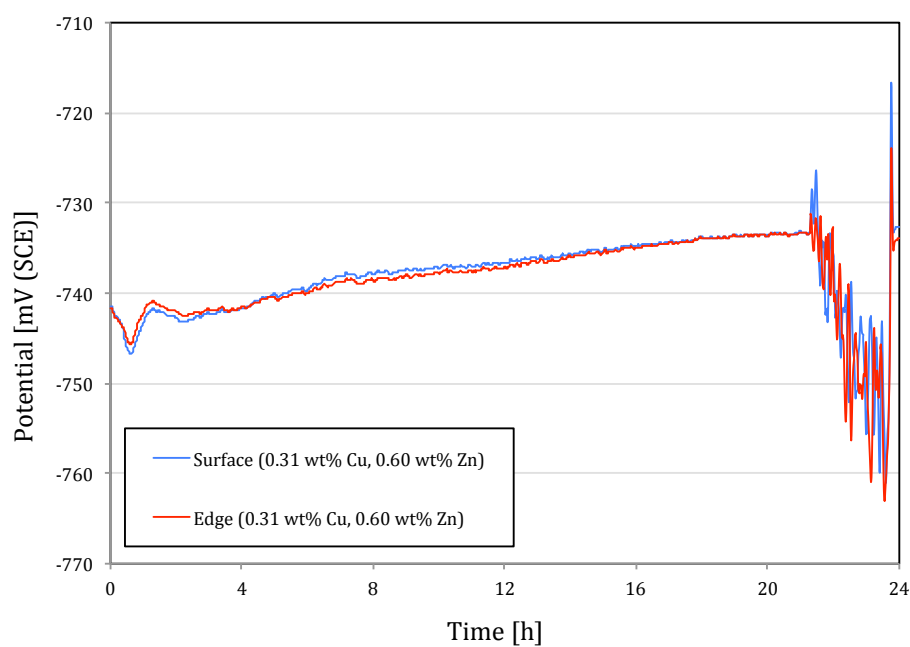


**Figure E.2:** 24 h OCP measurements of the edge and surface of a T5 tempered 0.31 wt% Cu, 0.60 wt% Zn alloy.